Multiplexed visible light communication systems using GaN-based sources

Shaun Viola

Submitted in fulfilment of the requirements for the
Degree of Doctor of Philosophy

School of Engineering
College of Science and Engineering
University of Glasgow

October 2018

Abstract

With the emergence of efficient semiconductor solid state lighting a new application space has emerged for communications, namely visible light communications (VLC). The high speed modulation capabilities of Gallium Nitride (GaN) based LEDs and laser diodes means these devices have the potential to supplement or replace existing radio wave standards such as Wifi, as well as creating new applications for optical communications such as underwater VLC. Given the ever increasing demand for information in modern society, it is desirable to continually increase the bandwidth capabilities of communication systems through both exploration of unused frequency spectrum, like the visible spectrum, and also the application of existing and developing multiplexing techniques.

This thesis will focus on the investigation of quadrature amplitude modulation (QAM) based orthogonal frequency division multiplexing (OFDM) as applied to GaN based sources in various VLC systems. In this thesis investigation of complex modulation formats and advanced multiplexing techniques applied to novel μ-LED devices has shown VLC system bandwidths of up to 655 MHz and data rates of up to 7.91 Gbit/s which, to the authors knowledge, is the highest data rate achieved using a single μ-LED pixel for data transmission.

The laser based VLC systems shown in this thesis have utilised both the simplest form of baseband modulation on off keying (OOK) as well as QAM based OFDM. These systems, at the time of publication, demonstrated the highest data rate achieved for each of these modulation types using commercially available devices.

In addition to multiplexing using orthogonal frequencies the implementation of spatial multiplexing has become an area of great interest for free-space optical (FSO) communication links, particularly for its use in last-mile links within larger optical networks. Light carrying orbital angular momentum (OAM) has emerged as a potential candidate that could be utilised for multiplexing independent channels. The feasability of OAM multiplexing underwater has been investigated through analysis of inter-channel crosstalk for a set of 11 OAM modes propagating through 3 m of slowly flowing water, similar to that found in Oceanic conditions. At publication this was the first investigation of its kind where crosstalk effects induced by flowing water were measured.

Publications

Articles

1. Shaun Viola, Mohamed Sufyan Islim, Scott Watson, Stefan Videv, Harald Haas, Anthony E Kelly. *15 Gb/s OFDM-based VLC using direct modulation of 450 GaN laser diode*. Proceedings of SPIE, vol. 10437, p. 104370E (2017).

2. Mohamed Sufyan Islim, Ricardo X Ferreira, Xiangyu He, Enyuan Xie, Stefan Videv, Shaun Viola, Scott Watson, Nikolaos Bamiedakis, Richard V Penty, Ian H White, Anthony E Kelly, Erdan Gu, Harald Haas, Martin D Dawson. *Towards 10 Gb/s orthogonal frequency division multiplexing-based visible light communication using a GaN violet micro-LED*. Photonics Research, vol 5, issue 2, p. A35-A43 (2017).

3. S Watson, S Viola, G Giuliano, SP Najda, P Perlin, T Suski, L Marona, M Leszczynski, P Wisniewski, R Czernecki, G Targowski, MA Watson, H White, D Rowe, L Laycock, AE Kelly. *High speed visible light communication using blue GaN laser diodes*. Proceedings of SPIE, vol. 9991, p. 99910A (2016).

4. Shaun Viola, Manousos Valyrakis, Antony E Kelly, Martin PJ Lavery. *Submersed free-space propagation of beams carrying orbital angular momentum*. Proceedings of SPIE, vol. 9991, p. 999103 (2016).

Conferences

1. Shaun Viola, Manousos Valyrakis, Anthony E Kelly, Martin PJ Lavery. *Study of orbital angular momentum mode crosstalk induced by propagation through water*. Lasers and Electro-Optics (CLEO), 2016 Conference on. p.1-2. Paper SW1F.3.

2. Giovanni Giuliano, Shaun Viola, Scott Watson, Leslie Laycock, Duncan Rowe, Anthony E Kelly. *Laser based underwater communication systems*. Transparent Optical Networks (ICTON), 2016 18th International Conference on. p. 1-4. Paper Tu.B2.3.

3. Scott Watson, Steffan Gwyn, Shaun Viola, Giovanni Giuliano, Opeoluwa Odedina, Thomas J. Slight, Szymon Stanczyk, Szymon Grzanka, Amit Yadav, Duncan Rowe, Leslie Laycock, Kevin E. Docherty, Edik Rafailov, Piotr Perlin, Steve Najda, Mike Leszczynski,

Mohamed Sufyan Islim, Stefan Videv, Haral Haas, Anthony E. Kelly. *InGaN/GaN Laser Diodes for Visible Light Communications and Beyond*. CLEO Pacific Rim 2018.

Contents

List of Figures

Acknowledgements

Firstly, I'd like thank my supervisor, Prof. Tony Kelly, for initially giving me the opportunity to do a PhD and for his continuous guidance and support throughout my time as a PhD student. Additionally, thanks to Scott Watson for his help and understanding. At different times during my PhD I worked collaboratively with other researchers and so would like to thank my co-authors from the works that have been published within this thesis. Finally, I'd like to thank my family and friends for their support throughout the last few years and the EPSRC for funding this research.

Declaration

This thesis consists of the author's original work, with exception of collaborative work which has been explicitly acknowledged. All of the experimental system design, implementation and results analysis in this thesis is the original work of the author.

Chapter 2 is the result of a collaboration between three research groups. The μ-LED devices were provided by the University of Strathclyde and the OFDM communications MATLAB code was provided by the University of Edinburgh. With the exception of the system optical source and OFDM communications MATLAB code, all other system design, experimental implementation and results analysis in chapter 2 were obtained by the author at the University of Glasgow. The QAM-OFDM modulation of the laser in chapter 3 was achieved using the MATLAB code provided by the University of Edinburgh. The DFB laser device used in chapter 4 was fabricated under the CoolBlue Innovate UK project.

This work has not been previously submitted for any other degree. The copyright of this thesis therefore belongs to the author and due acknowledgement must be made if any material from within is used.

Glasgow, Scotland, UK, 2018.

Abbreviations

AC - Alternating Current
AR - Anti-reflection
B - Boron
BER - Bit error rate
BERT - Bit error rate test
CMOS - Complementary metal-oxide semiconductor
DC - Direct current DFT - Discrete Fourier transform
DH - Double heterostructure
EQE - External quantum efficiency
DVI - Digital visual interface
FDM - Frequency division multiplexing
FEC - Forward error correction
FFT - Fast Fourier transform
FSO - Free space optical/optics
FMF - Few mode fibre
FP - Fabry Perot
GaAs - Gallium arsenic
GaAsP - Gallium arsenide phosphide
GaN - Gallium Nitride
HDMI - High-Definition Multimedia Interface
HG - Hermite Gaussian
HR - High-reflectance
ICI - Inter carrier interference
IFFT - Inverse fast Fourier transform
In - Indium
InGaN - Indium gallium nitride
IQE - Internal quantum efficiency
IR - Infrared
ISI - intersymbol interference
LAN - Local area network

LD - Laser diode
LED - Light emitting diode
LG - Laugerre Gaussian
LI - Light LVI - Luminescence-voltage-current
MDM - Mode division multiplexing
MIMO - Multiple input multiple output
MOCVD - Metal-organic chemical vapour deposition
MQW - Mulit quantum well
NRZ - Non-return to zero
OAM - Orbital angular momentum
OFDM - Orthogonal frequency division multiplexing
OOK - On off keying
P - Phosphorus
PIN - p type-intrinsic-n type
POF - Plastic optical fibre
PRBS - Pseudo-random bit sequence
QAM - Quadrature amplitude modulation
QPSK - Quadrature phase shift keying
RF - Radio frequency
RMS - Root mean square
SDM - Spatial division multiplexing
Si - Silicon
SiC - Silicon carbide
SNR - Signal to noise ratio
SRH - Shockley-Read Hall
UAV - Unmanned autonomous vehicles
VLC - Visible light communication
WDM - Wavelength division multiplexing
μ-LED - Micro pixellated light emitting diode

Chapter 1

Introduction

This thesis demonstrates the application of OFDM in visible light communication systems with both LEDs and lasers in free space. Furthermore, the effects from underwater turbulence on visible light OAM modes, which is an additional degree of multiplexing proposed for VLC, are demonstrated. The transmitter sources used in this thesis are LEDs and lasers, this chapter serves as a general introduction to these sources and their distinct characteristics. Additionally, the two multiplexing schemes employed in the experimental work detailed in this thesis, namely OFDM and OAM multiplexing, are described in this chapter. The chapter begins with a brief overview of the historical development of LEDs. The subsequent section then describes the structure and operation of LEDs. The two following sections introduce the laser diode covering historical development and operation in a similar manner to the introduction to LEDs. The final two sections will cover the historical development and theoretical basis for both OFDM and OAM.

1.1 The development of light-emitting diodes

The mechanism for photon emission in LEDs is distinct from that evident in incandescent light sources. Whilst incandescence relies on an increase in temperature within a material to emit light, typically > 750°C, LEDs experience electroluminescence through the recombination of electrons and holes even at room temperature. Henry Joseph Round first demonstrated this in 1907 when he observed yellowish light as a result of electroluminescence from a silicon carbide (SiC) crystal. He was investigating the crystal for use as a solid-state rectifying detector in a crystal detector radio [1]. Investigation and development of the process for producing SiC ensued in the following decades and by the late 1960s higher quality SiC films were being produced [2]. Even so, the best blue p-n junction LEDs of this era had only 0.005% electrical to optical power efficiency [3]. By the time the most highly efficient SiC LEDs had been demonstrated, with 0.03% efficiency emitting at 470 nm, gallium arsenide phosphide (GaAsP) diodes had already proved a more efficient material and therefore work on SiC LEDs ceased.

Using GaAsP, Holonyak *et al* began the era of viable visible LEDs operating at room temperature in 1962 [4]. Only 6 years later, in 1968, the Monsanto corporation was selling GaAsP p-n junction LEDs emitting red light for use in calculators, wristwatches and other applications. This was the first mass production of LEDs. These LEDs are currently used for low cost and low brightness applications, such as indicator lamps, due to their limited brightness. This is because the high density of dislocations between the GaAsP epilayer and the GaAs substrate results in a low external efficiency of 0.2% or less for these devices [5, 6].

The semiconductor used for contemporary white lighting LEDs is Gallium Nitride (GaN) and this material is the basis for the sources used in this thesis. In 1968, James Tietjen of Radio Corporation America (RCA) wanted to design a flat television. In order to achieve this he decided to use LEDs as they were a compact source of light. However, bright blue LEDs were not available like red and green LEDs at the time. Tietjen encharged Paul Maruska, a member of his group, with the responsibility of discovering a method for growth of single crystal GaN, which Tiejten believed would produce blue light. Maruska and Tietjen made numerous contributions to the understanding of GaN, notably producing the first single crystal film [7]. However, it was not until 1971 that electroluminescence was first demonstrated in GaN by Pankove *et al.* [8]. The inability to produce p-type conductivity in GaN and its inefficiency caused research into these devices to almost halt. Although work had ceased elsewhere research continued in Japan. In 1989 the first true p-type doping and p-type conductivity was achieved by Amano *et al.* [9]. Over the following year advances in p-type doping, activating Mg dopants and superlattice doping specifically, paved the way for efficient p-n junction LEDs [10, 11]. Eventually the first feasible blue and green GaN based heterostructure LEDs were demonstrated by Nakamura *et al.* [12–14]. As part of the research group at Nichia Chemical Industries in Japan, Nakamura *et al.* demonstrated GaN based LEDs with efficiencies of 10%.

Indium gallium nitride (InGaN) is the ternary compound used along with a colour converting phosphor for white light LEDs. InGaN has some interesting material properties which are still being investigated. One of these properties is the high efficiency of InGaN despite the high concentration of dislocations within the InGaN/GaN epitaxial film. These threading dislocations are as a result of the use of sapphire and SiC as substrates for GaN and InGaN epitaxial film. Previous to the discovery of highly efficient InGaN LEDs it was thought that LEDs required dislocations of $< 10^3$ cm^{-2} in order to be efficient [15]. Current dislocation densities in InGaN are approximately 10^9 cm^{-2}. Despite the number of dislocations found in InGaN LEDs they still have comparable performance with other arsenide and phosphide LEDs [9]. The high efficiency of GaN and InGaN materials is believed to be as a result of the short diffusion length of holes and low electrical activity of dislocations. Another proposed cause of the high efficiency of InGaN LEDs despite dislocations, is the In content [16]. If carriers are trapped in local minima as a result of the In then they will not reach dislocations and will eventually recombine. However, an understanding of the exact nature of the high efficiency of InGaN material has still not been

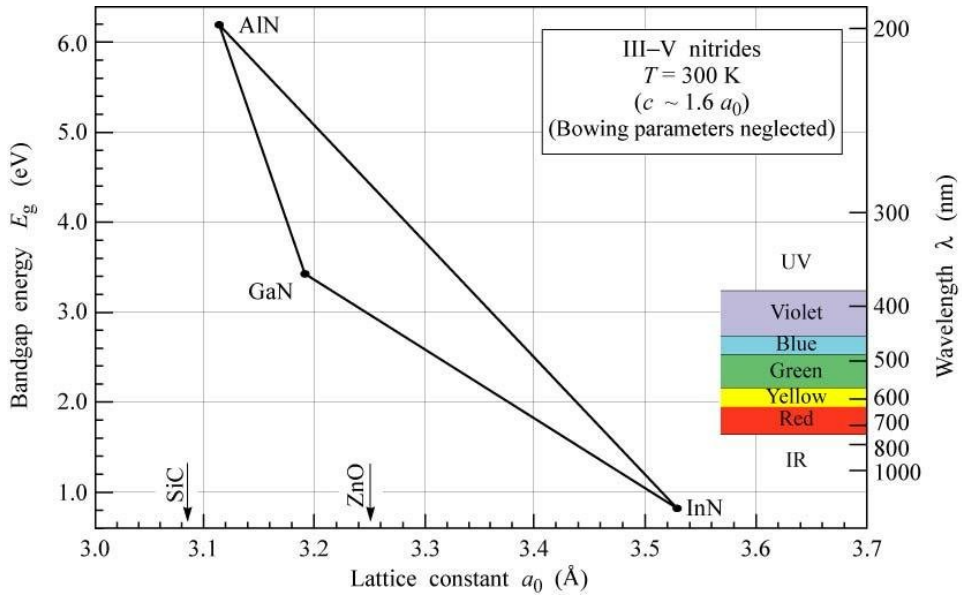

Figure 1.1: Room-temperature bandgap energy, E_g, and emission wavelength versus lattice constant for the AlInGaN-Nitride alloy system [19].

derived [17, 18]. As can be seen in Fig.1.1, InGaN LEDs should in theory be able to produce light covering the full visible spectrum. However, it is difficult to produce high quality InGaN where In is of a high proportion. This is partly due to the In re-evaporating from the growth surface.

With all of the progress that has been made with the brightness and efficiency of LEDs they are now finding use in numerous applications such as car headlights, street lamps, traffic lights and several other fields. GaN based lighting is a safe and efficient means of modernizing existing lighting infrastructure and could reduce lighting energy requirements to 1/5 of their current consumption [20]. The prospective ubiquity of GaN based lighting has given rise to the idea of VLC, where the visible spectrum augments the already congested radio frequency (RF) spectrum to transmit data [21].

1.2 Operation of light-emitting diodes

The three material types in solid-state physics are conductors, insulators and semiconductors. LEDs are fabricated from semiconductors. In these three material types, there exists a conduction band and valence band. Electrons in the conduction band can flow freely through the material whilst valence electrons are bound to the orbit of their associated atom. Between the conduction and valence band exists a bandgap of forbidden energy levels for both insulators and semiconductors. With conductors, there is no band gap and therefore electrons continually occupy the conduction band, this means the material is able to conduct electricity easily. Insulators have a large band gap and in these materials the valence band is filled with electrons whilst the

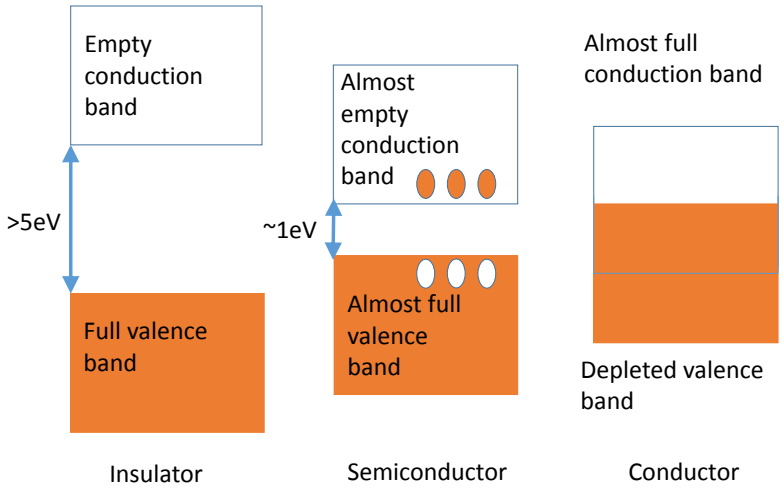

Figure 1.2: Difference in energy level overlap shows for the conduction and valence bands for insulators, semiconductors and conductors.

conduction band remains empty. Due to this, no electricity is conducted through an insulator. Finally, semiconductors, as the name indicates, have conduction properties between that of conductors and insulators. There exists a small bandgap in semiconductors, which electrons can overcome with the addition of thermal energy or light absorption resulting in electron flow via the conduction band. The bandgap energies for each material are depicted in Fig.1.2.

The most commonly used semiconductor in electronics is silicon (Si). Si is known as an elemental semiconductor as it contains only one element. Other semiconductors such as Gallium arsenic (GaAs) contain two elements and are described as binary compound semiconductors. Combining elements in this way makes it possible to manipulate the band structure of the material. In order to change the conductivity of a semiconductor a process called doping is utilized. To explain doping, let us firstly consider a pure Si lattice. When all the atoms in a material's lattice come from the same element, in this case Si, this is defined as an intrinsic semiconductor. At room temperature, intrinsic semiconductors have some free carriers due to thermal excitation or light absorption exciting electrons into the conduction band and creating an electron hole pair. Even so, the net charge of material will be zero as every negatively charged electron in the conduction band has a corresponding positively charged hole in the valence band. Si is part of group IV in the table of elements meaning it has 4 valence electrons for each atom. Each Si atom, as part of a lattice shares an electron with each of its 4 neighbours. P-type doping is the exchange of some of the Si atoms for elements from group III in the table of elements, such as Boron (B). This means only 3 covalent electrons exist, the absence of the fourth electron causes the material to become positively charged. This atom from group III is called an acceptor as it accepts electrons into the hole created by the absence of the fourth electron. Current is able to flow by the movement of electrons into this hole. As an electron moves to annihilate an existing hole it creates a hole at its previous location, moving the hole through the lattice. The effects of

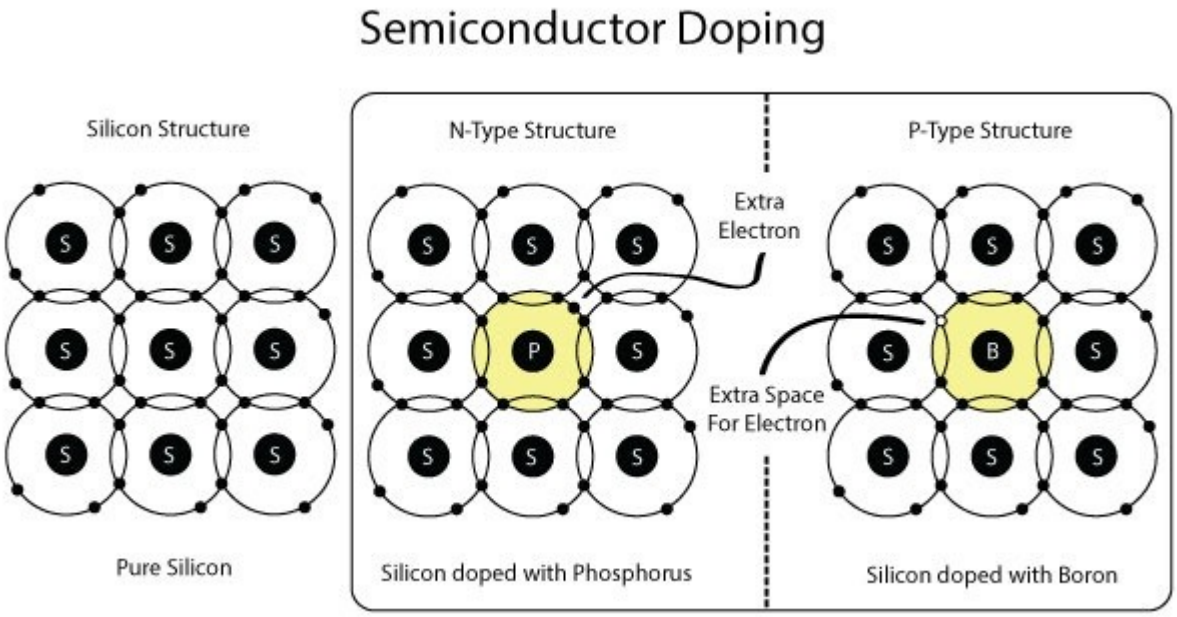

Figure 1.3: The effects on the material lattice of Silicon from Phosphorus and Boron doping can be seen. With n-type an extra electron is available, whereas, p-type creates a hole for conduction [22].

doping on the lattice can be seen in Fig.1.3. N-type doping is also depicted in Fig.1.3. In this case a Phosphorus (P) atom, know as a donor atom due to it donating an electron, replaces a Si atom. Phosphorus atoms have 5 valence electrons and only 4 of these are required for covalent bonds, therefore, the excess electron can move freely through the lattice conducting electricity. n-type material has a net negative charge.

As Si is doped new energy levels appear in the band diagram. The inclusion of acceptors in p-type doping creates acceptor energy levels just above the valence band. It is then easier for electrons to be excited and occupy this energy state leaving a hole in the valence band. A similar situation arises in n-type doping, however, the new energy levels are close to the conduction band and excitation of electron then results in that electron moving from the donor energy level into the conduction band where it is then free to move through the crystal. Fig.1.4 shows the position of the donor and acceptor energy levels in n-type and p-type doping. The following section will show how this process of doping intrinsic semiconductors facilitates light emission.

1.2.1 Electroluminescence

The physical process for producing light in LEDs is called electroluminescence. If an LED is under bias conditions the injected electrons move through the lattice of the semiconductor spontaneously recombining with holes. The electron moves from a higher energy state in the conduction band releasing energy in the form of light or heat and recombines with a hole in the

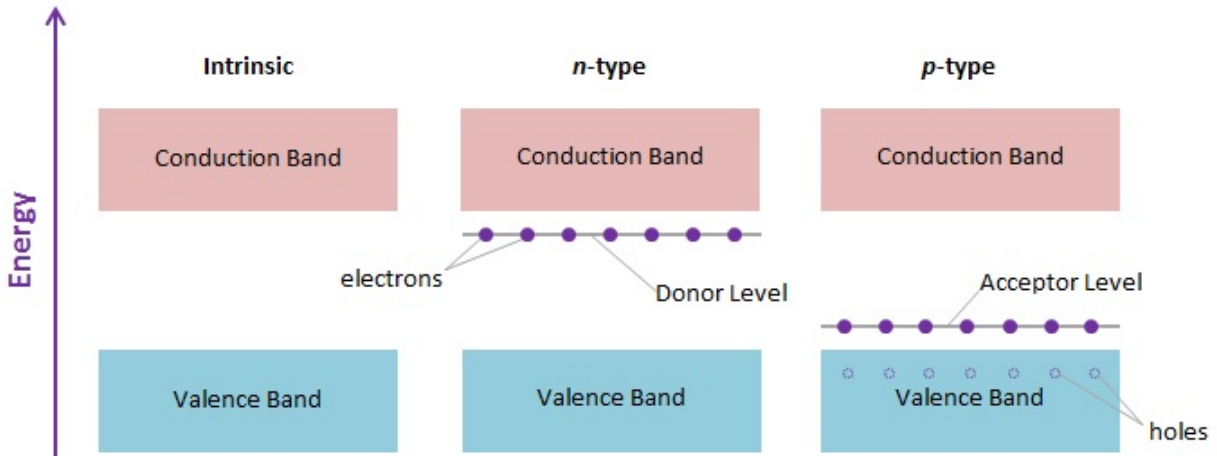

Figure 1.4: New energy levels are created within the forbidden bandgap after doping. [23].

valence band. When light is emitted this process is called electroluminescence and the energy emitted from this recombination, approximately equal to the energy band gap, is described by Eq.1.1.

$$E_g = E_c - E_v \tag{1.1}$$

Where E_g is band gap energy, E_c is minimum energy level of the conduction band and E_v is the maximum energy of the valence band. The wavelength of the emitted photon can be calculated from the energy released by the electron which is approximately equal to the bandgap energy. This is shown in Eq.1.2. Therefore, materials with different bandgaps emit different wavelengths of light and bandgaps can be engineered to produce different wavelengths using compound semiconductors.

$$E \approx E_g \approx \frac{hc}{\lambda} \tag{1.2}$$

Where E is the energy of the emitted photon, c is the speed of light in a vacuum, h is Planck's constant and λ is the wavelength of the emitted photon. Semiconductors can be split into two broad categories: Indirect and direct bandgap. The difference between these two types can be seen in Fig.1.5. With direct bandgap semiconductors the lowest energy level in the conduction band aligns with the highest energy in the valence band in k-space. As Fig.1.5 shows this is not the case for indirect bandgap semiconductors. As electrons tend to relax to the lowest energy level in the conduction band and holes tend to relax to the highest energy level in the valence band this results in the carriers being misaligned in k-space for indirect semiconductors. As a result there is extra energy required for an electron and hole to align and recombine. This energy is required in the form of a phonon to change the momentum of the electron so that it can then make the transition. This means that recombination with indirect bandgap materials is less likely than with direct bandgap materials. Therefore, direct bandgaps are a more efficient

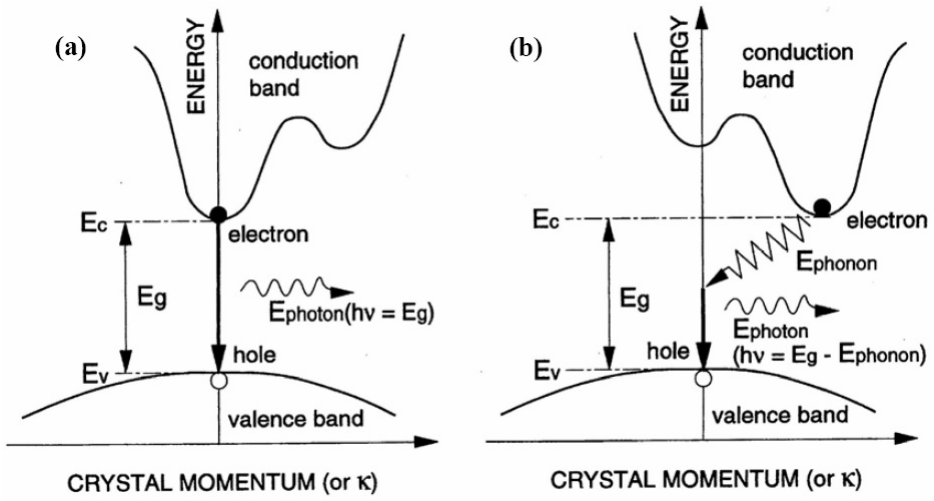

Figure 1.5: a) The alignment of the minimum energy of the conduction band and maximum in the valence band for a direct bandgap semiconductor b) This minimum and maximum is not aligned with indirect bandgap materials [24].

choice for the emission of photons from electroluminescence. The next section will discuss the combination of p-type and n-type semiconductors to facilitate carrier injection and efficient recombination within an LED.

1.2.2 The p-n diode

The basic design of an LED is based on the p-n junction diode. A p-n junction is formed when an area of p-type semiconductor is grown adjacent to an area of n-type semiconductor. The heavily doped regions are formed using epitaxial growth, meaning they are grown layer by layer atomically directly onto a substrate. The junction formed at the p and n doped materials is known as a homojunction when the same semiconductor is used on both sides.

At the boundary between the p and n type materials there exists a region depleted of both electrons and holes named the depletion region. This region occurs due to diffusion of electrons from the n-doped material to the p-doped side where they recombine with holes in the acceptors. A reciprocal process occurs with the diffusion of holes into the n-doped material and the subsequent recombination of the holes with the excess electrons from the donors. This results in statically charged atoms and a depletion of mobile charge carriers. The result is a potential arising from the statically charged acceptor and donor atoms called the diffusion voltage given by Eq.1.3.

$$V_D = \frac{kT}{e} \ln \frac{N_A N_D}{n_i^2} \tag{1.3}$$

Where n_i is the intrinsic carrier concentration of the semiconductor, N_a and N_d are the acceptor and donor concentrations respectively, k is Boltzmann's constant, T is temperature and e

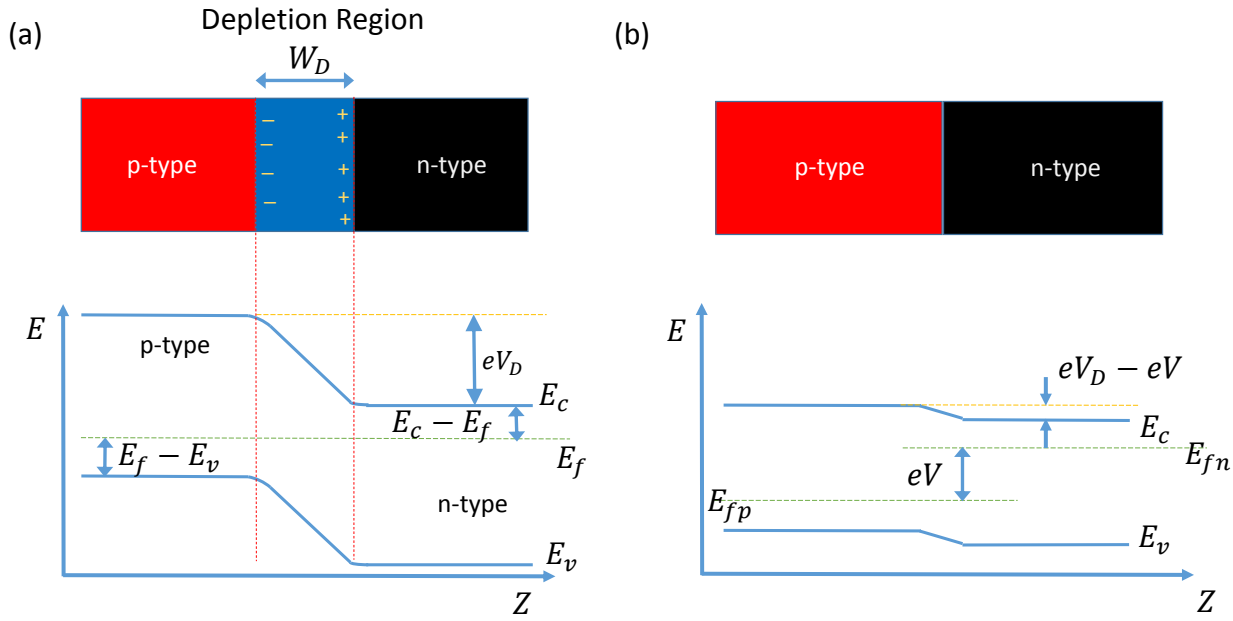

Figure 1.6: a) The p-n diode under zero bias showing the depletion region and the corresponding energy band diagram where z is the spatial dimension perpendicular to the junction. b) The junction is now shown under forward bias with a reduced depletion region width and changed energy band diagram.

is elementary charge. This diffusion voltage is the voltage that must be overcome by a carrier to reach the neutral region of the other conductivity type, that is, the diffusion voltage must be overcome to conduct current. The p-n junction under zero bias is shown in Fig.1.6.a) with the depletion region indicated in blue and the result of the diffusion voltage seen in the change of the conduction and valence band across this region.

The Shockley equation describing the current-voltage (I-V) characteristics of an ideal p-n junction diode with cross-sectional area A is given by Eq.1.4.

$$I = I_s(e^{\frac{eV}{kT}} - 1) \quad \text{where} \quad I_s = eA\left(\sqrt{\frac{D_p}{\tau_p}}\frac{n_i^2}{N_D} + \sqrt{\frac{D_n}{\tau_n}}\frac{n_i^2}{N_A}\right) \tag{1.4}$$

Where $D_{p,n}$ and $\tau_{p,n}$ are the electron and hole diffusion constants and minority carrier lifetimes respectively and V is the applied voltage. The diode acts like a rectifier, opposing current flow in one direction and facilitating it in the opposite direction. This occurs when the diode is reversed bias because the applied biasing voltage further enhances the barrier seen by carriers due to the diffusion voltage. When a voltage V is applied in the forward bias this reduces the change in the conduction and valence bands across the junction as seen in Fig.1.6.b). This makes it easier for holes and electrons to pass across this region and conduct current. Under forward bias conditions $V \gg \frac{KT}{e}$ and therefore $exp(\frac{eV}{kT} - 1) \approx exp(\frac{eV}{kT})$ and the Shockley equation can be

written as in Eq.1.5.

$$I = eA\left(\sqrt{\frac{D_p}{\tau_p}}N_A + \sqrt{\frac{D_n}{\tau_n}}N_D\right)(e^{\frac{eV-eV_D}{kT}}) \tag{1.5}$$

As can be seen by looking at the exponent of the exponential function in Shockley's rewritten equation, the current strongly increases as the applied voltage approaches the diffusion voltage. The voltage required to reach this strong increase is called the threshold voltage (V_{th}) and is approximately equal to V_D. For an ideal diode V_{th} is approximately equal to the bandgap energy over the elementary charge shown in Eq.1.6.

$$V_{th} = \frac{E_g}{e} \tag{1.6}$$

After the forward bias voltage surpasses V_{th} electrons and holes can easily diffuse through the depletion region and into the p and n-type regions. After reaching these regions they will recombine with the majority carriers in these regions emitting light. The next section will elaborate further on the design and structure commonly found in LEDs.

1.2.3 Quantum well structure

One disadvantage of p-n diodes is their large area, this is a disadvantage when it comes to radiative recombination and efficiency of an LED. As minority carriers are dispersed over a large area reducing the carrier concentration, this also reduces the recombination rate. The recombination rate is given by the bimolecular recombination formula in Eq.1.7.

$$R = Bnp \tag{1.7}$$

Where B is the bimolecular recombination coefficient, n is the electron carrier concentration and p is the hole carrier concentration. Therefore, it is evident from Eq.1.7 that the recombination rate is proportional to the concentration of electrons and holes and that reducing these reduces the efficiency. The p-i-n diode offers a solution to this issue of low carrier concentration by confining carriers to a smaller area and increasing the concentration. The p-i-n diode works by sandwiching an area of intrinsic semiconductor with a small bandgap between heavily doped p and n regions of a semiconductor with a large bandgap. This creates two large bandgap cladding regions which confine the carriers to the active region of the small bandgap intrinsic semiconductor. This is known as a double heterostructure, 'hetero' from the two dissimilar semiconductors forming a junction and 'double' from the fact two heterojunctions are used. The process of confinement can be understood by looking at the energy band diagram of a regular p-n junction diode compared with that of a double hetero structure device shown in Fig.1.7.a) and b). Fig.1.7.a) shows a homojunction under forward bias and Fig.1.7.b) shows the double heterostructure also under forward bias. It can be seen schematically the double heterostructure

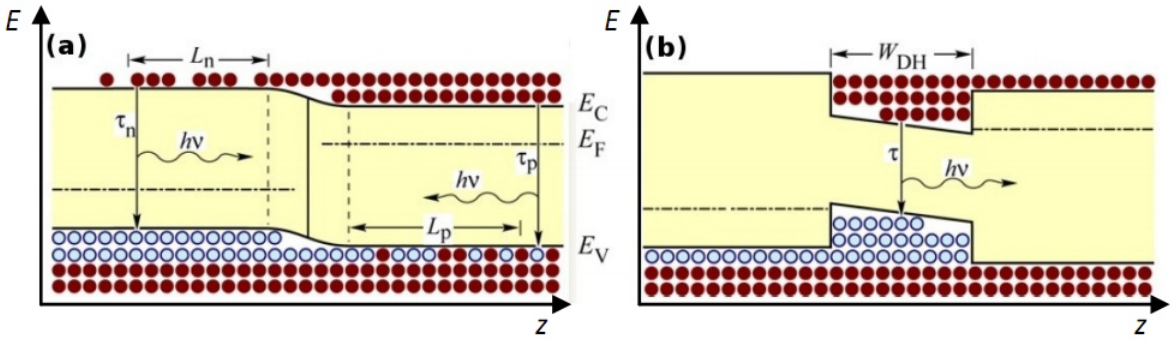

Figure 1.7: a) The p-n diode under forward bias with carriers spread across the junction. b) p-i-n diode with carriers concentrated in the intrinsic active region due to energy bandgap changes [16].

confines the diffusing carriers in a smaller area where recombination is more efficient due to higher carrier concentration. The width over which the carriers diffuse is much greater in the homojunction.

If the active region is made small enough so that its length is comparable with the de Broglie wavelength associated with the mass and momentum of the confined charge carriers, the active region becomes a quantum well. The de Broglie wavelength is given by Eq.1.8.

$$\lambda = \frac{h}{p} = \frac{h}{\sqrt{2m^* kT}} \tag{1.8}$$

Where m^* is the carrier effective mass and p is the momentum. In this scenario, the carriers are confined to movement in two dimensions as they cannot move in the z direction. The result of this confinement is a change in the allowable energy states for such a carrier. The energy levels the carrier can occupy no longer form a continuous band but instead are replaced with discrete energy levels. This can be understood by imagining the active region is a one dimensional 'potential well' with infinite potential either side of the well confining carriers inside the well where they have zero potential. This is depicted in Fig.1.8. As the carrier cannot escape the well and must be found there, boundary conditions can be applied to schrödinger's equation with ψ = 0 for W = 0 and W = L. Therefore, Schrödinger's equation can be solved to give Eq.1.9

$$E_n = \frac{n^2 h^2}{8mL^2} \tag{1.9}$$

Where n is an integer and L is the width of the quantum well. Therefore, the permissible energy levels are found to be discrete and defined by the integer n. As a result of this carefully controlling the length of the quantum well can manipulate the wavelength of the emitted photons.

Using quantum wells can cause diffusing carriers to fill the active region and cause carrier overflow out of the region. To compensate for this effect in reality most LEDs used multiple evenly spaced quantum wells called multi-quantum wells (MQW) to generate high carrier con-

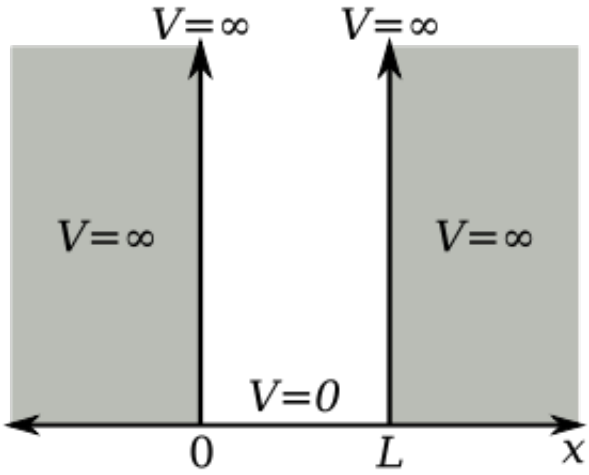

Figure 1.8: Theoretical one-dimensional potential well where a region of zero electrical potential is bounded by barriers of infinite potential [25].

centration.

1.3 The development of lasers

The word laser is an acronym standing for light amplification by stimulated emission radiation. It was in 1917 when Einstein first proposed stimulated emission as a distinguishable form of emission [26]. This provided the theoretical basis for lasers but the laser was not to be demonstrated for over forty years. The first demonstration of amplification through stimulated emission was at microwave frequencies. In 1954 Townes demonstrated microwave amplification by stimulated emission radiation (maser) when he directed excited ammonia molecules into a resonant cavity resulting in amplification of a wavelength at a little over one centimetre [27]. The power of the first maser was very small, only amounting to tens of nanowatts. Shortly after this demonstration research groups at IBM and Columbia University, amongst others, tried to create the first laser. In 1960, working at Hughes laboratory, Theodore H. Maiman produced the first laser [28]. Using a flash lamp to optically pump a ruby rod, Maiman demonstrated pulsed operation of the first laser which produced red light.

Later in 1960 Javan *et al.* produced the first continuous wave (CW) laser, which was also the first gas laser [29]. Using helium-neon gas the laser demonstrated amplification at 1.15 μm and was the first in a large number of discharge excited gas lasers to emerge. One of the most important of these lasers was the first CW visible helium-neon laser. Whilst working at Bell laboratories Alan White and Dane Rigden developed the helium-neon laser at 1.15 μm designed by Javan *et al.* [30]. Observing the spectrum of emission from the helium-neon plasma they noticed a spectral line at 632.8 nm. After adding reflective mirrors at this wavelength they were able to show the laser working at 632.8 nm.

In 1961 Johnson and Nassau demonstrated the first neodymium-doped solid state laser [31].

The following year Johnson *et al.* published their research reporting the operation of a CW solid state laser at room temperature at 1.06 μm [32]. There was further development in solid state lasers in 1962 reported by Robert N. Hall. Whilst attending the Solid State Devices Research Conference in July, Hall witnessed a talk explaining the improved efficiency in GaAs LEDs doped with Zinc impurities and cooled to liquid nitrogen temperatures [33]. Realizing the implications for lasers Hall worked on developing a GaAs laser diode and within two months the first semiconductor laser had been manufactured [34]. Although this was the first semiconductor laser diode it was operated with microsecond pulses and was cooled to liquid nitrogen temperatures. By 1977 more practical laser diodes where available, Hartman *et al.* published work showing GaAlAs lasers with a mean lifetime of 100 years under CW conditions [35].

As lasers have developed since the initial Ruby laser in 1960 towards the modern semiconductor lasers available today so have their applications. An important milestone in this development was the invention of the InGaN blue/violet laser diode by Nakamura in 1996 [36]. InGaN lasers have since been developed to emit at 450 nm allowing the combination of blue, green and red lasers to produce white light. Laser-based illumination has already been shown to produce high quality colour rendering for white light illumination using multiple coloured sources and using phosphor colour converters [37, 38]. Therefore, dual purpose lighting, where lasers are used for VLC as well as illumination, has become a feasible option for next generation optical communications. In addition to this potential use lasers have already been used in numerous fields from retina treatment to the study of light-matter interactions for research [39, 40].

1.4 Operation of lasers

The fundamental process for emission of light in a laser is different from that of an LED. Laser is an acronym standing for light amplification by stimulated emission radiation. Photons emitted from a laser are as a result of stimulated emission as opposed to the spontaneous emission process present in LEDs. To understand this process, a basic understanding of quantum mechanics is required. The simplest example of atomic structure is the hydrogen atom. The hydrogen atom has only one proton and therefore only one electron orbits the nucleus. Consulting Fig.1.9 we can see the inner most orbit $N = 1$ where the energy level is labelled E_1. This is the ground state with the lowest energy level. As the orbit number increases so does the energy of the electron and these levels above the ground state are called excited states. All of these energy levels are discrete.

The different energy levels described by the orbit state of the electron are not the only determining factor for the discrete energy levels in matter. The nucleus of the atom itself has energy, molecules of atoms have energy corresponding to their rotation and also to the vibrational energy of the atoms within the molecules itself. All of these energy levels are used in different lasers to produce emission. Lasers with emission from ultraviolet to infrared, such as neodymium lasers,

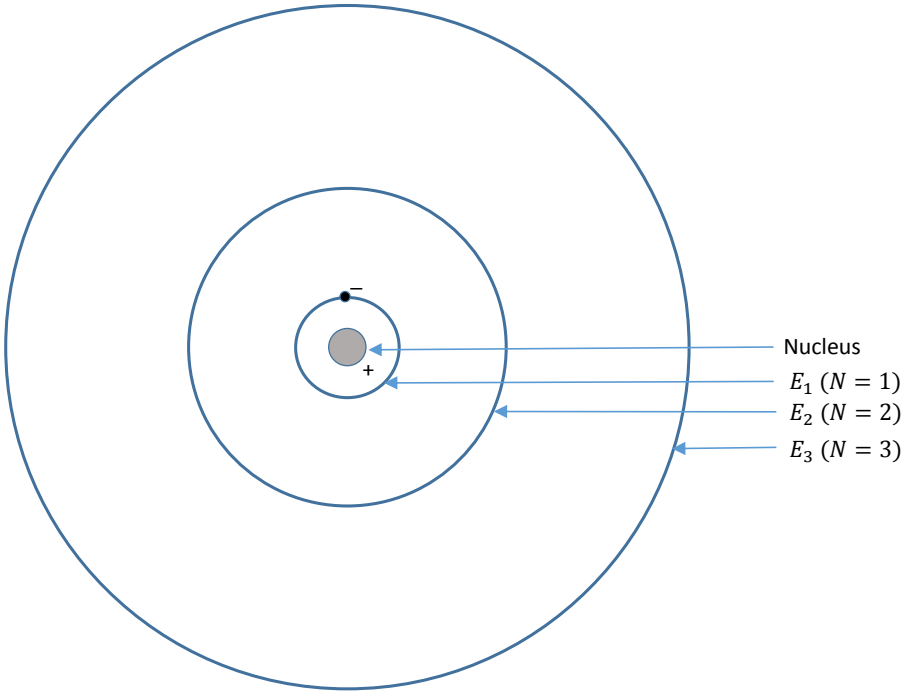

Figure 1.9: Energy levels for different orbital states of a hydrogen atom.

are dependent upon electron transitions, whereas a carbon dioxide laser emitting infrared light utilises transitions between different vibrational energy states of its atoms.

Within solids, liquids and gases atoms are constantly colliding causing changes in their energy levels. These changes do not all cause emission of light. The transitions that are fundamental to lasers are optically allowed transitions. When a photon is absorbed or emitted it must satisfy the resonance condition $E = hv$ where E must equal the transition energy between two states given h is Planck's constant and v is the frequency of the emitted or absorbed photon.

1.4.1 Absorption, spontaneous emission and stimulated emission

As was stated in the previous section as well as emitting photons it is possible for matter to absorb photons. When a photon is absorbed by an electron it will transition from its current energy state to a higher energy state. In order for absorption to be possible an atom must be in a lower energy level and the energy of the absorbed photon must satisfy $E = hv$ where E is the transition energy between the two involved states. The probability of absorption is determined by Einstein's absorption coefficient and the population of the lower energy level.

As is discussed in section 1.2.1, it is possible for an excited atom or molecule to drop energy levels spontaneously emitting a photon in the process without any stimulus. If a photon is released by these means the energy of the photon will be equal to the difference between the two energy states and its frequency will be determined by $E = hv$. Spontaneous emission occurs at a rate independent of the population of an energy state. It is determined solely by the related

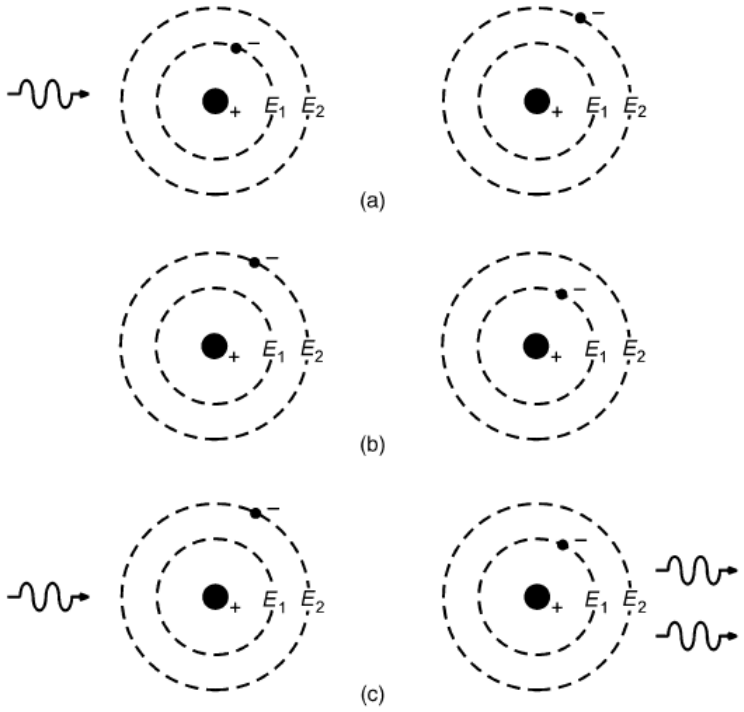

Figure 1.10: Absorption and emission processes :a) absorption; b) spontaneous emission: c) stimulated emission [41].

Einstein coefficient.

Lasers are dependent upon the process of stimulated emission for their operation. Unlike spontaneous emission, where a photon is emitted without external stimulus of the atom, a photon is required to interact with an excited atom or molecule to produce a new photon in a laser. The stimulating photon must have energy equal to the transitional energy between the excited state and a lower energy level. After interacting with the photon the atom or molecule will drop to the lower energy level emitting a photon with the same frequency, phase and polarization as the stimulating photon. The rate of stimulated emission is proportional to the population of the excited energy level and to the related Einstein coefficient. The three processes are shown in Fig.1.10.

As lasers depend on stimulated emission for their operation and LEDs depend on spontaneous emission this results in fundamental differences in performance. Looking at the typical L-I characteristics of an LED in Fig.1.11 it can be seen that increasing the current through the device causes the power to increase until a maximum output power is reached and increasing the current beyond this point will result in a reduction in power. Looking at the L-I curve of a typical laser in Fig.1.12 shows the output power continually increasing with drive current. If the drive current of this device was to be increased further eventually the output power of the laser would saturate, however, it would not experience the same reduction as the LED power does. This is due to the difference between an LED internal quantum efficiency (IQE) and a laser IQE.

Eq.1.10 shows the formula for the IQE of an LED and Eq.1.11 shows the formula for IQE

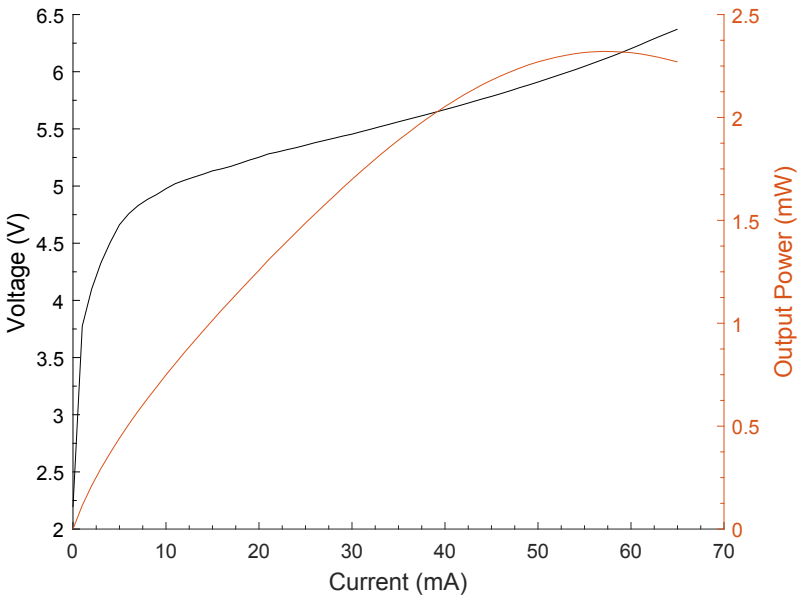

Figure 1.11: LVI curve of violet μ-LED at room temperature.

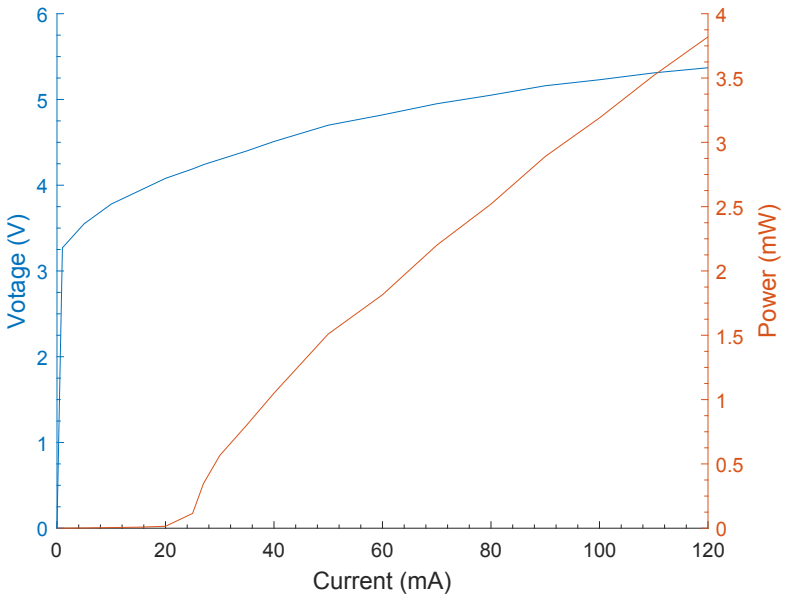

Figure 1.12: LVI curve of blue laser at 17°C.

of a laser.

$$\eta_{IQE} = \frac{Bn^2}{An + Bn^2 + CN^3} \tag{1.10}$$

where n is the carrier density, Bn^2 is the radiative recombination rate, and An and Cn are the Shockley Read-Hall and Auger recombination rates, respectively. At high currents, Cn dominates and reduces η_{IQE}.

$$\eta_{IQE} = \frac{Bn^2 + R_{st}N_{ph}}{An + Bn^2 + CN^3 + R_{st}N_{ph}} \tag{1.11}$$

Similarly to the LED formula for IQE, Eq.1.11 for laser IQE contains terms for the radiative and non-radiative recombination which are dependent on the carrier density n. However, there is an additional term $R_{st}N_{ph}$. This is the stimulated emission rate multiplied by the cavity photon density. As dominant process of emission in the laser is stimulated emission as opposed to spontaneous emission when the current is increased in a laser beyond threshold the photon density term, N_{ph}, increases at much quicker rate than the carrier density. Therefore, the dominant term affecting the IQE of a laser is not the Auger term Cn but the stimulated emission term $R_{st}N_{ph}$. Hence, the difference in the IQE and output power as a function of current for lasers and LEDs. The fact that lasers have a higher efficiency than LEDs at high drive current is one advantage of lasers. The efficiency droop of LEDs and other advantages of lasers are discussed further in section.3.2.

1.4.2 Population inversion

In order for stimulated emission to be the dominant process in a light source there must be enough atoms or molecules in an excited state to allow stimulated emission to occur at a high enough rate. As discussed in the previous section the rate of stimulated emission is dependent upon the population of the excited energy level in the lasing medium. This is why a population inversion is required. To explain this lets use the simple two level laser model shown in Fig.1.13. Taking as an example a neodymium-doped yttrium aluminium garnet laser with a wavelength of 1064 nm, the transition energy given by $E = hv$ is approximately 1 eV. Given this and assuming the laser is at room temperature we can use Eq.1.12 to calculate the population of N_2 relative to N_1.

$$\frac{N_2}{N_1} = e^{[-(E_2 - E_1)/kT]} \tag{1.12}$$

The result gives $N_2 = 1.5\text{x}10^{-17}N_1$. The population of the lower energy level is much greater than the population of the upper level for the two level system. Given the rate of absorption and stimulated emission are proportional to the population of lower and upper states respectively, the likelihood of absorption is much greater than the likelihood of stimulated emission. Lasers require the rate of stimulated emission to be higher than the rate of absorption and spontaneous emission. Therefore, the lasing medium must be altered such that the population of N_2 is greater than that of N_1. As N_2 is depleted also by spontaneous emission there is a certain value of $N_2 - N_1$ which produces lasing action known as the lasing threshold or inversion threshold. This population inversion is achieved by what is known as pumping.

Pumping the laser medium can be achieved through optical or electrical pumping. Where

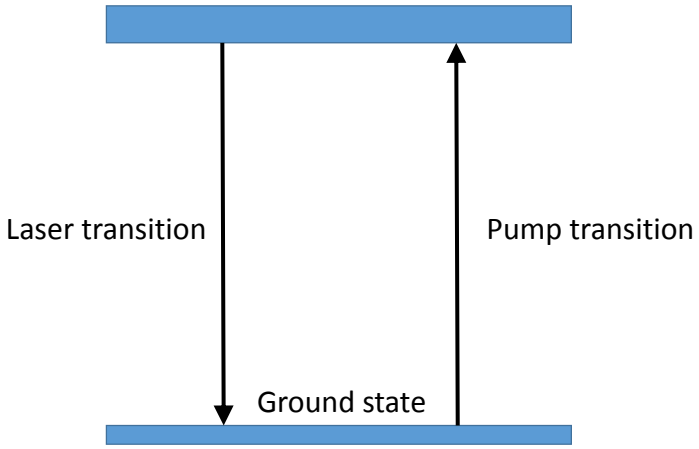

Figure 1.13: Two level laser system.

optical pumping is used the photons from a pumping source are absorbed by the lasing medium exciting the atoms and causing them to move to the higher energy state. As the atoms populate the higher energy states population inversion is achieved. Alternatively, electrical pumping can be used. In this case electrical current is used to populate the upper state. This is the method used mostly with semiconductor lasers.

1.4.3 Laser resonator and threshold

The most basic design for a laser resonator is shown in Fig.1.14. The lasing medium is bound by two mirrors which cause photons to be reflected back through the medium increasing the gain of the laser. At one end there is a partially emissive mirror which allows photons to escape. Not only does this resonator increase the gain of the laser it will also limit the wavelengths that are amplified to those which are resonant frequencies. Eq.1.13 describes the wavelength of these resonant frequencies.

$$Roundtriplength = 2L = n\lambda \tag{1.13}$$

Where L is the length of the resonator, n is an integer and λ is the wavelength of the wave.

Within the cavity there are optical losses associated with the mirrors and the gain medium. If the optical gain of the medium is equal to the losses experienced in the medium the laser will meet threshold conditions. Assuming steady state operation this is described by Eq.1.14.

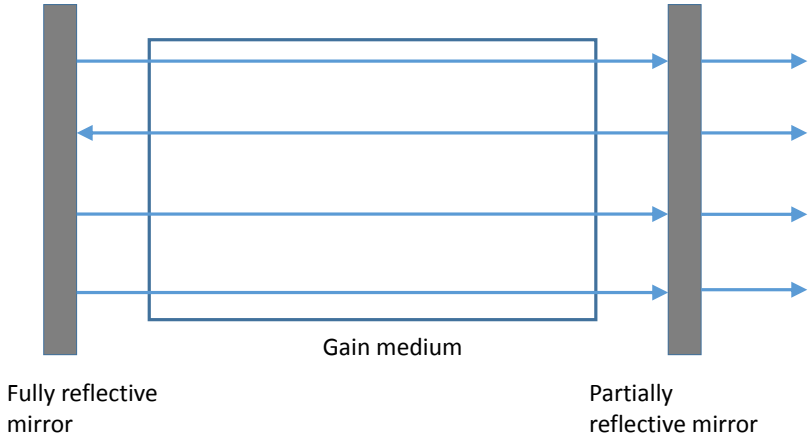

Figure 1.14: Lasing medium enclosed by mirrors.

$$R_1 R_2 e^{(2g_{threshold}l)} e^{(-2\alpha l)} = 1 \tag{1.14}$$

R_1 and R_2 are the power reflectivity of the mirrors at the ends of the cavity, l is the length of the gain medium, $exp(2g_{threshold}l)$ is the round trip threshold power gain and $exp(2\alpha l)$ is the round trip power loss. Assuming the optical loss of the cavity is constant $\alpha = \alpha_o$ the threshold gain shown in Eq.1.15 is found by rearranging Eq.1.14.

$$g_{threshold} = \alpha_o - \frac{1}{2l}\ln(R_1 R_2) \tag{1.15}$$

1.4.4 Semiconductor laser structure

A generic structure for a Fabry Perot semiconductor laser diode is shown in Fig.1.15. When charge carriers recombine in the active region the emitted photons are reflected into the active region using reflective surfaces creating a laser resonator as described in previous section. This feedback allows stimulated emission to become dominant over spontaneous emission in the active region. At the laser output the mirror is partially reflective allowing emission of photons from the active region. The active region is placed between p-type and n-type cladding regions which have a wider bandgap than the active region. This creates a quantum well and confines the carrier to the active region which in turn increase the carrier concentration in the active region making stimulated emission more probable.

From Fig.1.16 we can gain insight into the spectral output from the active region of the laser. As is discussed in section.1.4.3 there are a limited number of longitudinal modes which are resonant in the cavity this is depicted in Fig.1.16.b). However, this is not the laser spectral output. The active region has an associated bandwidth at which it will emit photons as is shown in

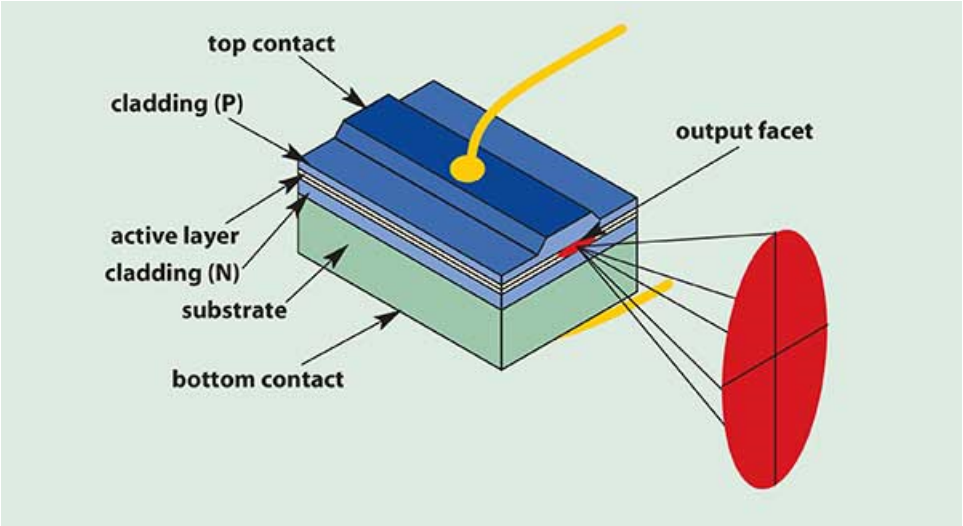

Figure 1.15: Generic structure for FP semiconductor laser [42].

Fig.1.16.a). When the bandwidth of the active region is combined with the resonant frequencies of the cavity the spectral output of the laser can then be determined by Fig.1.16.c).

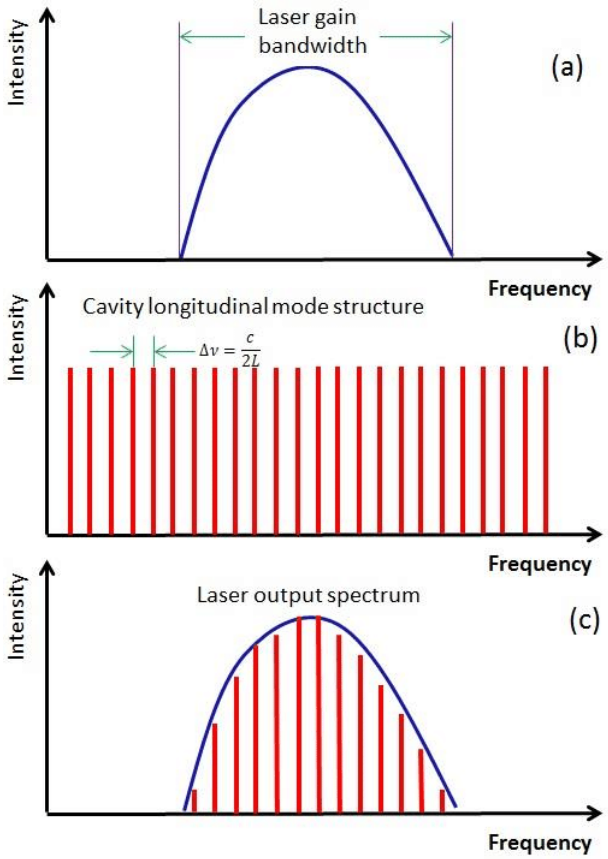

Figure 1.16: a) Laser gain bandwidth as a result of active region. b) The frequency of wavelengths which are resonant longitudinal modes of the cavity. c) Output spectrum of the laser as a result of effects from both the active region and the cavity [43].

1.5 Orthogonal frequency division multiplexing

Fig.1.17 shows a block diagram which introduces the general concept of a FSO communication system. A source is modulated at the transmitter by combining DC power with a modulated AC signal which is transduced into an optical signal before being transmitted via a free space link to a receiver which collects the signal and converts into an electrical signal before the signal is demodulated. In this thesis the bulk of the work has been concerned with making improvements to the transmitter side of the system. This has been done by using a variety of optical sources with various benefits and potential applications in VLC systems. Initially μ-LEDs were used as the source for the VLC systems in this thesis. These sources offer high bandwidth modulation with cheap production costs. However, these devices do not have the same efficiency, modulation bandwidth and output power as lasers, this is discussed in more detail in section 3.2. Therefore, the work in this thesis explores GaN-based laser diode capabilities within a VLC system as an option for improving the transmitter performance. One of the main improvements to the transmitter used in this thesis was the inclusion of complex modulation formats with advance multiplexing techniques. QAM-based OFDM was used to improve the transmitter performance and this multiplexing technique is introduced in this section. Other multiplexing techniques are also available for optical communication systems and these are briefly discussed first in this section before a more in depth discussion of OFDM is given.

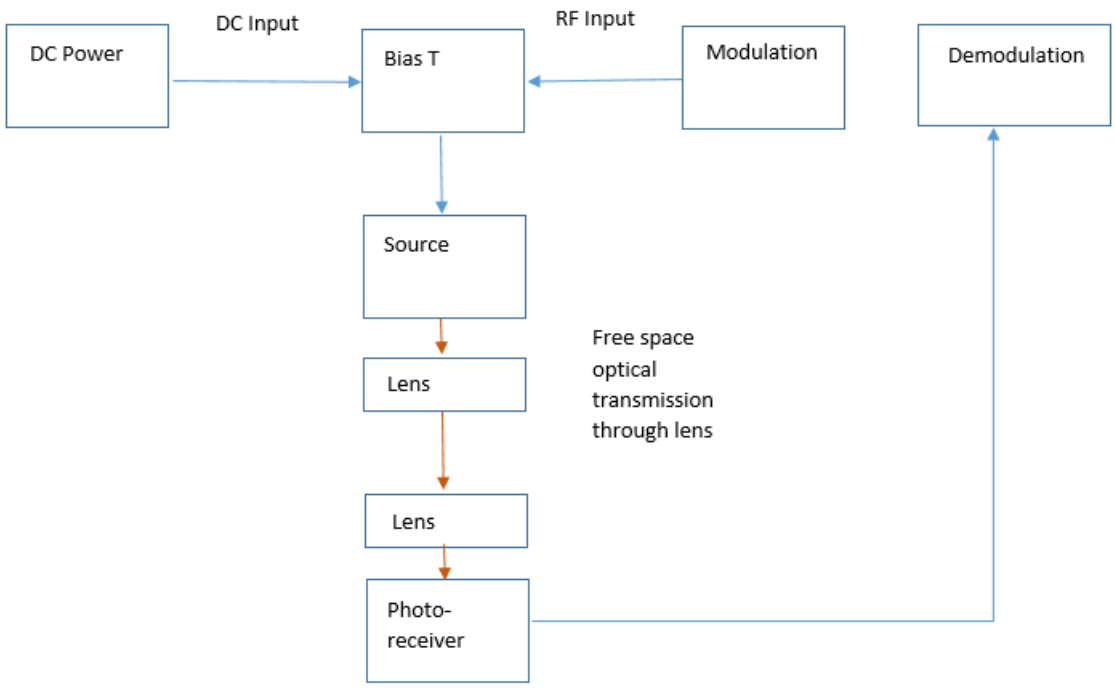

Figure 1.17: Block diagram showing concept of optical communication system.

1.5.1 Multiplexing techniques for optical communications

There are multiple dimensions available for multiplexing in optical communications. Fig.1.18 shows the five physical dimensions which can be exploited when multiplexing is desirable in optical communications.

One of these dimensions which used in current fibre optic telecommunications is TDM, where multiple signals are transmitted across the same channel link in temporal succession. This is depicted in Fig.1.19. A pulse source is modulated by different modulators, each signal then experiences a different time delay and is coupled into a single transmitted composite signal. At the receiver the signal is then demultiplexed by sampling at the correct interval and the signal is split into the different transmitted signals.

As Fig.1.19 demonstrates there is increased complexity over individual channel systems.

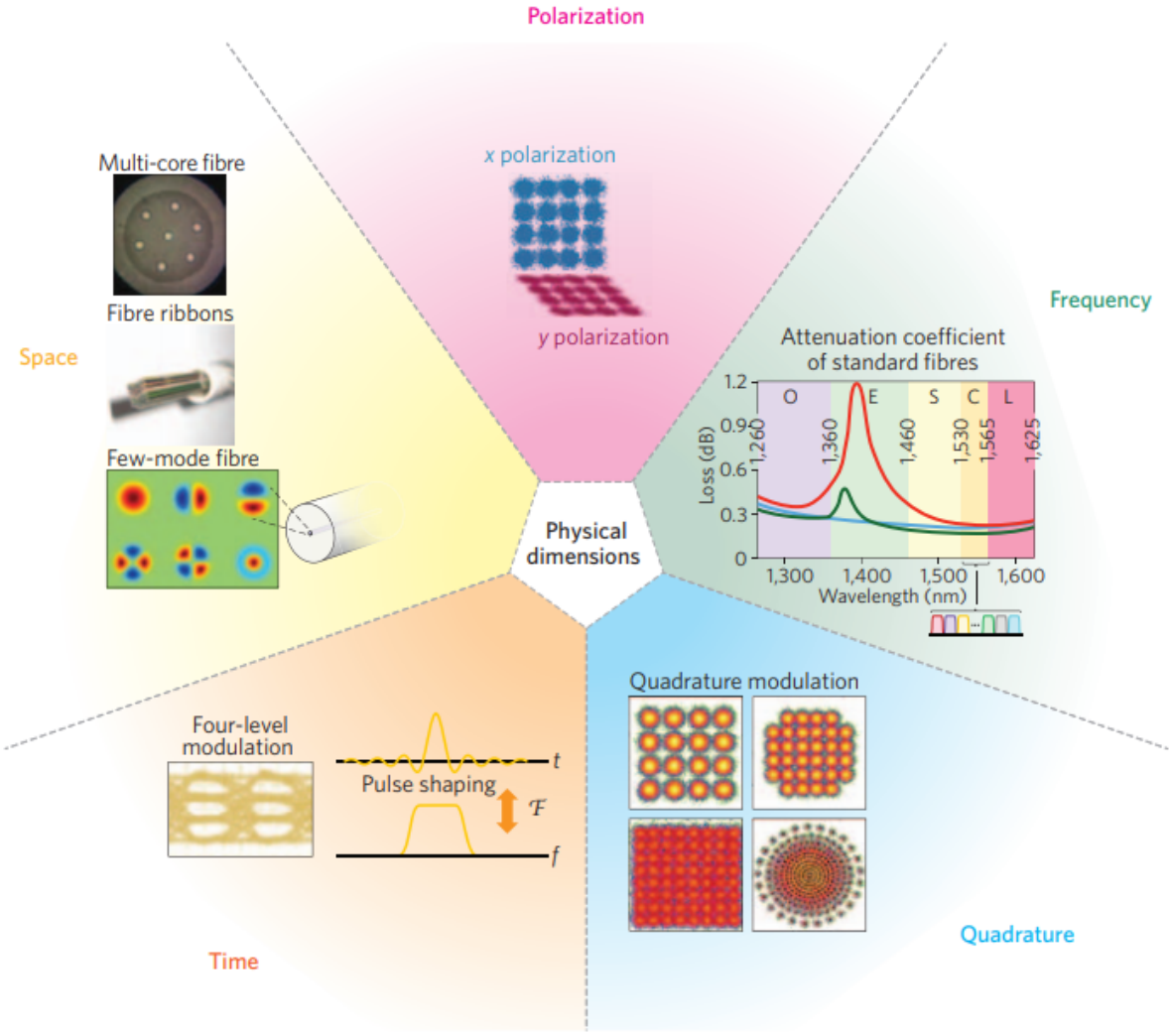

Figure 1.18: Five physical dimensions (polarization, frequency, quadrature, time and space) form the basis of all electromagnetic communication techniques. Specific examples pertaining to optical communications are shown. [44].

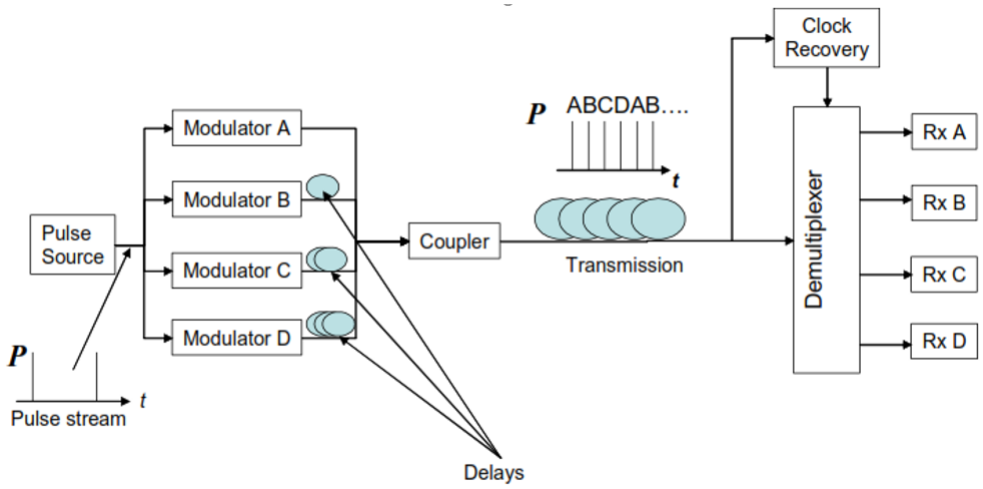

Figure 1.19: Schematic of TDM system with modulators, time delays and transmission.

Optical time division multiplexing requires a splitter, additional modulators, components for delaying and coupling the modulator outputs into one signal, a demultiplexer and additional receivers.

The number of channels that can be interleaved is limited by the width of the pulse source compared to the bit period. It is desirable that the pulse source has a short duration to allow more time within the bit period for additional channels. For example if there exists a bit period of T due to a pulse source within a 4 channel system, it is required that width be a maximum of $T/4$. In reality it must be smaller to avoid overlap of pulse tails.

Another method for increasing data rate transmission through a single channel optical communication system is WDM. WDM uses different wavelength carriers to transmit data across a single channel. At the receiver these wavelengths can me demultiplexed using filtering. Fig.1.20 shows a schematic diagram for such a system.

In the system schematic there are 4 sources at different wavelengths. Given N wavelengths, The components required are N transmitters, a multiplexer, a demultiplexer and N receivers.

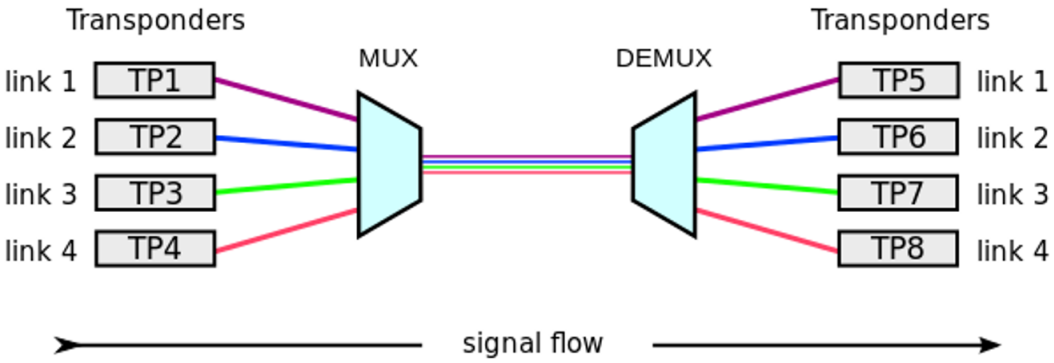

Figure 1.20: Schematic of WDM system with multiplexing and demultiplexing of different wavelengths [45].

Using this method can increase the transmission by a factor of N.

For example in silica fibre single wavelength optical transmission utilises only a fraction of the wavelengths that a silica fibre can transmit at. It is possible to fill the bandwidth of the fibre using WDM and transmit information at different wavelengths across the fibre simultaneously. The information at different wavelengths is maintained uncorrupted so long as the frequency of the sources is controlled preventing the frequency bands of the sources overlapping.

The electromagnetic polarization of a wave can also be used to create two orthogonal carriers in PDM. Fig.1.21 shows two linearly polarized waves. Similarly to WDM these waves can be transmitted simultaneously across a channel and separated at the receiver which can double the data rate.

Fig.1.18 also depicts the constellation diagram of a QAM signal using quadrature modulation. QAM is used in WiFi technology based on the IEEE 802.11 specification. It was also used as the modulation format for the VLC systems described in this thesis. QAM is a digital encoding scheme where the amplitude and phase of a carrier wave is manipulated to transfer information. A carrier modulated in such a way can be described by Eq.1.16.

$$X(t) = a(t)cos(2\pi f_c t + \theta(t)) \tag{1.16}$$

Using the angle sum trigonometric identity this can be converted to Eq.1.17 and after defining X_I and X_Q as the in phase and quadrature modulation functions we then have the solution in Eq.1.18.

$$X(t) = a(t)cos(\theta(t))cos(2\pi f_c t) - a(t)sin(\theta(t))sin(2\pi f_c t) \tag{1.17}$$

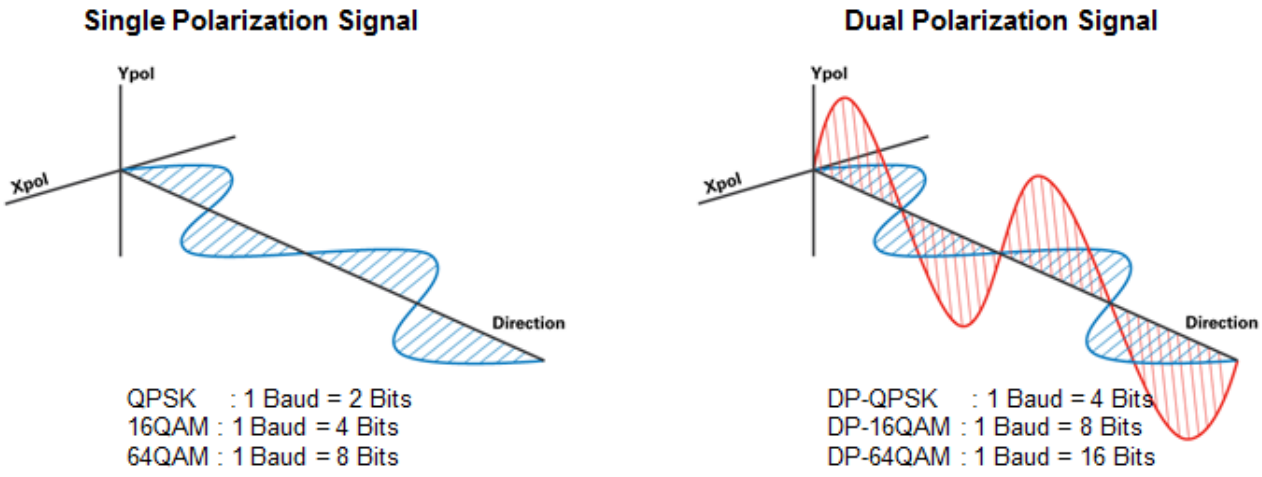

Figure 1.21: When imposed on a QPSK signal, polarization multiplexing enables one baud to carry four bits [46].

$$X(t) = X_I(t)cos(2\pi f_c t) - X_Q(t)sin(2\pi f_c t) \tag{1.18}$$

The baseband equivalent of $X(t)$ is given by Eq.1.19.

$$X_{bb}(t) = X_I(t) + jX_Q(t) \tag{1.19}$$

When taking the real part of the baseband signal multiplied by a complex carrier we return to $X(t)$, this is shown in Eq.1.20.

$$X(t) = X_I(t)cos(2\pi f_c t) - X_Q(t)sin(2\pi f_c t) = Real\{X_{bb}(t)e^{j2\pi f_c t}\} \tag{1.20}$$

There are various order of QAM such as 16-QAM, 32-QAM, 64-QAM etc. The order determines the number of bits per symbol for the modulation scheme. For example 16-QAM encodes 4 bits per symbol. Looking at the 16-QAM constellation diagram in Fig.1.22 the positions of the different symbols can be identified in the complex plane. Each of these points has a unique combination of phase and amplitude with a corresponding real and imaginary part. The I and Q axis correspond to the magnitude of the real and imaginary parts of the signal and these are determined by the $X_I(t)$ and $X_Q(t)$ the in-phase and quadrature functions.

These different positions of symbols in the complex plane can also be understood and depicted in the time domain as in Fig.1.23. This figure shows all 16 modulation symbols in the time domain. In the time domain the symbols take one of three amplitudes. This can be understood by observing the magnitudes of the points in Fig.1.22, looking at one of the quadrants it can be seen that the symbol closest to the origin has the same phase as the furthest symbol from the origin but a different magnitude this gives two of the the time domain amplitudes. The

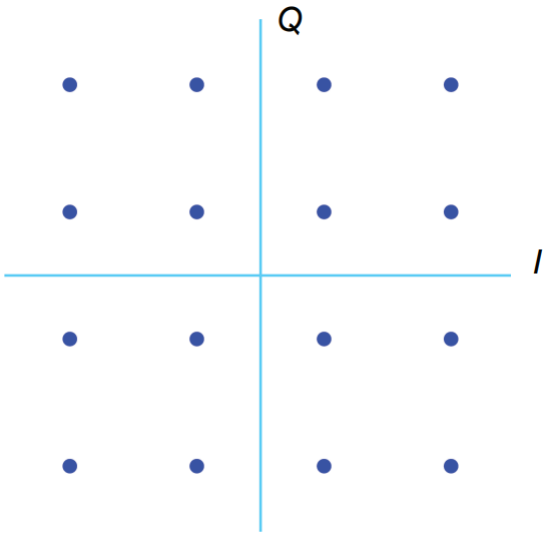

Figure 1.22: 16-QAM constellation diagram where each symbol represented as a point in the plane transmits 4 bits [47].

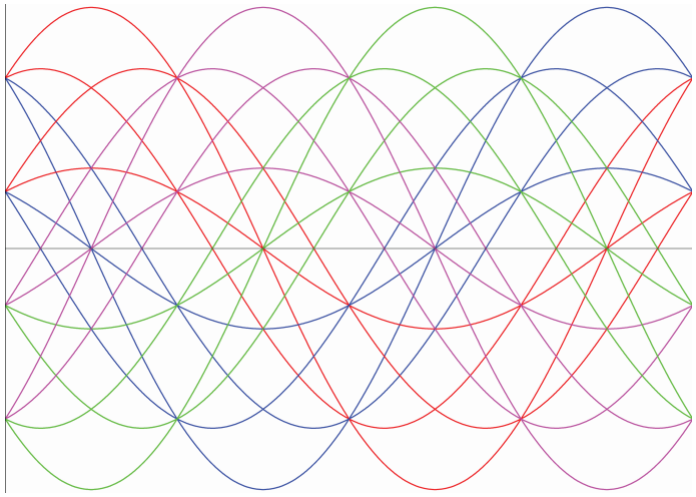

Figure 1.23: All QAM symbols for 16-QAM shown in the time domain [47]

remaining two symbols have the same magnitude which gives the third time domain amplitude and are distinguished by there phase. It can be seen from the time domain depiction that each symbol has the same frequency but a unique combination of phase and amplitude. The different colours show the different quadrants that the symbol is placed within in the complex plane. The number of separate symbols or, QAM order, required is determined by number of bits per as described by Eq.1.21.

$$QAMOrder = 2^{\frac{bits}{symbol}} \tag{1.21}$$

In section 1.6 the orbital angular momentum of light is introduced. The orthogonality of these modes underwater is investigated in Chapter 5. OAM multiplexing has been proposed as a means of multiplexing for VLC systems. This would be a form of space division multiplexing (SDM). SDM can be achieved through spatial separation of channels or through transmissions of different vector modes from an orthogonal basis set such as the Hermite Gaussian (HG) modes, with the intensity profiles shown in Fig.1.24, or Laugerre Gaussian (LG) modes discussed in section 1.6. Even though novel means of utilizing SDM in optical communications are emerging, it is actually a well established practice in electronics and both fibre and wireless optical communications. Spatial separation of channels is used in electronics with media interface technologies like HDMI and DVI and is also used in optical communications using fibre bundles. Wireless communication using WiFi uses multiple input multiple output (MIMO) technology which is another form of SDM. In the work in Chapter 5 SDM is investigated through the propagation of orthogonal OAM modes and examination of the crosstalk between these modes. Utilization of orthogonal modes is known as mode division multiplexing (MDM). Work has been done to investigate the application of MDM with few mode fibres (FMF). Fig.1.24 depicts one method of multiplexing and demultiplexing HG modes by manipulation of the fundamental mode using phase plates to give three orthogonal modes which can be coupled into a FMF. Further dis-

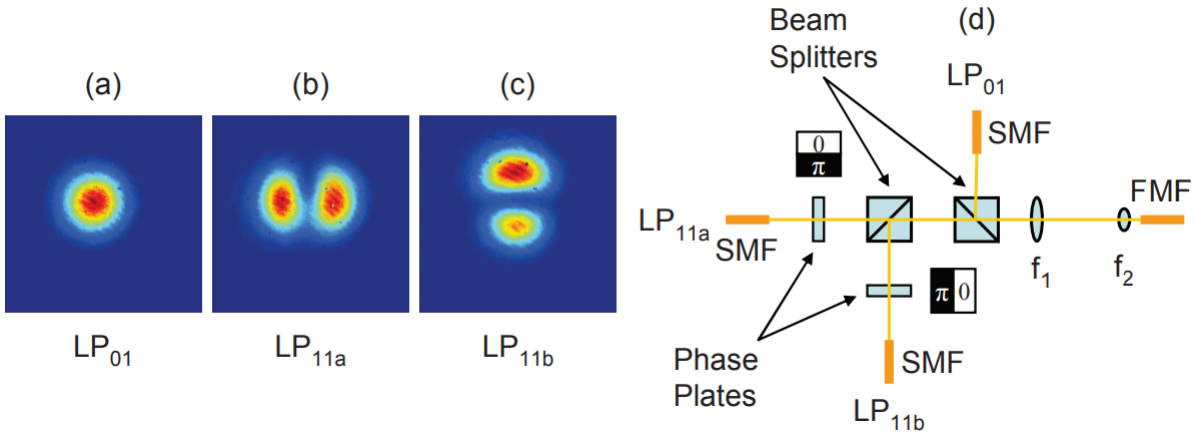

Figure 1.24: (a),(b),(c)Intensity profiles of three linearly polarized mode. (d) Free-space optics principle of the mode multiplexer/demultiplexer. [48].

cussion of generation, multiplexing and demultiplexing of OAM modes is described in section 5.2. The multiplexing scheme used to increase data rates in this thesis was OFDM. This will be discussed in the following section along with its predecessor frequency division multiplexing (FDM).

1.5.2 Orthogonal frequency division multiplexing theory and development

In order to understand why OFDM has become a popular multiplexing scheme it is first beneficial to observe its predecessor FDM. In a conventional FDM system there are multiple channels and each individual channel is centred at a different carrier frequency. The frequency range occupied by each channel is limited and inter carrier interference (ICI) is prevented by creating guard bands between the channels. The frequency domain representation of FDM is shown Fig.1.25.

The gaps between channels (guard bands) which prevent ICI mean there are ranges of the frequency spectrum which are not utilized to encode data. This is where the advantage of OFDM becomes obvious, by using carriers which are orthogonal it is possible to overlap the channels

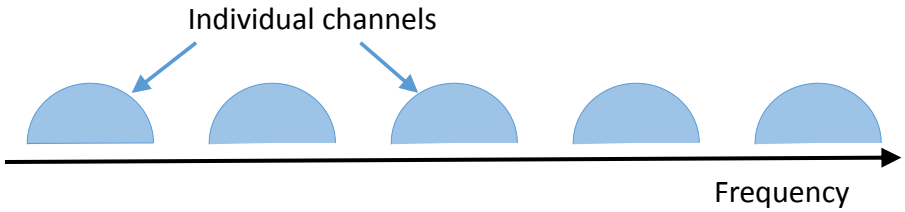

Figure 1.25: Carrier bandwidth and guard intervals for frequency division multiplexing.

and separate them after transmission. This is possible through digital signal processing using the fast Fourier transform (FFT) and inverse fast Fourier transform (IFFT) which will be explained further towards the end of this section. Fig.1.26 shows how this looks in the frequency domain and it can be seen from this that more of the spectrum is utilized which results in improved spectral efficiency when compared to FDM.

The idea of OFDM was first proposed in 1966 by Robert W. Chang [49]. Given a limited spectrum Chang suggested splitting the spectrum into individual sub-channels transmitted on orthogonal sub-carriers. This improved spectral efficiency and reduced receiver complexity due to frequency selective fading consistency across the sub-channels. However, this analogue domain implementation proved impractical as the number of sub-carriers increased. With this added complexity comes more stringent coherent detection and synchronization requirements which increases hardware costs, along with analogue oscillator drift causing ICI, this caused OFDM to have limited popularity at this time.

The next milestone for OFDM was the utilization of the discrete Fourier transform (DFT) and the reduction in system complexity this produced [50]. Using the DFT reduced hardware costs because the oscillators and coherent demodulators required in the analogue implementation became unnecessary. The orthogonality of the sub carriers was further improved in 1980 by Peled and Ruiz [51]. ISI and ICI interference were reduced by the introduction of the cyclic prefix. The cyclic prefix improved orthogonality compared to the work done by Weinstein and Ebert in [50], where guard time and raised cosine windowing where used to reduce ISI and ICI without the cyclic prefix.

Contemporary standards implementing OFDM use QAM encoding schemes. In 1980 Hirosaki demonstrated channel equalization for an OFDM QAM system [52]. One of the advantages of OFDM is simple channel equalization by multiplying the signal with a complex number to mitigate for the complex transfer function of the channel. Channel estimation through pilot tones, which is common in modern implementations of OFDM, was introduced in 1985 by Cimini [53]. Another major contribution made during the 1980s was the first use of adaptive bit loading [54]. Kalet showed that it was possible to reduce the frequency of errors in the transmit-

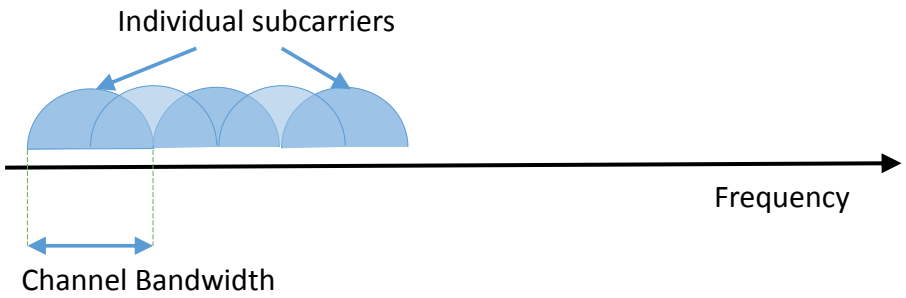

Figure 1.26: Carriers overlap in frequency space when using OFDM.

ted data by increasing the amount of data transmitted on reliable sub-carriers which experienced the least channel distortion. These contributions to OFDM, and others not noted here, meant that OFDM became more efficient and consequently in 1995 it was adopted as the European Digital Audio Broadcast (DAB) standard [55]. Today OFDM is utilized in many data transmission standards, most notably, IEEE 8012.11a/g standards for wireless local area networks (WLAN), ITU G.992.1 asymmetric digital subscriber line (ASDL) standards and the long-term evolution (LTE).

The fundamental requirement for using OFDM for multiplexing is the orthogonality of the sub-carriers. Two functions can be described as being orthogonal if their inner product, shown in Eq.1.22, is equal to zero.

$$\langle f,g\rangle = \frac{1}{L}\int_{-L}^{L} f(x)g(x)dx \tag{1.22}$$

When $\langle f,g\rangle = 0$ the carriers f & g are orthogonal and different data sets can therefore be transmitted on each carrier. Theoretically infinite sinusoids would only have one non-zero component in the frequency domain which would then mean each sinusoid could modulate different data and be filtered to separate them from one another. However, due to pulse shaping in the time domain the spectrum of the carrier broadens and this creates a requirement on carrier spacing to maintain orthogonality. The frequency spacing between the carriers must be $\frac{1}{T_s}$ where T_s is the symbol duration. This is achieved in OFDM by using the inverse discrete Fourier Transform (IDFT) with specified carrier frequencies given in Eq.1.23

$$f[n] = \frac{1}{N}\sum_{k}^{N-1} F[k]e^{j\frac{2\pi kn}{N}} \tag{1.23}$$

The binary information is converted from serial to parallel before being used to modulate individual carriers using QAM. The IDFT generates the transmitted time domain sample n from the frequency domain coefficients F[k]. N samples are then converted from parallel into the series time domain signal. The block diagram at the bottom of Fig.1.27 shows this process.

After the time domain signal has been generated a cyclic prefix is added to the signal. The cyclic prefix takes a given number of samples from the end of the time domain data stream and repeats these at the beginning of the stream. This is shown in the block diagrams in Fig.1.27. Ng samples are taken from the end of the time domain symbol, which is N samples long where N is the number of points in the IFFT, and attached to the front of the symbol. This is achieved through taking the final Ng output samples from the IFFT and attaching these to the front of the symbol as depicted in Fig.1.27. This block diagram also shows the conversion of the parallel frequency coefficients to the serial time domain stream. The cyclic prefix acts as a guard interval reducing inter-symbol interference (ISI) in multipath propagation channels. Delayed signals from multipath propagation can cause the overlap of symbols which means orthogonality between carriers no longer exists. Fig.1.28 depicts the cyclic prefix (Green Block) acting

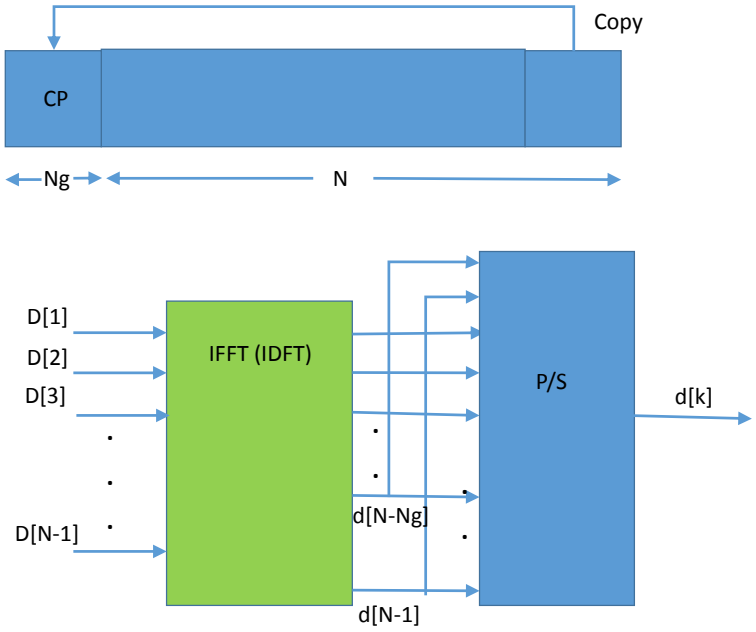

Figure 1.27: Cyclic prefix is taken from the end of the symbol and attached at the beginning to reduce ISI.

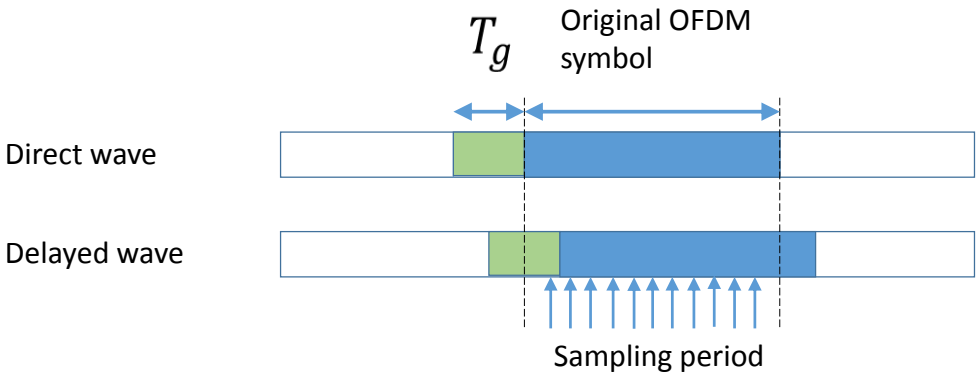

Figure 1.28: Cyclic prefix is taken from the end of the symbol and attached at the beginning to reduce ISI.

as a guard interval. The cyclic prefix must maintain an integer multiple cycles within the DFT interval in order to prevent ICI in the frequency domain that is why a cyclic prefic guard interval is required instead of other forms of guard interval.

1.6 Orbital angular momentum

Since James Clark Maxwell published his paper "A Dynamical Theory of the Electromagnetic Field", in 1865, it has been accepted that light intrinsically carries momentum in addition to

its energy [56]. Later, the form of this momentum was investigated by Poynting [57]. Poynting made an analogy between the mechanical model of a revolving shaft and the rotation of a circularly polarized electromagnetic field. He suggested that looking at the torque and energy relation of a beam of light incident on an absorbing surface would yield the same relationship of torque and energy for a uniformly revolving shaft. However, this wasn't demonstrated experimentally until the 1930s, when Beth reported the conservation of angular momentum exhibited when a double refracting plate reversed the polarisation of a circularly polarised light beam and experienced torque as a result [58].

Moving on from the classical wave theory of light to the modern quantum interpretation, the circularly polarised light concerned in the previously discussed work can be thought of as spinning photons. In the case of a single photon the spin angular momentum (SAM) can take one of two values, SAM can equal $\pm\hbar$. However, looking at the production of photons, it can be seen for higher order atomic transitions that the momentum transfer is greater than $\hbar$. It was Darwin in 1932, who first suggested that a torque was produced when linear momentum acted at a radius vector, and this could produce the extra angular momentum [59]. This is known as orbital angular momentum of light and it is the angular momentum associated with the spatial field distribution of light and not the photon spin or polarization of the photons.

In 1992 Allen *et al.* demonstrated that the OAM identified by Darwin was not as a result of a rare almost forbidden transition [60]. They showed it was possible to generate laser light beams where every photon was in a higher angular momentum state. When a cylindrical lens is placed in a Hermite-Gaussian beam it converts the beam to a Laguerre-Gaussian beam with a helical phase front and OAM demonstrated in Fig.1.29. The Laguerre-Gaussian beam shows the transverse electric and magnetic field in the plane of the helical phase front which means the orthogonal Poynting vector will point in different directions dependent on the position within the phase front. Therefore, the linear momentum of the light has an azimuthal component. This means the light carries an angular momentum in the direction of propagation of the light independent of the spin of the photon.

The angular momentum of a photon is described by $\sigma\hbar$ where $\sigma = \pm 1$. This describes the left or right polarisation of the photon. As a result of this, there are only two orthogonal states for the angular momentum of photon spin. Whereas, OAM has an unbounded state space. Below is Eq.1.24 which describes the Laguerre-Gaussian beam.

$$\psi_{l,p}(r,\theta) = C_{lp}\left(\frac{\sqrt{2}r}{w}\right)^{\frac{|l|}{2}} \; L_p^{|l|}\left(\frac{2r^2}{w^2}\right) \; x \; exp[\frac{-r^2}{w^2}]exp[il\phi] \tag{1.24}$$

The $exp[il\phi]$ term determines the azimuthal phase profile of the helical beam. This helical phase profile gives rise to a skew angle in the local rays and this is described by Eq.1.25.

$$\beta = \frac{l\lambda}{2\pi r} = \frac{l}{kr} \tag{1.25}$$

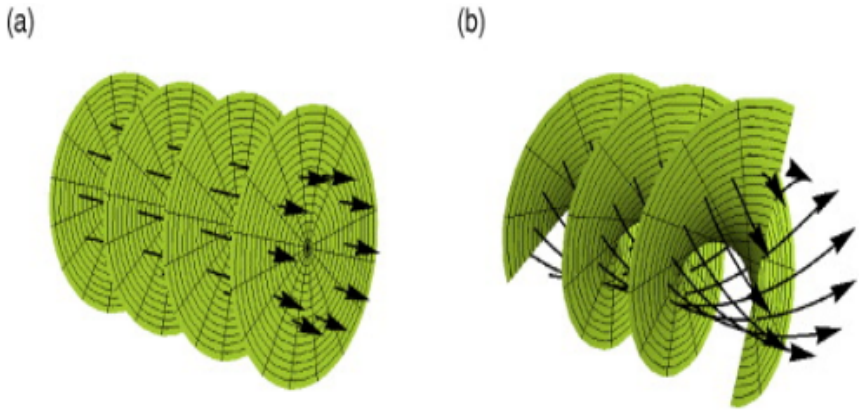

Figure 1.29: (a)Plane wave with Poynting vector parallel and collinear to propagation. (b) Laguerre-Gaussian beam where the Poynting vector has an azimuthal component [61].

Where the distance from the beam centre is r, λ is the light wavelength and k is the wavenumber of the beam. Furthermore, the OAM can be determined by considering the linear momentum P of a skewed ray incident on the surface at an angle of β from Eq.1.26.

$$|L| = |rxP| = |rx\hbar ksin\beta| = l\hbar \tag{1.26}$$

Therefore, the OAM state space is unlimited, given an infinite aperture, as there is no limitation on the value of l. This has caused interest in the use of OAM in communications as the theoretically unbounded state space could yield high data density communications.

The multiple orthogonal states available when using OAM multiplexing and the inherent loss of orthogonality for off axis interpretation has caused interest in the use of OAM as a multiplexing technique in communications.

1.7 Summary

This chapter gives a basic theoretical introduction and historical development of the two types of sources measured and utilized in the experimental work detailed in this thesis.

Similarly, a historical introduction and theoretical explanation are presented for the two multiplexing schemes applied to the sources during the experimental work described in the following chapters. The work throughout this thesis will based on a combination of either lasers or LEDs with OFDM or OAM.

More specific descriptions of the sources will be given at the beginning of the relevant chapters along with a literature review specific to the research described in that chapter. Chapter 2 gives the results from research of the communication capabilities of a unique micro-LED design therefore, appropriately, the specific design of that device will be discussed in that chapter. Where OFDM is utilized in chapters two and three more specific parameters relating to the application of OFDM will be discussed. This chapter serves an introduction and broad overview

to the sources and multiplexing schemes used for the research results given in this thesis.

Chapter 2

GaN based array μ-LEDs for OFDM communications

This chapter discusses the results from the demonstration of two VLC systems using InGaN μ-LEDs at 400 nm (violet) and 450 nm (blue). Firstly, an overview of past research using LEDs for VLC is presented. Then the design and fabrication process for the μ-LED array is described. This design and process is similar for both the violet and the blue light systems. The difference being the InGaN composition which is varied to create different emission spectra. After the system source has been described the OFDM implementation, system design and experimental method are explained. The final section of this chapter presents the results and discussions for both of the μ-LED systems.

2.1 Visible light communication utilizing LEDs

The use of LEDs for optical communications has been evident for many decades. Applications exist in both free space and fibre systems. An everyday example of this is the use of IR-emitting LEDs in remote controls and automated card readers. The first IR LED suitable for coupling into silica fibre for communications was demonstrated in 1971 [62]. This was demonstrated by Burrus and Miller using a GaAs IR LED. Due to their low cost IR LEDs are widely used in short distance and low to medium data rate applications. IR-emitting RCLEDs have been demonstrated as a source for an indoor communication system transmitting at 155 $Mbit/s$ and tracking a mobile receiver's position [63].

LEDs have also been used to transmit information in the visible light range of the electromagnetic spectrum. VLC using red emitting LEDs in combination with POF are frequently used for short distance transmission. At the emission frequency of red LEDs (650 nm) POF fibre has low loss and low dispersion [16]. Dumitrescu *et al.* used a red emitting RCLED with a bandwidth of 350 MHz to transmit via a POF at 622 $Mbit/s$ error free [64]. Similarly to lasers, Resonant cavity LEDs (RCLEDs) place the light emitting region of the device in an optical

cavity. The length of the cavity is set so that the emission wavelength of device is a resonant frequency of the cavity. The concept of resonance was explained in section 1.4.3. The mirrors at either end of the cavity reflect photons back into the region causing stimulated emission. The light is coupled out via the mirror with lower reflectivity. The QW is located at the antinode of the standing wave in the cavity. Unlike lasers the rate of stimulated emission does not surpass that of spontaneous emission and absorption within a RCLED. RCLEDs have a number of advantages over conventional LEDs: The light intensity normal to the direction of the device is enhanced due to the increased directionality of the light output from RCLEDs, As a result of the optical cavity in a RCLED the light output has higher spectral purity and the device also has higher extraction efficiency than conventional LEDs.

An alternative to red emitting LEDs are AlInGaN-based LEDs. Emitting at 510 nm, in the green portion of the visible spectrum, the wavelength of these devices approximately coincides with the attenuation minimum in POF [65]. However, there can be difficulties with the manufacturing of AlInGaN-based RCLEDs [66]. High Q cavities are attainable in RCLEDs with the use of epitaxial and dielectric DBRs acting as mirrors. The difficulty in growing in epitaxial DBRs in $III-V$ materials means that RCLEDs in these materials are still in the early developmental stage. The alternative options for bounding the optical cavity require expensive lift off processes. Shaw *et al.* modelled nitrde based RCLEDs for optical fibre communications by varying the AlN proportion in the AlGaN layers. The limitation of such devices would be the small refractive index that is achievable between between adjacent DBR layers and growing more layers to increase reflectivity results in severe strain management issues. *III*-Nitride RCLEDs that have been used in fibre optical communications have been fabricated without epitaxial DBR growth. VLC using a *III*-Nitride RCLED was demonstrated using at 509 nm over 100 m of fibre. Using a blue RCLED Tsai *et al.* achieved 100 $Mbit/s$ over 100 cm of free space.

LEDs can also be used for free space transmission. The idea of dual purpose lighting, where LEDs are used to communicate and illuminate simultaneously, was proposed in 2004 [67]. This concept is of interest as it would be an energy efficient alternative to current practice. Additionally, there are environments where optical systems are more desirable than RF systems such as hospitals where RF frequencies can interfere with equipment. Therefore, there is a growing field of research examining visible light for free space communication. Currently commercially available white light LEDs have been shown to be capable of data transmission up to 500 $Mbit/s$ [68]. There are several factors limiting the use of commercially available devices with one of the main issues being the carrier lifetime in these devices which affects the bandwidth.

μ-LEDS are emerging as a good candidate for both free space and fibre communications sources. μ-LEDS have a number of advantages over broad area devices. These LEDs have been shown to have turn-on times in the region 30 ps and turn-off times of around 0.2 ns. These fast switching times can be attributed to the small device area and high current density of these LEDs [69]. μ-LEDS are easier to manufacture than RCLEDs and also have the advantage

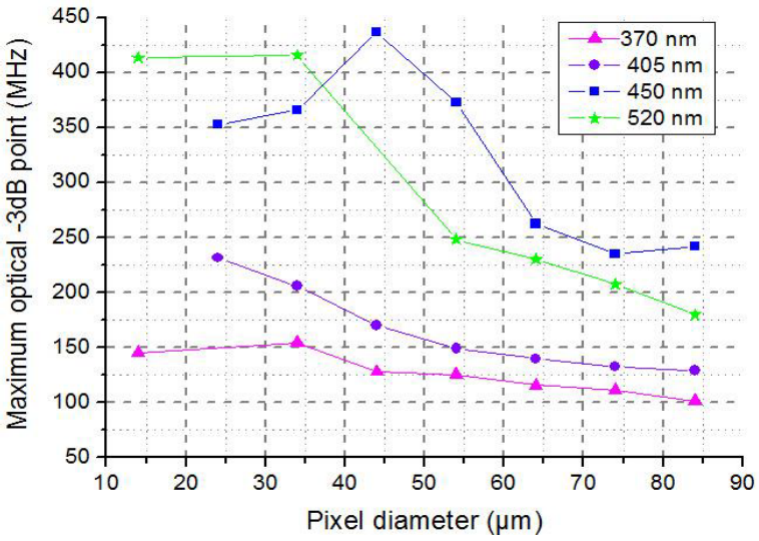

Figure 2.1: Maximum modulation bandwidths of micro-LED pixels of different diameters and peak emission wavelengths [70].

of having several sources on one chip that can be modulated independently. Furthermore, array design of μ-LEDs can be useful when coupling into arrays of fibre for parallel data transmission.

μ-LEDS have smaller active areas than conventional LEDs. This is desirable as bandwidth has been shown to be inversely proportional to area. McKendry demonstrated this when he characterised an 8 x 8 array of GaN μ-LEDs with various areas [70]. In his paper, the μ-LEDs in the array had wavelengths of 370, 405, 450 or 520 nm. The inverse relationship can be seen in Fig.2.1. Deviations from the inversely proportional relationship between area and bandwidth are attributed to defects by McKendry. These defects limit the drive current of the 24 and 34 μm device and, therefore, the bandwidth. The highest modulation bandwidths measured were greater than 400 MHz and a data rate of 512 $Mbit/s$ was achieved modulating a 24 μm pixel with an emission wavelength of 450 nm. The formula for calculating the bandwidth of an LED is shown in Eq.2.1.

$$f_{3dB} = \frac{1}{2\pi\tau} \tag{2.1}$$

τ can be the value of the RC time constant or the carrier lifetime. When the resistance and capacitance are high enough the time it takes for the voltage across the LED to change is determined by the RC time constant.

This then limits the rate at which the optical intensity can be varied and therefore affects the bandwidth. The voltage as a function of time across the LED is shown in Eq.2.2.

$$V(t) = V_B(1 - e^{\frac{-t}{RC}}) \tag{2.2}$$

Where V is the voltage across the device, V_B is the bias voltage, t is time, R and C are the resistance and capacitance of the device.

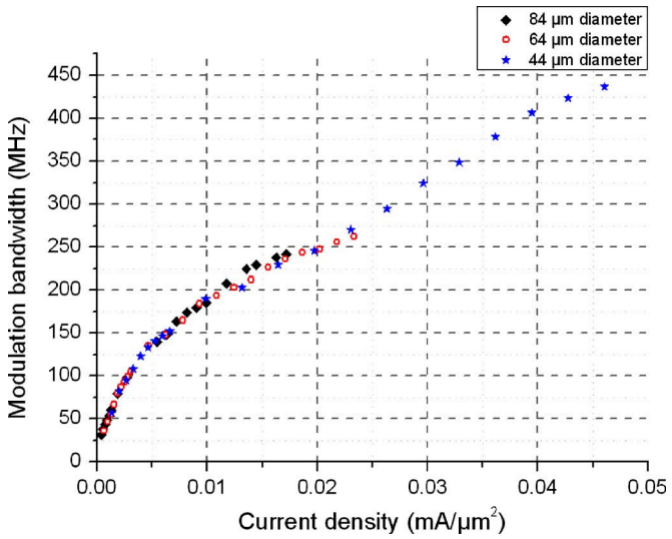

Figure 2.2: Bandwidth versus current density for different pixel sizes from the same 450 nm-emitting 8x8 μ-LED array. [70].

Another finding from this work by McKendry *et al.* is the relationship between current density, modulation bandwidth and the μ-LED active area. Fig.2.2 shows modulation bandwidth plotted against current density for three pixels with different active areas. The figure shows the modulation is dependent upon current density. The bandwidth is similar for each of the different size pixels at the same current density. This shows that the limiting factor in the bandwidth of these devices was the carrier lifetime and not the RC time constant associated with the devices. If the capacitance was affecting these devices the bandwidth of the bigger devices would be less than that of the smaller devices for a given current density. Additionally, the bandwidth would not continually increase with the current density as the RC time constant would cause the bandwidth to saturate.

However, part of the significance of this work is that the LEDs were integrated with a CMOS driver array chip. The system bandwidth, including the driver, was reduced to 185 MHz. Therefore, this lower overall bandwidth was what limited the data rate and not solely the bandwidth of the μ-LED. The integration of the μ-LED and CMOS driver signifies progress towards convenient computer control of the μ-LEDs. In this instance, error free data is defined as a BER of less than 1 x 10^{-10} and 512 $Mbit/s$ was achieved using NRZ OOK. μ-LEDs offer an increased current density and therefore bandwidth compared to conventional LEDs resulting in higher data rates.

Looking at more complex modulation techniques, Tsonev *et al.* showed it is possible to achieve data rates of up to 3 $Gbit/s$ using a single 50 μm GaN LED if OFDM is used [71]. OFDM modulation is an attractive proposition when using LEDs as it allows the limited bandwidth of the transmitter to be utilized to its full capacity. In Tsonev's paper there are two approaches to the use of OFDM. In the first approach pre-equalization is achieved by applying the inverse of the frequency response function to the signal before transmission. The signal arrives

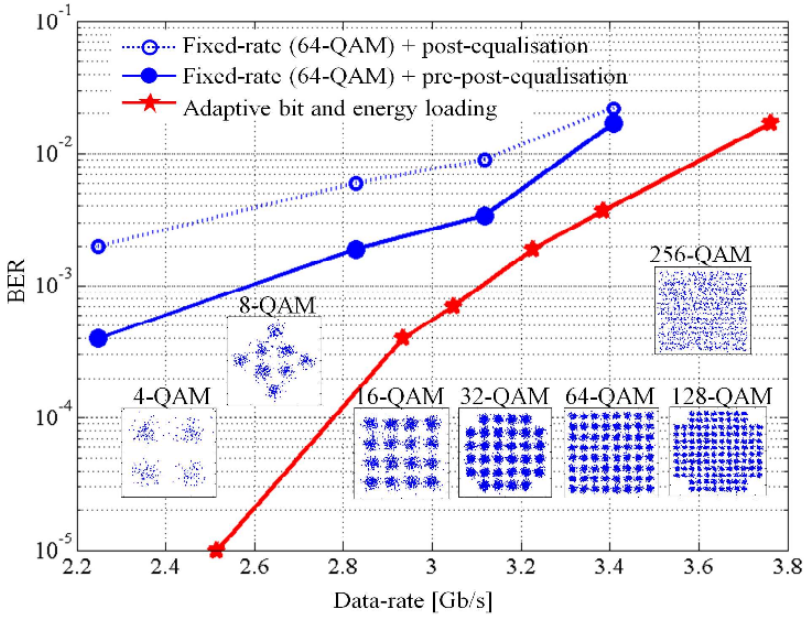

Figure 2.3: BER results and received constellations for D=3.22 $Gbit/s$ with adaptive bit and energy loading [71].

with the same average energy on each subcarrier as the gain due to transmission has been compensated for with pre-equalization. Using this method the optimum constellations size for the QAM signal on each subcarrier was M=64 which achieved 2.8 $Gbit/s$ with a BER < 0.002. The second method is to use adaptive bit and energy loading on each subcarrier. The algorithm used to ascertain the loading on each carrier is the Levin-Campello algorithm on optimal data allocation [72]. Using this optimized system for loading then allows for higher data transmission at the same BER. Allowing for a FEC code with an overhead of 7% Tsonev was able to demonstrate a 3 $Gbit/s$ wireless VLC link over 5 cm of free space. This distance could be improved with the use of multiple LEDs which would generate greater signal power. Fig.2.3 demonstrates these results. Utilizing μ-LEDs with complex modulation formats and multiplexing techniques results in $Gbit/s$ data rates.

When using blue LEDs at 450 nm it is necessary to pass the blue light through a yellow emitting phosphor if white light is required. There is a relaxation time associated with such filters which affects the system bandwidth, this was shown to be 73 ns for the phosphor in [73]. These devices are discussed further in section 2.4.2. When considering sources for dual purpose lighting RGB LEDs provide a feasible alternative to nitride based LEDs with phosphor caps. With the advantages of avoiding bandwidth effects from phosphors and creating the option of implementing WDM to increase data rates. Wang utilized WDM to produce a VLC system capable of 4.5 $Gbit/s$ over a distance of 1.5 m [74]. This is a significantly greater distance than other published work with comparable data rates (where the transmission distances range from 1 cm to 25 cm) [75–77]. A BER of $3.8x10^{-3}$ is achieved at 400 lx which is below the standard illumination level of 500 lx. Hence, the system could be improved by increasing the optical

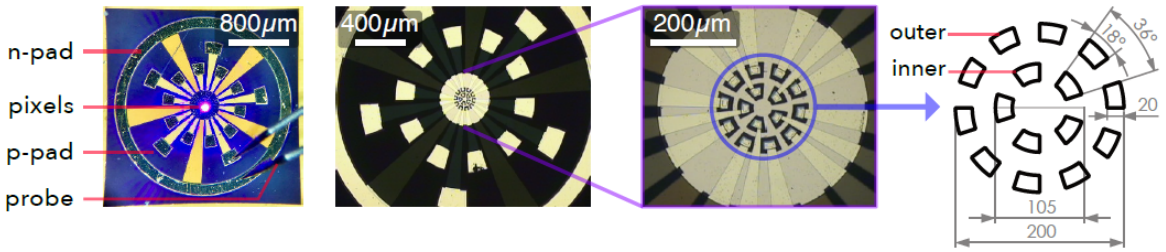

Figure 2.4: Micrographs of the segmented μ-LED arrays. Magnified micrographs on the right show the array configuration and individual pixel design, a diagram is also included noting inner and outer pixels (dimensions in micron).

power. The luminance level is what limits the distance to 1.5 m at 4.5 Gbit/s

As will be shown in the next chapter lasers are also commonly used as transmitters in VLC research. There are various advantages and disadvantages to VLC systems using GaN based μ-LEDs, RCLEDs and lasers. Lasers have higher output power, bandwidth, efficiency and light directionality than LEDs, however, they are more expensive. Therefore, lasers may find there application in more niche markets such as underwater communications, this is discussed further in the following chapter. GaN based RCLEDs are still currently under development but could find use in POF systems defined by the IEEE 1394b S200 where red RCLEDs are currently being used. μ-LEDs have lower output power and data rates than lasers but are less costly so could find use in more general VLC scenarios such as "Li-Fi" in office or home settings.

The work in this chapter has been carried out using 400 nm and 450 nm μ-LEDs. With these devices both out performing previous devices at these wavelengths [70, 78]. There is more on why these devices are of particular interest in section 2.4.1 and section 2.4.2 where the results from each system are reported. The following section describes the design and fabrication of these μ-LEDs.

2.2 μ-LED design and fabrication

The novel devices used as the transmitter in the following VLC systems were designed and fabricated by the Institute of Photonics at the University of Strathclyde. All the experimental work described in this thesis was carried out at the University of Glasgow.

The μ-LED used in this work as the source at the transmitter is selected from a μ-LED array. The array consists of two segmented rings of μ-LED. The outer ring contains 10 LEDs whilst the inner ring has 5 LEDs. The active are of the outer ring LEDs is 465 μm^2. The inner LEDs have a smaller active area of 435 μm^2. This array design was initially used to match with the design of POF. The design can be seen in Fig.2.4.

The μ-LED arrays shown are fabricated from AlInGaN wafers hetero-epitaxially grown on c-plane sapphire substrate (Al_2O_3). Sapphire is an appropriate choice as a substrate as it has a

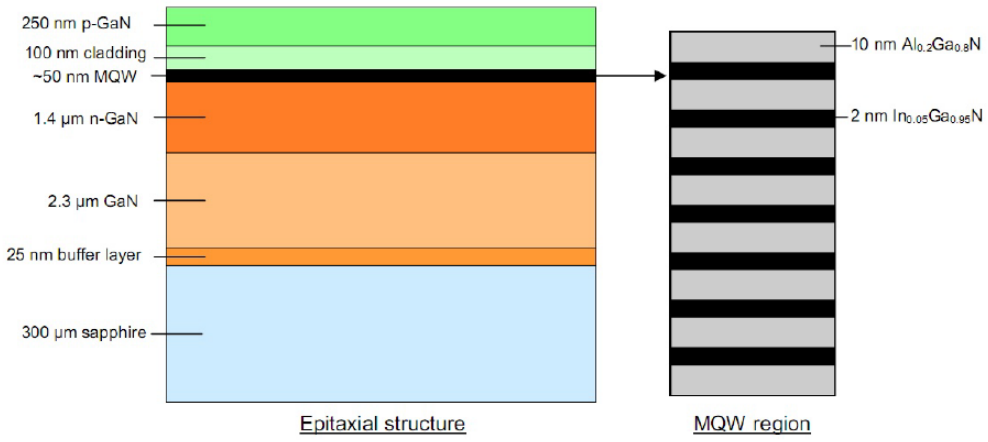

Figure 2.5: Schematic illustration of a typical epitaxial structure of a UV-emitting micro-LED. The MQW region is expanded and is shown on the right. Schematic is not to scale [79].

close lattice match with AlInGaN. Additionally, across optical frequency sapphire is transparent which is obviously beneficial for VLC sources. There are other substrate materials more suited to AlInGaN wafer growth, however, they are not as commonly available or as low cost as sapphire.

Fig.2.5 shows a typical epitaxial structure for InGaN-based LEDs. The first layer is a 300 μm sapphire substrate upon which is grown a 25 nm GaN buffer layer to help compensate for the differences in lattice structure between the substrate and the AlInGaN wafer. On top of the buffer layer a 2.3 μm layer of undoped GaN is grown followed by 1.4 μm layer of Si-doped n-type GaN. This layer is capped by the MQW region which is 50 nm thick. On top of the MQW region is a cladding layer of M_g-doped AlGaN which preserves the carrier density in the active region by providing a potential barrier. The barrier prevents electrons from overflowing and escaping the MQW region. The uppermost layer of the structure is a contact layer of 30 nm thick M_g-doped GaN. The MQW region is bounded either side by a layer of 10 nm thick $Al_{0.2}Ga_{0.8}N$. Between the barrier layers there are seven 2 nm thick $In_{0.05}Ga_{0.95}N$ QWs. After the wafer is grown it must be processed to produce an operable LED. Fig.2.6 shows two common configurations for LEDs. Fig.2.6.a) shows the conventional chip configuration. A small area of the p-type layer must be etched to allow access to the n-type layer. Ohmic contacts can then be deposited in each of the regions. When LEDs operate in this configuration the light is mostly extracted by passing through the p-type material and the p-type current spreading layers which reduces the efficiency and power output of the LED. An additional disadvantage of conventional chip orientation is the dependence on sapphire which has poor thermal conductivity and this inefficient heat extraction further reduces the performance of the device.

The μ-LEDs used for the experimental work in this thesis are orientated in the flip chip configuration shown in Fig.2.6.b). The etching process is similar to that in the conventional chip, however, in this case the device is flipped and the contacts are soldered directly to another

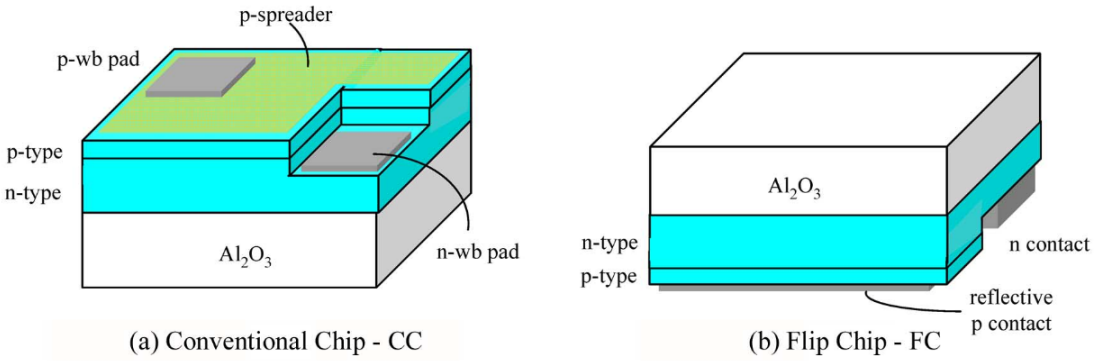

Figure 2.6: Two common structures of AlInGaN LED die - the μ-LEDs used in this thesis are based on the (b) flip-chip designs [80].

substrate, which is normally silicon. This removes the need for wire bonding which improves light extraction efficiency. With the LED mounted directly onto a new substrate with better thermal conductivity than sapphire, the flip chip configuration is capable of higher output power and better efficiency than the same device in conventional chip orientation. After the device is etched metal contacts are deposited on the n and p type regions using magnetron sputtering or electron-beam evaporation. Titanium/gold was used for the n-contacts and palladium was used for the p-contacts.

This chapter reports the results from the use of two different wavelength LEDs both fabricated from AlInGaN wafers, these being 400 nm and 450 nm. It is possible to produce LEDs from AlInGaN wafer with wavelengths varying from deep-UV to near infrared. This is possible by changing the proportion of each of the elements in the quaternary alloy which changes the bandgap and emission wavelength. The next section moves from the device level to the system level by explaining the OFDM implementation and the transmitter and receiver design.

2.3 μ-LED communication system

This section gives a description of the OFDM implementation used to modulate the violet and blue μ-LEDs. It also describes the system design and the experimental method used to take the measurements and give the results which are described in the final section of this chapter.

2.3.1 OFDM implementation

When using OFDM for VLC the signal must be purely real to utilize intensity modulation direct detection. To achieve this Hermitian symmetry must be achieved by imposing zero values on the DC subcarrier and the 2π subcarrier and setting the negative frequency carriers to the complex conjugate of the positive frequencies [71]. The bandwidth of a system utilizing OFDM is limited to twice the Nyquist rate therefore N_{fft} subcarriers are evenly separated across the frequency

range $-\frac{1}{2T_s}$ to $\frac{1}{2T_s}$ where T_s is the time domain sampling period which corresponds to the Nyquist rate. The spectral efficiency of OFDM is described by Equation 2.3.

$$n = \frac{\sum_{k=0 M_k>0}^{\frac{N_{fft}}{2}-1} log_2 M_k}{N_{fft} + Ncp(1+\beta)} \ \ bits/s/Hz \tag{2.3}$$

Where N_{fft} is the number of subcarriers, M_k is the order of QAM on the K_{th} carrier, N_{cp} the length of the cyclic prefix in the time domain and β is roll off factor for the employed RRC filter. The single sided bandwidth is given by Equation 2.4.

$$B = \frac{1}{2T_s}(1+\beta) \ \ Hz \tag{2.4}$$

Using the spectral efficiency and bandwidth it is possible to calculate the data rate with Equation 2.5 .

$$D = 2Bn \ \ bits/s \tag{2.5}$$

The number of points in the FFT (N_{fft}) is equal to 1024 in this experiment. After exhaustive experimental measurements the cyclic prefix length (N_{cp}) was set to 5 which prevented any significant intersymbol interference (ISI). These settings for clipping and carrier number come from the Matlab OFDM provided by the University of Edinburgh. The values are found by adjustment of parameters and observation of system BER. It is possible to use a bipolar OFDM signal to modulate a laser diode if a suitable DC bias is selected around which the signal will be centred. This is known as DC-biased optical OFDM (DCO-OFDM). The time domain OFDM signal typically has high peak to average power ratio (PAPR) and to avoid this clipping of the time domain waveform can be employed. If the PAPR is high, the peak value is mapped to the maximum output of DAC and all the other values relative to the peak are much lower and therefore will be mapped to much lower outputs on the DAC which will mean a low system SNR. By clipping the peak and reducing the PAPR it will mean samples other than the peak sample will be mapped to higher outputs of the DAC whilst maintaining the peak sample as the max output of the DAC increasing the system SNR. In this experiment the upper and lower clipping was set as +3σ and -3.5σ respectively. Where σ is the standard deviation of the time domain signal. Equation 2.6 shows the square of σ known as the variance.

$$\sigma^2 = 2 \sum_{k=0}^{\frac{N_{fft}}{2}-1} \frac{E_{bk} log_2 M_k}{N_{fft}} \tag{2.6}$$

Where E_{bk} is defined as the energy per bit on the k_{th} subcarrier.

The components of the transmitter and receiver are shown in the block diagram of Fig.2.7. The SNR from the a priori estimation is used to determine the bit and power allocation to each

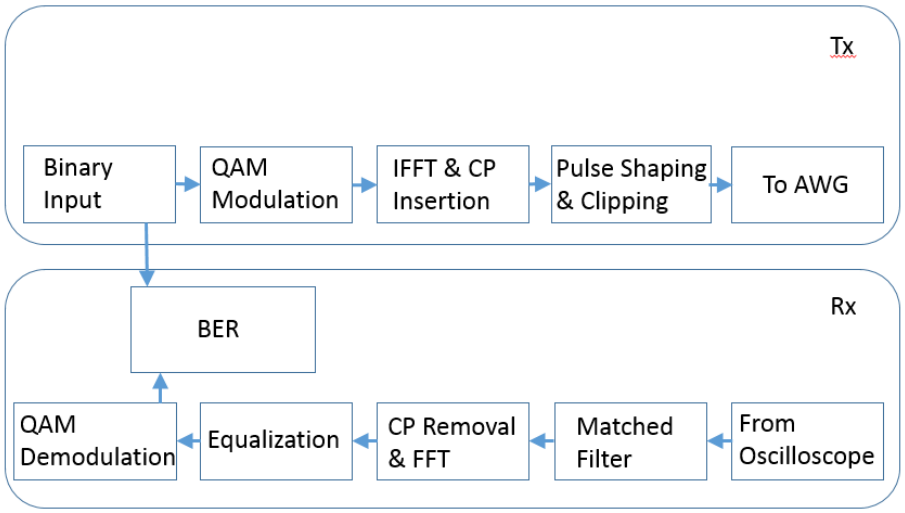

Figure 2.7: Block diagram showing OFDM transmitter and receiver components.

carrier. The binary data is encoded using QAM format before the IFFT converts the signal to the serial time domain waveform. The addition of the cyclic prefix helps the receiver determine the starting position of the OFDM block, finally pulse shaping and clipping reduce ISI and PAPR respectively. The receiver then filters and removes the CP from the time domain waveform before the FFT converts back to the frequency domain. Compensation of the effect from the channel is performed by equalization before QAM demodulation. The BER can then be calculated by correlation of the known binary data with the received data.

The SNR of the subcarriers is used to adaptively load the carriers with customized bit and energy loading determined by the Levin-Campello algorithm [72]. The a priori estimated SNR is achieved using the channel estimation described by Wang *et al.* This is done by assuming the signal at the receiver takes the form of Eq.2.7.

$$S_r = H(f)S_t(f) + N(f) \tag{2.7}$$

Where $H(f)$ is the complex channel gain as a function of frequency, $S_t(f)$ is the frequency component of the transmitted symbol and $N(f)$ is the AWGN frequency components. $H(f)$ is assumed to respresent the electrical and optical channel. To estimate the channel, noise and SNR mutliple copies of a known OFDM pilot frame are transmitted sequentially. As the AWGN is zero mean, when N copies of the known frame are received the channel can be estimated with a conventional mean estimator as described in Eq.2.8.

$$\hat{H}(f) = \frac{\sum_{i=1}^{N} S_r^i(f)}{NS_t(f)} \tag{2.8}$$

With an estimated channel the the noise variance can be estimated with a conventional variance estimator given in Eq.2.9.

$$\hat{\sigma}_n^2(f) = \frac{\sum_{i=1}^{N} |S_r^i(f) - \hat{H}(f)S_t(f)|^2}{N-1} \tag{2.9}$$

From the channel gain and the noise variance, the achieved channel SNR can be estimated. After the SNR has been estimated it is then used to adaptively load the carriers with different energy and bit allocation using the Levin-Campello algorithm. The pseudo code for the initial bit allocation is shown in Fig.2.8 where the minimum channel loading is 2 bits which is in line with the asymmetric digital subscriber line requirements.

The index to each subchannel is determined by i. The projected margin (PMi) is the difference between the subchannel's SNR (SNRi) and the required SNR (SNRref(b)) for a given number of bits (b). The algorithm works by finding the subchannel with the maximum projected margin and attributing k bits to this channel. In this case the number of used subchannels (U) effects the total number of bits that require allocation (Bt) because of the use of trellis coding. Therefore, the number of used channels is monitored. After attributing bits to the subchannel with the maximum projected margin the projected margin for this subchannel is updated before the cycle repeats until all the bits have been allocated.

After this initial allocation, energy is adaptively loaded by increasing the energy loading on subchannels which are close to having the required SNR for higher QAM constellations. The target BER must be preserved after changing the constellation. This adaptive bit and energy loading is therefore the optimization of the spectral efficiency subject to the target BER and power limitations. Fig.2.9 shows the bit and energy loading of subcarriers which is determined by the Levin-Campello algorithm [72]. The channel capacity is also shown as described by Shannon [81]. The implementation of this was achieved through MATLAB provided by the University of Edinburgh

```
FOR i = 1:N, PM_i = SNR_i - SNR_ref(2)
WHILE B_t > 0
        max = index{maximum(PM_i)}
        k=1
        IF b_max = 0
                IF U is even
                        B_t = B_t + 1
                END
                k= k + 1
                U= U +1
        END
        b_max = b_max + k
        B_t = B_t - k
        PM_max = SNR_max - SNR_ref(b_max+1)
END
```

Figure 2.8: Pseudo code for initial bit allocation from Levin-Campello algorithm [72].

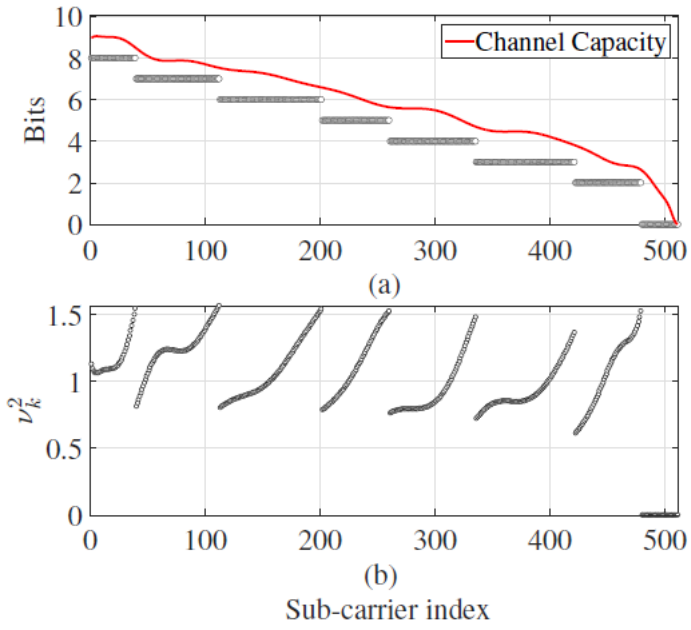

Figure 2.9: (a) The bit loading and channel capacity per subcarrier, both given in bits per subcarrier. (b) Energy loading per subcarrier.

2.3.2 System design and experimental method

The optical power of the arrays under DC conditions was measured using a Si detector placed at close proximity to the polished sapphire substrate. A spectrometer and charge coupled device detection system was used for the collection of electroluminescence spectra.

The small signal frequency response was measured by a network analyser (NA) (HP8753ES). The system design block diagram is shown in Fig.2.10. A 224 mV AC signal is output from the NA sweeping across a frequency range from 100 KHz to 1 GHz. This is combined at the bias-T (ZFBT-4R2GW+) with a DC signal biasing the laser diode. The frequency response measurement was performed at varying drive currents. The output from the bias-T was connected to a high speed probe which was connected to a μ-LED.

The light emitted from μ-LED is collected and collimated with an optical plano-convex lens from Thorlabs (LA1116). The light is reflected by a dielectric mirror from Thorlabs (CM1-E02) with higher than 97% reflectance at the transmission wavelength. The reflected light is then focussed using a bi-convex lens from Thorlabs (LB4879) followed by a microscopic objective lens Newport (M-40x) with a numerical aperture of 0.65. The light is focussed onto a silicon positive-intrinsic-negative (PIN) Femto photoreceiver (HSPR-X-I-1G4-SI) with a 3 dB bandwidth of 1.4 GHz and a responsivity of 0.135 A/W around 400 nm and 0.185 A/W at 450 nm. The experimental setup is shown Fig.2.11. The signal from the photoreceiver was then connected back into the NA and the NA measured the frequency response of the system.

The system was then updated to perform OFDM data transmission. The updated system is

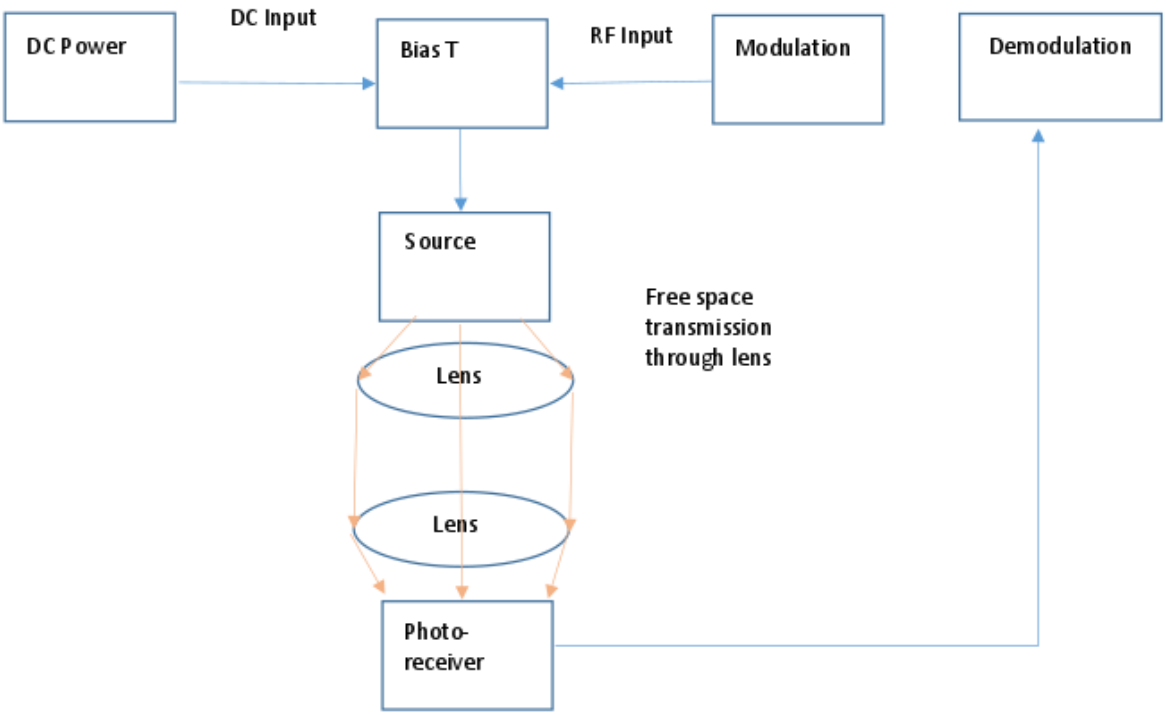

Figure 2.10: Block diagram showing the different system components for measurement of the μ-LEDs small signal frequency response.

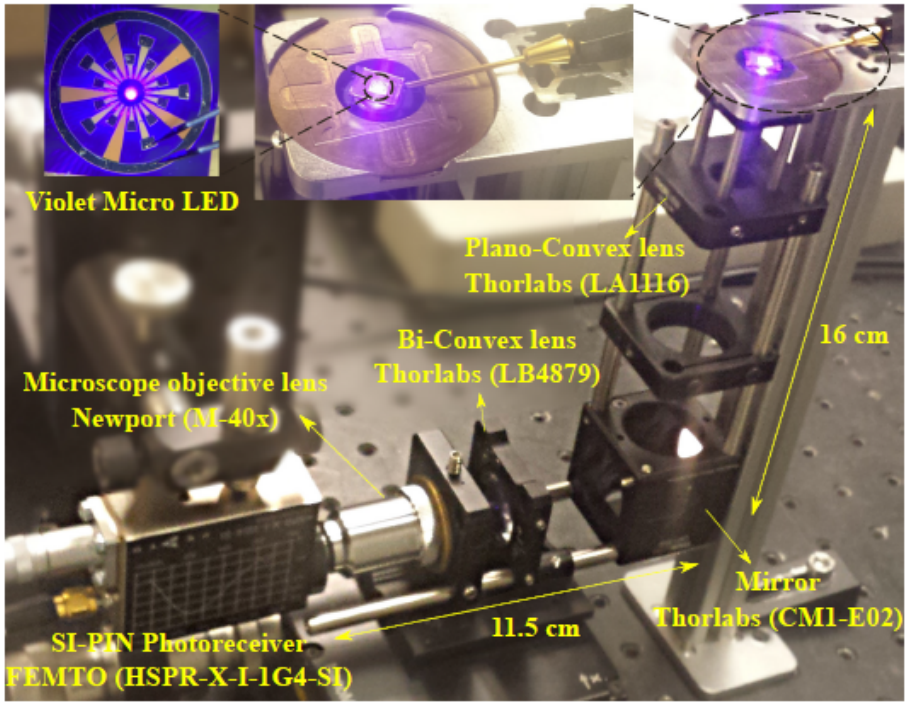

Figure 2.11: Photograph of the optical system showing the μ-LED, optical lens system, and the photoreceiver.

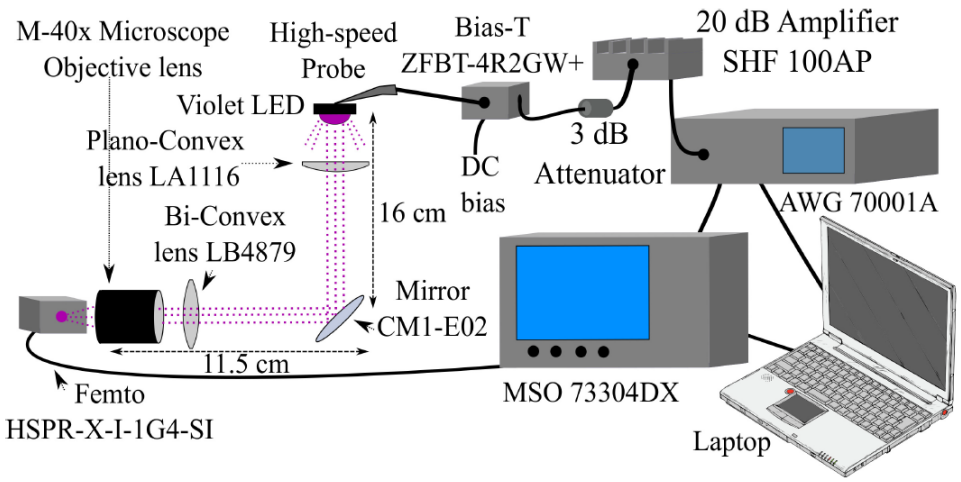

Figure 2.12: Schematic set-up of the experiment showing the optical system, AWG, oscilloscope, amplifier, attenuator, and Bias-T.

shown in Fig.2.12. The RF input to the bias-T was changed from the NA to the OFDM signal output from an arbitrary waveform generator (AWG). The output of the AWG is combined with a DC bias via a bias-T to generate a DC biased optical-OFDM (DCO-OFDM) signal. The OFDM signal was generated using a bespoke MATLAB script as described in section 2.3.1. The MATLAB script controlled the Tektronix AWG (AWG70001A) with a maximum sampling frequency of 50 GS/s and an ADC resolution of 10 bits per sample. The maximum output from this AWG is 0.5 V_{pp}. In order to better use the dynamic range of the μ-LED this signal was amplified with the use of a broadband amplifier (SHF 100AP) with a frequency range of 100 KHz to 20 GHz and a maximum gain of 20 dB. A 3 dB attenuator was placed at the output of the amplifier in order to allow the modulation depth to be varied and accurate assignment of a system power budget to utilize the dynamic range of the μ-LED. Finally, the output from the photoreceiver was connected to a Tektronix oscilloscope (MSO73304DX) for analysis instead of the NA. The oscilloscope was interfaced with a laptop to perform decoding and analysis in MATLAB. The following section gives the results and discussions from the experimental measurements described in this section for both the blue and violet devices.

2.4 μ-LED system characterisation and performance

This section reports the results from the characterisation of each system's transmitter source and the measurement of the system's communication performance. Two wavelengths of interest are investigated, these are 400 nm and 450 nm. These devices could potentially both find use in future VLC systems. With the superior colour rendering and reduced effects on circadian rhythm of devices at 400 nm, these are potentially more attractive for VLC systems in domestic spaces [82]. However, this is at a cost in terms of efficiency and, therefore, 450 nm devices may be more suitable for lower budget lighting. Additionally, blue lighting is more practical for

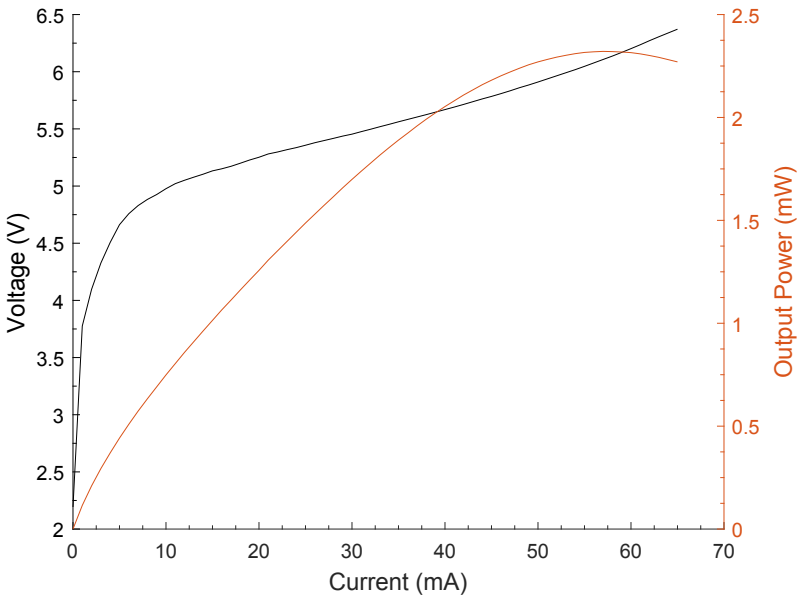

Figure 2.13: LVI curve of violet μ-LED at room temperature.

underwater VLC systems.

2.4.1 Violet μ-LED system

The novel violet μ-LED used in this work is of interest for a number of reasons. As the goal for such a device is utilisation in a VLC system then colour rendering is an important consideration. Using violet LEDs along with red, green and blue phosphors produces white light with a higher colour rendering index than the more common combination of blue light with a yellow emitting phosphor [83,84]. Additionally, it has been shown that direct blue light interferes with the human circadian rhythm [82]. Using a violet LED will eliminate the use of direct blue light. These advantages come with comparable internal quantum efficiency (IQE) to InGaN blue LEDs [85].

Firstly, the μ-LED was characterised by measuring its LVI, emission spectrum, frequency response and bandwidth. It is desirable for the system source to have high output power and a large dynamic range in the linear region of the LVI curve. This allows for the signal to have a large modulation depth. A larger modulation depth improves the SNR of the system and, therefore, the achievable data rate. Fig.2.13 shows the luminescence-current and voltage-current curves for the violet μ-LED. This curve is known as the LVI curve. The device has a turn on voltage of 4.60 V and a series resistance of 27 Ω. The maximum optical power achieved by this μ-LED is 2.32 mW. This demonstrates an improvement in optical power per unit of active area compared to previous violet μ-LEDs. The output power of the violet device in [78] was marginally higher at 2.5 mW. However, the active area was 2.88 times greater at 1256 μm^2. This improvement in performance can be attributed to the improved IQE of the commercial wafer used in the fabrication process of these devices. Additionally, improved Palladium p-type

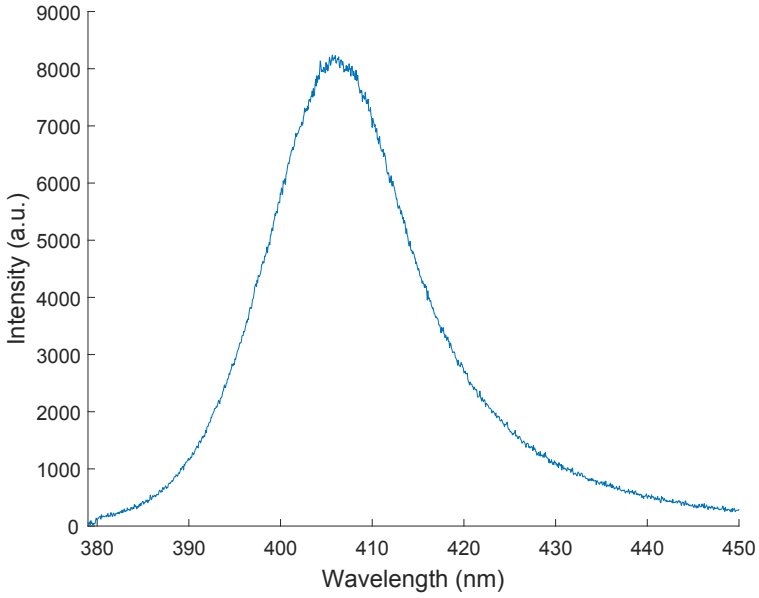

Figure 2.14: Wavelength spectrum for violet μ-LED at 50 mA.

contacts are a factor. All results in this section were achieved at room temperature without temperature control.

The output wavelength of the device was measured at a drive current of 50 mA. Fig.2.14 shows this wavelength with intensity plotted in arbitrary units (A.U.). Due to the spontaneous emission of the device a wide emission spectrum was measured. The wavelengths measured ranged from 380 nm to 450 nm. The peak wavelength was found to be approximately 407 nm. The intensity of the peak wavelength was 39 dB higher than that of the wavelengths at the edges of the emission spectrum.

The frequency response of the μ-LED was measured at varying drive currents ranging from 5 mA to 50 mA. Fig.2.15 shows the results of these measurements. Each response was measured at 801 points separated between the lower limit frequency of 100 KHz and an upper limit of 1.5 GHz. The lower limit was determined by the bias-T. Effects from the bias-T and SMA cables used were compensated for by calibration. Calibration is achieved by connecting the output port of the NA to the input with a direct electrical signal. The cables at the transmitter and receiver are connected through the bias-T, and the output from the NA is connected to the input through the cables and bias t directly without optical transmission. The inverse of this frequency response is then applied to future measurements. The bandwidth of the photodiode used for these measurements was 1.4 GHz, therefore, this response can be directly attributed to the μ-LED as the highest -3 dB optical modulation bandwidth measured was 655 MHz at a DC bias of 50 mA. This is the highest reported bandwidth for a violet wavelength LED.

The frequency response was used to calculate -3 dB optical modulation bandwidth as a function of DC bias and the result is shown in Fig.2.16. The bandwidth of the device increases as the DC bias increases up to a maximum of 655 MHz at 50 mA. This can be explained

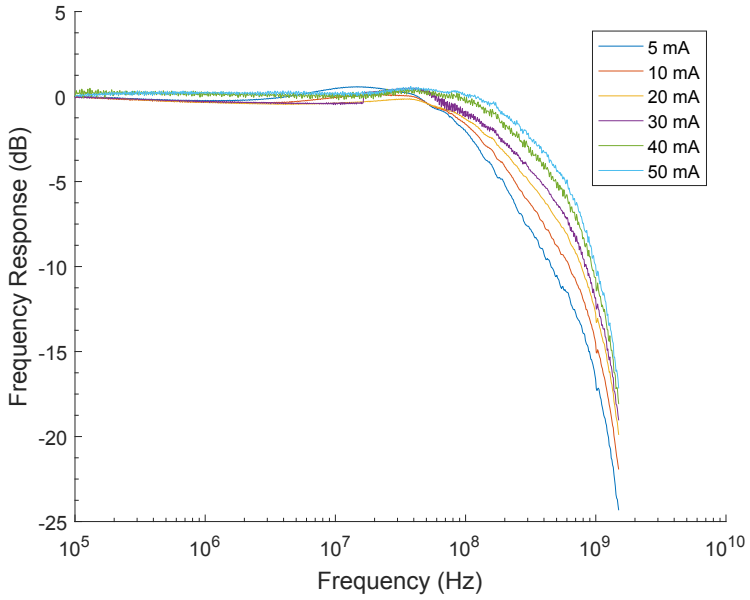

Figure 2.15: Small signal frequency response at DC bias currents from 5 *mA* to 50*mA*.

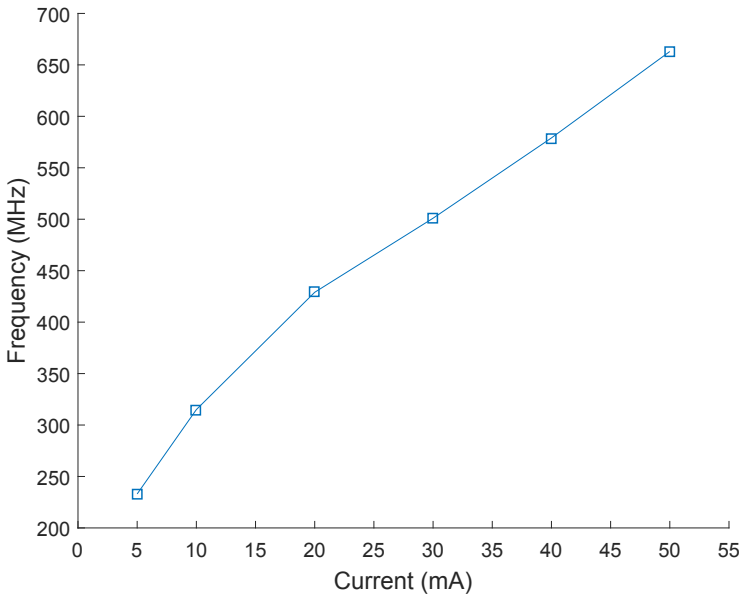

Figure 2.16: The -3 *dB* optical modulation bandwidth for DC bias currents from 5 *mA* to 50 *mA*.

by consulting the simple ABC model used for predicting carrier lifetimes in small bandgap semiconductors. This has been shown to be applicable with GaN-based μ-LEDs [86]. The total current, as defined by the ABC model, is given in Eq.2.10.

$$I = I_A + I_B + I_C = ead(AN + BN^2 + CN^3) \tag{2.10}$$

The total current through the device, I, is a combination of Shockley-Read-Hall, radiative and Auger currents (I_A, I_B, I_C). e, a and d are the electron charge, device area and device thickness

respectively. N is the carrier density per unit of volume within the QWs of the device. A, B and C are the Shockley-Read-Hall, radiative and Auger coefficients. Taking the derivative of the recombination rate with respect to carrier density gives Eq.2.11.

$$\tau^{-1}(N) = A + 2BN + 3CN^2 \tag{2.11}$$

τ is the differential carrier lifetime. This model assumes the A, B and C coefficients are independent of N and the carrier density is the same in all QWs. Therefore, the increase in bandwidth can be explained by assessing the effects of the carrier lifetime, τ , on the bandwidth. The carrier concentration increases with current density and therefore drive current when the active area is constant, as in this case. As N increases with increasing drive current then τ is reduced. The bandwidth dependency on τ is shown in Eq.2.12. τ can be the value of two different phenomena depending on the limiting factor of the device, it can be the carrier lifetime or the RC time constant of the device which is independent of carrier lifetime.

$$f_{3dB} = \frac{1}{2\pi\tau} \tag{2.12}$$

Given this relationship it can be understood the mechanism for increasing the bandwidth. This device has a higher bandwidth than previously reported violet LEDs. With comparable optical output power and improved bandwidth capabilities over the device in [78] this device performs better as a source in VLC as is shown later in this section. The improved bandwidth is as a result of reduction in size of the active area increasing current density. The bandwidth shows no sign of saturating as the device drive current is increased. It can therefore be inferred that the limiting factor on the bandwidth of these devices is the carrier lifetime and not the RC time constant. The RC limit is understood to become the limiting factor with devices on the order of 200 x 200 μm^2 [87].

The highest bandwidth measured for this device was at 50 mA, however, this was not the optimized DC bias for communications. As is stated in section 2.3.2 the modulating signal was 224 mV which avoids saturating the output power of the device. Using a higher modulation depth of V_{pp} = 2.36 V the optimum DC bias was investigated. By increasing the DC bias from 10 mA to 40 mA the optical power was increased and the optimum DC bias was determined. Fig.2.17 shows the data rate and BER for different optical powers corresponding to different DC biases. With a DC current of I_{DC} = 10 mA and a DC voltage V_{DC} = 4.16 V a data rate of 3.46 $Gbit/s$ was achieved at an optical power P_{op} = -4.95 dBm. The data rate increases to 4.91 $Gbit/s$ at an optical power of P_{op} = -2.29 dBm at this point the maximum data rate is achieved. This corresponds to a DC current of I_{DC} = 35 mA and DC voltage of V_{DC} = 5.21 V. At this point the data rate saturates and increasing the power does not improve the achieved data rate. This can be understood by consulting Fig.2.13 and recognising that increasing the DC optical power introduces higher clipping distortion with an applied modulation voltage of V_{pp} = 2.36.

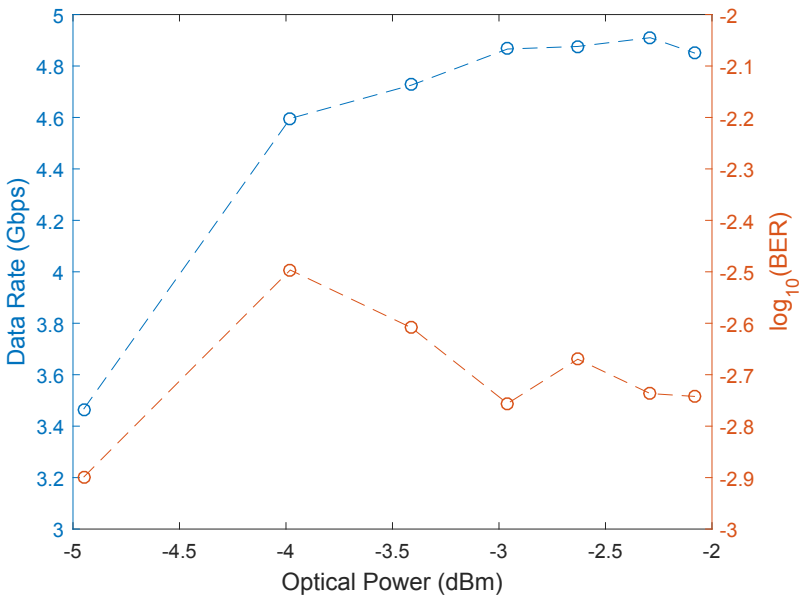

Figure 2.17: The data rate and BER versus different dimming levels at a modulation depth of $V_{PP} = 2.36\ V$. The values for the received optical power corresponds to DC bias values ranging from 10 mA to 40 mA.

The achieved BER in all of these cases is below the FEC limit. The DC bias selected for data communications was 30 mA. As is discussed next, it was beneficial to use a higher modulation signal to increase the SNR but this required a lower DC bias to reduce optical power saturation and therefore, biasing at 30 mA resulted in a higher achievable data rate.

The system SNR was investigated as a function of the modulation depth V_{pp}. As the modulation depth is increased the signal power, σ_x^2 , also increases. This is expected to increase the system SNR, however, large modulation depths can also introduce non linear distortion from clipping and optical power saturation. Fig.2.18 shows the estimated system SNR for three modulation voltages $V_{pp} = 1.96, 2.70, 3.88\ V$. The effects from non linear distortion are evident across the first 250 MHz as the SNR of the 2.70 V_{pp} is greater than that of the larger 3.88 V_{pp} signal. However, at higher frequencies the the 3.88 V_{pp} signal has the highest SNR. This is as a result of the attenuation at higher frequencies being offset by the larger modulation depth resulting in higher SNR. The improvement in higher frequency SNR outweighs the reduction in SNR of the lower frequencies from non linear distortion and the system performance was found to be best at 3.88 V_{pp} and 30 mA DC bias. The maximum -3 dB optical modulation bandwidth of this device was 655 MHz, however, data was encoded beyond this frequency due to adaptive bit and energy loading from the Levin-Campello algorithm [72] . Therefore, the SNR is shown up to 1.8 GHz.

The data rate versus BER system performance was measured using the optimized values of $I_{DC} = 30\ mA$ and $V_{pp} = 3.88\ V$. Fig.2.19 shows the maximum achieved data rate without averaging was 7.91 $Gbit/s$ with the BER below the FEC threshold of $3.8x10^{-3}$. This reduces to

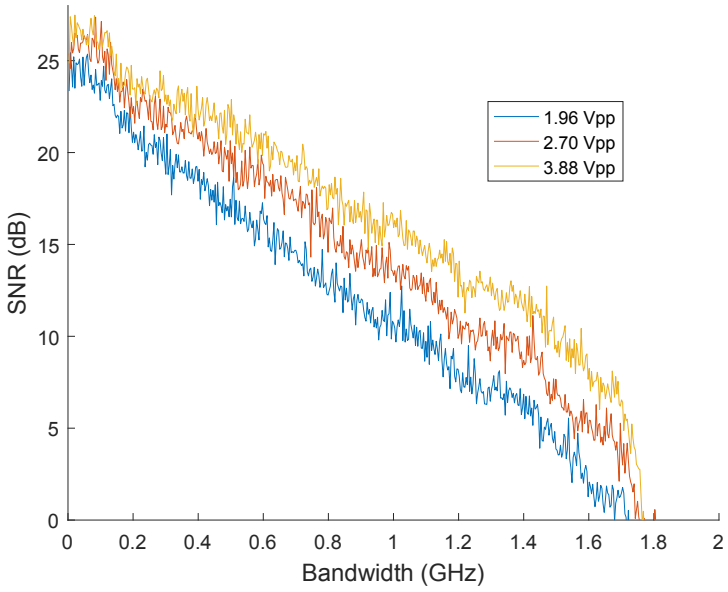

Figure 2.18: SNR versus frequency for different modulation depths at DC bias current I_{DC} = 30 mA. The values for the modulation signal swings corresponds to pumping the μ-LED with varying power levels from 5.85 dBm to 11.78 dBm.

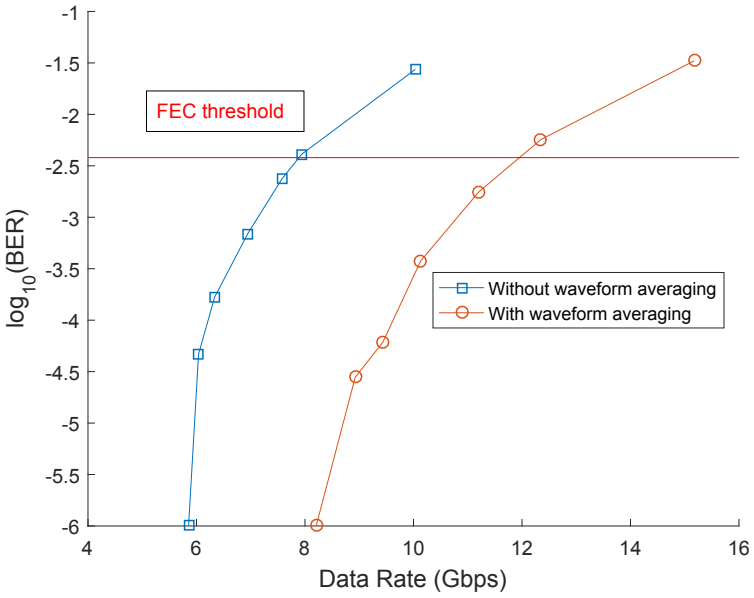

Figure 2.19: Data rates versus BER at DC bias current I_{DC} = 30 mA corresponding to P_{opt} = -2.6 dBm and modulation depth V_{PP} =3.88 V.

7.36 $Gbit/s$ when the FEC overhead of 7% is subtracted. This is the highest data rate achieved using a single μ-led as a source for a communication system. In order to asses the maximum achievable data rate when the only noise source is the non linear distortion from the μ-led itself, averaging is performed at the oscilloscope. This eliminates the AWGN from the photoreceiver. After averaging the maximum data rate achieved below the FEC limit for BER was increased

to 11.95 $Gbit/s$ which reduced to 11.12 $Gbit/s$ after subtracting the FEC overhead. The section that follows describes the system based on a blue wavelength μ-led as the source at the transmitter.

2.4.2 Blue μ-LED system

There are several reasons that blue μ- LEDs are of interest when designing a VLC system. It is possible to produce white light from blue LEDs when they are a combined with a yellow emitting phosphor. Fig.2.20a) and b) show the schematic design and emission wavelength for a typical white LED based on a blue emitting device combined with a yellow phosphor. In the future these white LEDs based on blue emission devices will be 63% more efficient than fluorescent lighting and 90% more efficient than incandescent lighting [88]. III- nitride LEDs emitting in the blue region have also been shown to have superior internal quantum efficiency than other wavelength devices [85]. Additionally, it is has been shown that for the state of the art high power LEDs in the visible spectrum InGaN blue LEDs have the highest external quantum efficiency [80]. These devices can find use in a variety of environments such as car interior lighting, external lighting and car headlights. Blue μ-leds are also a good candidate for underwater communications as blue light has the lowest attenuation coefficient in water. This work presents data transmission with a novel μ-led transmitting at 440 nm with the array design and geometry explained in section 2.2.

As was previously stated in section 2.4.1 it is desirable for a there to be a large dynamic range in the linear region of a device's LVI curve when it is to be used in communications. The LVI curve for the blue transmitter source is shown in Fig.2.21. The device was found to have turn on voltage of 5.4 V. The maximum optical power achieved by this μ-LED was 6.12 mW. This is a similar output power to previous blue μ-LEDs, although, in this instance there is a

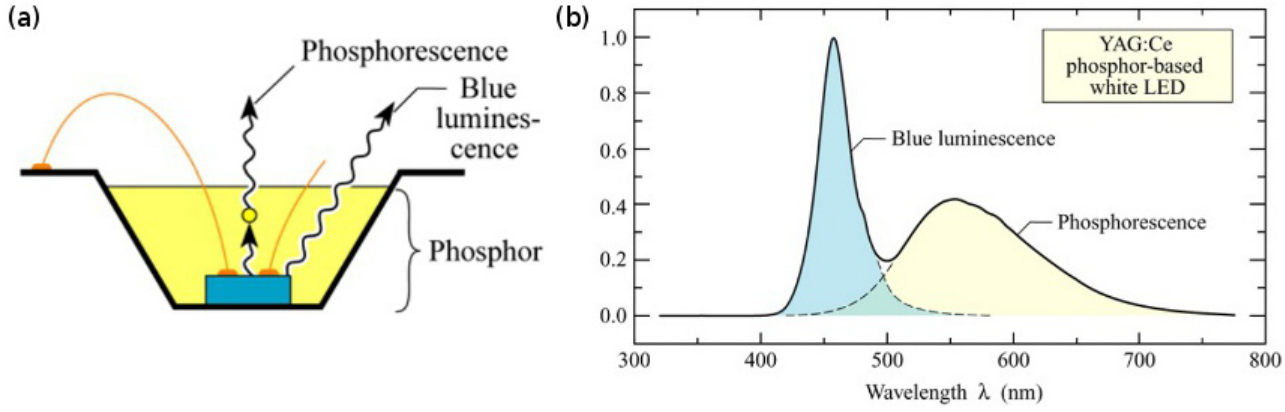

Figure 2.20: Conventional white LED (a) schematic and (b) emission spectra. In such a device, emission from a blue LED is combined with a yellow phosphor to produce an overall white light emission. [16].

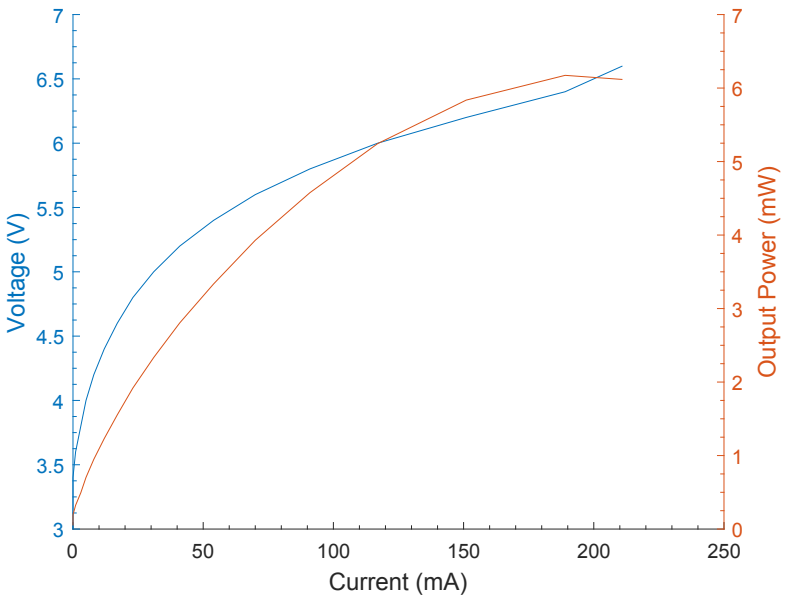

Figure 2.21: LVI curve of blue μ-LED at room temperature.

much smaller active area [70]. This results in a high bandwidth which is shown later in this section.

The spectrum of the blue μ-LED is shown in Fig.2.22. The maximum intensity wavelength of the device was at 437 nm with the broad spectrum ranging between 400 nm to 510 nm. This device measurement was taken with a 50 *mA* DC bias current. The maximum wavelength had

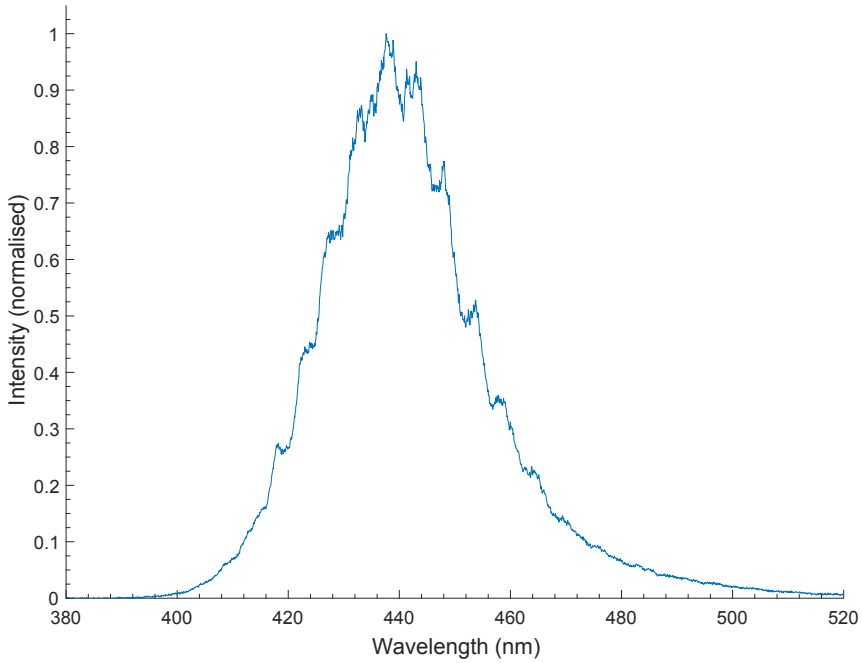

Figure 2.22: Wavelength spectrum for blue μ-LED at 50 *mA*.

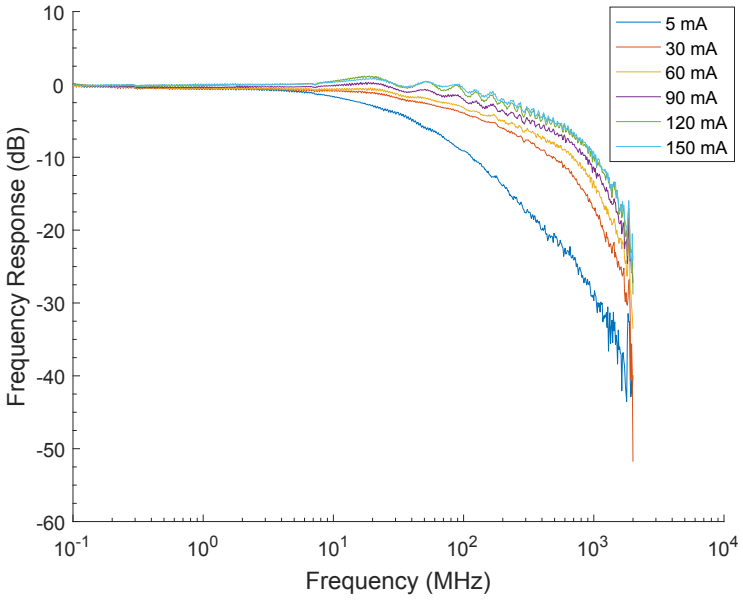

Figure 2.23: Small signal frequency response at DC bias currents from 5 *mA* to 150 *mA*.

an intensity 35 *dB* greater that of the wavelengths at the edge of the emission. The fringes may be as a result of a cavity in the LED.

The frequency response of the device was measured at drive currents from 5 *mA* to 150 *mA*. Fig.2.23 shows the results of these measurements.The same experimental method as is described in section.2.4.1 was used. The frequency response was then used to calculate the -3 *dB* optical modulation bandwidth at the different drive currents. This is done by calculating the frequency at which the signal magnitude has reduced by -6dB from its magnitude at the lowest measured frequency. -6dB in the electrical domain translates to a -3dB reduction in optical power. Fig.2.24 shows explicitly the maximum achieved bandwidth was 590 *MHz* at 150 *mA* drive current. This is directly attributable to the device as the device was the bandwidth limiting factor in the system. The increase in drive current results in a reduced carrier lifetime which increases the device bandwidth. A more detailed description of this is given in section.2.4.1. The carrier lifetime was found to be 28 *ns* at 150 *mA*. This is a reduced carrier lifetime in comparison to previous state of the art LEDs which were reported to have a carrier lifetime of 37 *ns* at < 0.05 $mA/\mu m^2$ [70]. Driving the blue μ-LED at 150 *mA* corresponds to a current density of 0.34 $mA/\mu m^2$. The increased bandwidth is attributed to the increased current density and reduced carrier lifetime.

Using the optimum settings with a drive current of 55 *mA* and a modulation voltage of 3 *Vpp* the BER of the system was measured as a function of the data rate as shown in Fig.2.25. The maximum successful data rate of the system was 6.4 $Gbit/s$ at a BER of $2.8x10^{-3}$. This reduces to 5.96 $Gbit/s$ when the FEC overhead of 7% is deducted. As in section 2.4.1 waveform averaging was introduced to eliminate the AWGN from the photoreceiver and the maximum data rate achievable with the device limiting the system was found to be 9 $Gbit/s$. Reducing to 8.37

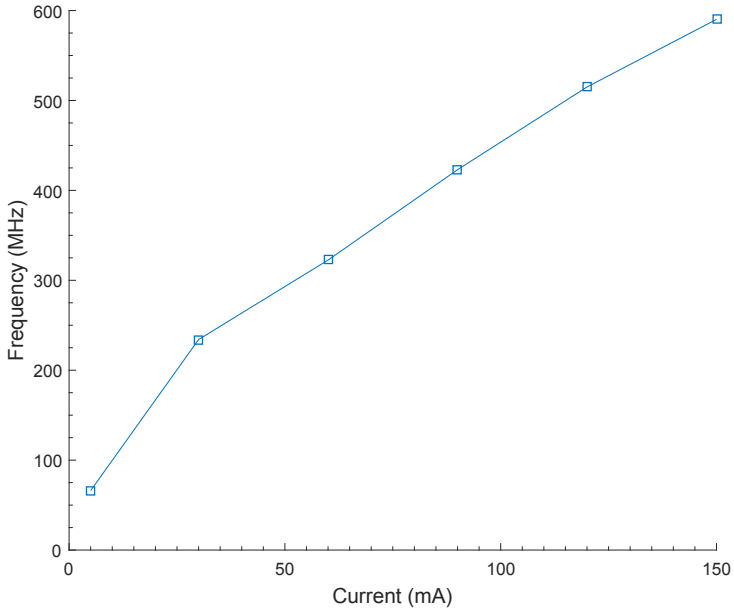

Figure 2.24: The -3 dB optical bandwidth for DC bias currents from 5 mA to 150 mA.

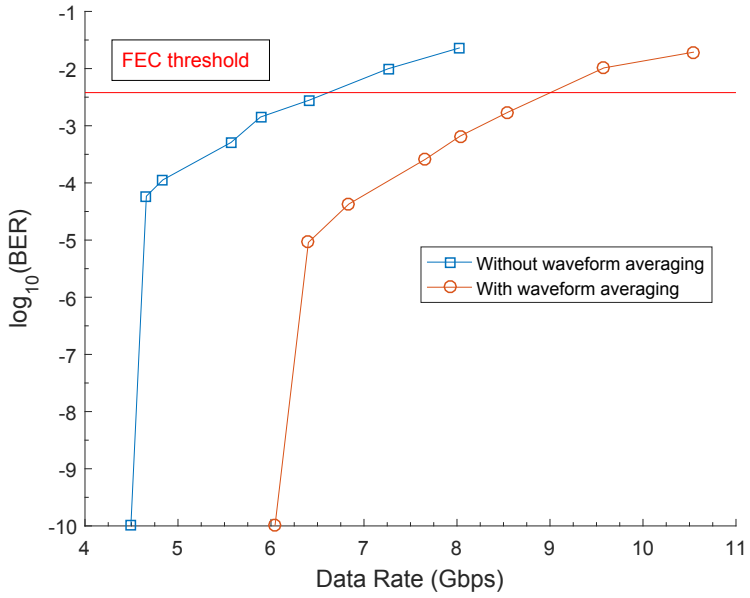

Figure 2.25: Data rates versus BER at DC bias current I_{DC} = 55 mA corresponding to P_{opt} = -2.6 dBm and modulation depth V_{PP} =3.88 V.

$Gbit/s$ after subtracting the FEC overhead. Previous blue LEDs have shown data rates up to 3 $Gbit/s$ [71]. This system surpasses that with a data rate of 6.4 $Gbit/s$.

2.5 Summary

In this chapter the performance of two VLC system based on GaN μ-LEDs, with an active area of 435 μm^2, has been investigated by analysis of the μ-LED's bandwidth and data transmission capabilities. The devices were characterized in terms of their LVI curves, emission spectrum and frequency response. Characterisation of the device allowed for selection of optimum biasing and modulation indices. The violet μ-LED was found to have an optical modulation bandwidth of 655 MHz which to the best of the author's knowledge is the highest modulation bandwidth reported for a violet wavelength LED. The maximum optical modulation bandwidth of the blue μ-LED was 590 MHz. Both these bandwidths were directly attributable to the μ-LEDs as in each system the μ-LED was the bandwidth limiting factor. These bandwidths were found to be dependent on the carrier density which can be explained by the simple ABC model for carrier recombination explained in this chapter.

Each device was then used as a source for a transmitter in a VLC OFDM system. The maximum data rate achieved for the violet system was 7.91 $Gbit/s$. To the best of the author's knowledge this is the highest data rate achieved for single μ-LED source communication system. The blue system was able to achieve 6.4 $Gbit/s$. These exceptionally high data rates where as a result of the high bandwidth capabilities of the μ-LEDs and the utilization of advanced modulation formats (QAM), multiplexing techniques (OFDM), along with bit and energy loading (Levin-Campello algorithm) allowing for efficient use of the system SNR. As a result of the bit and energy loading in the system transmission the utilised system bandwidth was extended beyond the 3 dB bandwidth to 1.81 GHz.

Finally, the device data transmission limit was ascertained by eliminating AWGN by averaging. This meant that the noise limitation on data transmission came solely from the μ-LEDs themselves. This enabled data transmission at 11.91 $Gbit/s$ for the violet system and at 9 $Gbit/s$ for the blue system.

Moving forward these devices would have to be implemented in a white light system to be used in a Lifi setting. It is common for LEDs to be combined with a phosphor to produce white light but this limits the system bandwidth. Different means of colour conversion such as quantum dots are faster and future work should look towards integration LED and quantum dot colour conversion. The fact that InGaN LEDs are subject to efficiency droop has been previously stated. However, the origin of this is not understood. Therefore, work could be done to better understand the recombination mechanisms in these devices and this will help improve understanding of efficiency droop.

Chapter 3

GaN based lasers for OFDM based communications

Chapter 2 described VLC systems based on μ-LEDs as sources for transmission. In this chapter the source of the two demonstrated systems is the Osram PL450B 450 *nm* laser diode. Lasers offer certain advantages over LEDs as sources such as better efficiency and bandwidth. Additional interest in blue lasers communications stems from the desire for increased data rate underwater communications. Therefore, current research is exploring blue laser communications in a number of capacities. For the two systems in this chapter the equipment and encoding scheme is varied with an NRZ-OOK and OFDM-QAM based system demonstrated. This chapter presents a brief history of lasers for VLC, laser advantages over LEDs, the device characterisation for the Osram PL450B and the results from transmission for the two communication systems.

3.1 Lasers based visible light communication background

Lasers have a history of use in commercial optical communications systems reaching back several decades. They have been applied in both free space and fibre based systems. Every day lasers are used for communication systems with applications in telecommunications, internet and LANs being a few examples. The first instance of a commercially available fibre-optic system came in 1980 [89]. The system achieved 45 $Mbit/s$ using a GaAs semiconductor laser source at 0.8 μm wavelength. POF is often utilized over shorter distances due to its low cost, ease of installation and resilience to mechanical stress. Recent achievements in this field have seen data rates of up to 5.3 $Gbit/s$ [90]. The laser diode used as the source for the transmitter in this section is a blue wavelength laser. Research into the use of blue lasers with fibre is limited. However, blue laser communications have been demonstrated through POF and water at a data rate of 2.5 $Gbit/s$ [91].

One of the factors driving research in underwater optical communications is the applications available for defence and oil and gas companies. For example, in off shore oil and gas

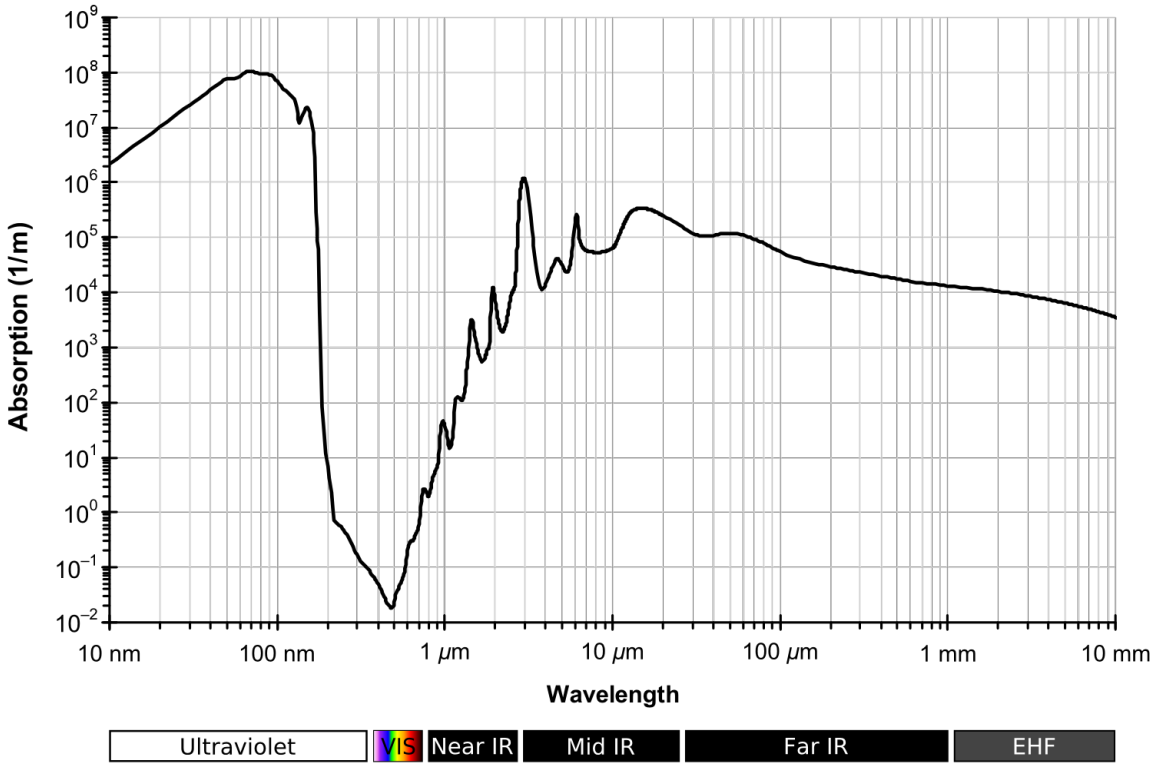

Figure 3.1: Absorption of light versus wavelength for water [95].

production, maintenance and monitoring of equipment is difficult and dangerous. UAVs (unmanned autonomous vehicle) are becoming the industry standard for this process. However, current systems rely on expensive cable systems which are inflexible once deployed or low data rate ultrasonic systems to communicate with these UAVs. Some advantages of underwater optical communications over ultrasound are the higher data rates, lower latency and elimination of acoustic noise. Blue light has the lowest underwater absorption in clear oceanic conditions as shown in Fig.3.1, therefore, current research is moving towards using blue light for underwater VLC systems to enhance and augment current ultrasound systems. Current commercially available blue underwater communication systems are capable of 500 $Mbit/s$ [92]. Nakamura *et al.* used a 405 nm laser to transmit underwater at a rate of 1.45 $Gbit/s$ [93]. This was over a distance of 4.8 m of fresh tap water using 64 QAM OFDM. There have been demonstrations of underwater optical communications at more practical distances but with lower data rates. Pontbriand *et al.* demonstrated an underwater VLC system with an omni-directional receiver and transmitter; the system was capable of transmitting 5 $Mbit/s$ over a range of 200 m in clear water [94].

As well as being the preferred candidate for underwater VLC systems, lasers are now being considered as a source for free space VLC systems. One application space where lasers could be used for free space communications is on road and vehicle to vehicle communications. Research is already emerging for the use of VLC in these areas [96, 97]. Lasers have the advantage of being a high power and high efficiency source and are already being utilised in car headlights [98].

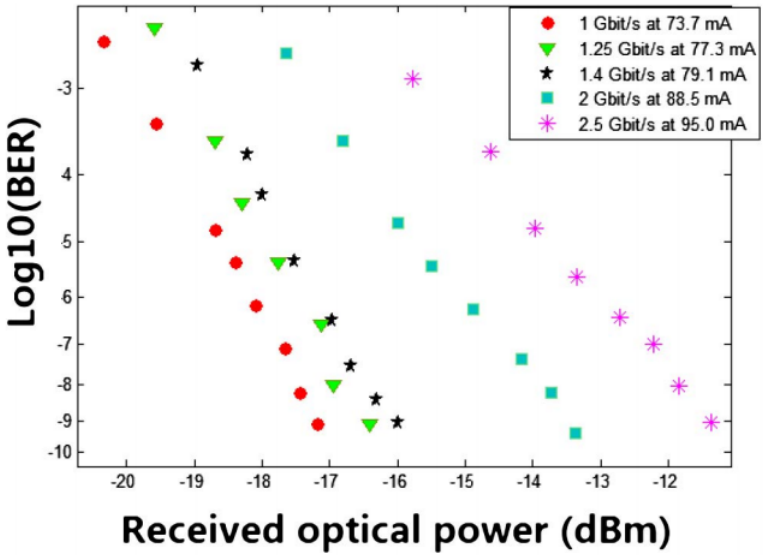

Figure 3.2: BERs versus received optical power at 1, 1.25, 1.4, 2 and 2.5 $Gbit/s$ at optimum bias currents for each bit rate, using a limiting amplifier after the receiver. [99].

Lasers also offer an alternative to LEDs in Lifi and VLC systems. They have the advantage of higher bandwidth and higher efficiency over LEDs [20]. These advantages are discussed in section 3.2. Laser-based VLC has been demonstrated using a number of modulation formats. Using NRZ-OOK has shown data rates of up to 4 $Gbit/s$ [99, 100]. Fig.3.2 shows the optical power versus data rate achieved by Watson *et al.* using blue laser NRZ-OOK for communication. Using multi-carrier modulation schemes such as OFDM for laser-based VLC has achieved transmission speeds as high as 9 $Gbit/s$ [101].

3.2 Laser advantages

One of the main advantages of lasers over LEDs as a source for a VLC system is that lasers do not experience efficiency droop. When using AlInGaN LEDs as a source increasing the current density in the device reduces the efficiency. This leads to a trade off between bandwidth and efficiency as increasing the current density will increase the bandwidth. Fig.3.3 shows the EQE versus the forward current for a Phillips Luxeon I LED [102]. There is much debate over the source of this efficiency droop with possible causes being identified as screening of excitons, inefficient carrier injection and Auger recombination [86, 103, 104]. In order to overcome the phenomenon of efficiency droop and fabricate devices with high efficiency and high bandwidth it is necessary to better understand the carrier dependence of non-radiative recombination in GaN LEDs. Green *et al.* demonstrated a valid method of analysis of differential carrier lifetimes in 450 nm emitting μ-LEDs using the simple ABC model which is applicable when describing carrier lifetime in narrow gap semiconductors [86]. When using the ABC model the carrier

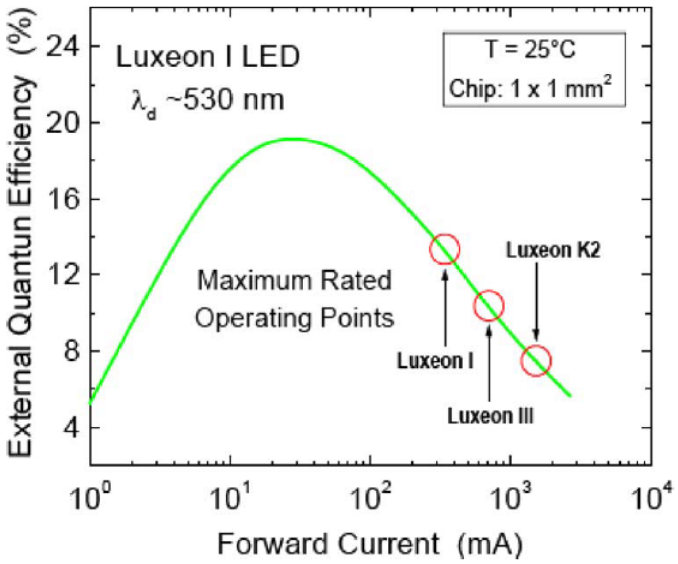

Figure 3.3: External quantum efficiency of commercial green LEDs (Philips Lumileds' Luxeon line) as a function of operating current. Maximum rated operating currents of three different Luxeon models are indicated [102].

lifetime can be described by Eq.3.1.

$$\tau^{-1}(N) = A + 2BN + 3CN^2 \tag{3.1}$$

where, A, B and C are the Shockley-Read-Hall non-radiative recombination, radiative recombination and Auger recombination coefficients, respectively. By measuring the bandwidth the carrier lifetime can be calculated using Eq.3.2.

$$f_{3dB} = \frac{1}{2\pi\tau} \tag{3.2}$$

By varying the drive current, and measuring the bandwidth at each current, the carrier density in the quantum wells as a function of current, $N(I)$ can be found using the integral in Eq.3.3.

$$N(I) = \frac{\eta_{inj}}{ead}\int_0^I \tau dI \tag{3.3}$$

Where η_{inj} is the internal quantum efficiency of the LED, e is the elementary charge, a is the active area of the LED and d is the active region thickness. Green *et al.* used a value of 0.7 for η_{inj} from the literature in there analysis.

The current through the device can be split into radiative current, I_r and non radiative current, I_{nr}. Therefore, Eq.3.4 gives the total current through the device.

$$I = I_r + I_{nr} \tag{3.4}$$

The total current, I, radiative current, I_r, and the non radiative current, I_{nr} are given by:

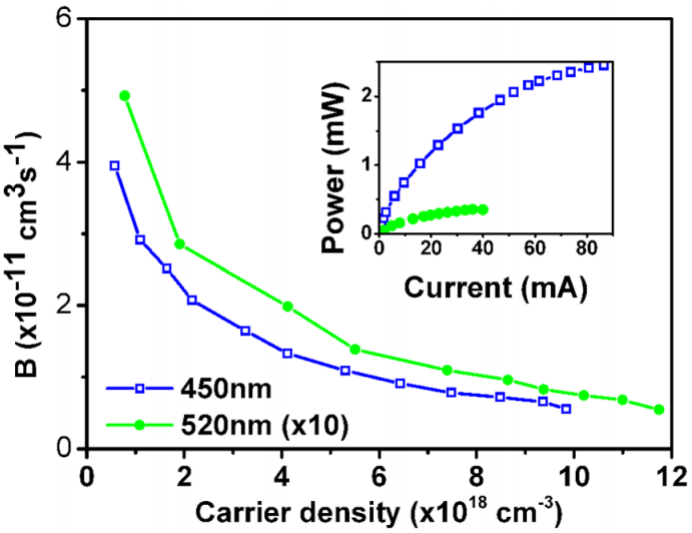

Figure 3.4: Values of the radiative coefficient B obtained from the LI curves for 44 μm diameter 450 nm emitting and 54 μm diameter, 520 nm emitting devices. (Inset) LI data for the same two devices. [86].

$$I = ead(A + BN^2 + CN^3) \tag{3.5}$$

$$I_r = ead(BN^2) \tag{3.6}$$

$$I_{nr} = ead(A + CN^3) \tag{3.7}$$

Eq.3.6 would indicate that the curve of I_r versus N^2 would be a straight line with gradient $eadB$. Using the LI curve of an LED the radiative current can be estimated using Eq.3.8.

$$I_r = e \times (\frac{P}{\hbar\omega \times \eta_c}) \tag{3.8}$$

where P is the LED output wattpower in Watts, $\hbar\omega$ is the energy of the emitted photons in Joules and η_c is the collection efficiency. It can be found when looking at the literature that the curve of I_r versus N^2 is not a straight line as expected from Eq.3.6. It is then assumed that B is a function of N and the function is defined by Eq.3.9.

$$B = \frac{1}{ead}\frac{dI_r}{dN^2} \tag{3.9}$$

From the LI data and making legitimate assumptions regarding collection efficiency Green *et al.* found values of B shown in Fig.3.4.

Now a means of establishing B has been described the next step before use of the ABC model is finding the other two coefficients A and C. By interpolating the plot of carrier lifetime versus current density it is possible to arrive at the value of τ_0, the value of τ when the carrier

density N=0. Then using $A = \frac{1}{\tau_0}$ the value of A can be determined. Given values for A and B it is assumed that the remainder of the current is due to Auger recombination. From Eq.2.10 the Auger current I_c can be calculated. The value of C is then given by Eq.3.10.

$$C = \frac{1}{ead}\frac{dI_c}{dN^3} \tag{3.10}$$

The C coefficients of the GaN LEDs calculated in this manner by Green *et al.* showed good agreement with the literature [105–108]. Therefore, this analysis demonstrates that GaN LEDs can be assessed using the ABC model. Where Shockley-Read-Hall and Auger recombination are the only significant non-radiative recombination mechanisms and any carrier overflow mechanisms or variation of the injection efficiency do not have a great effect on τ.

Lasers avoid this phenomenon, unlike LEDs the carrier density in a laser does not continue to increase pass the threshold carrier density as the current increases. This can be understood from the assessing the photon and carrier density in the active area of a laser. The photon density is given by Eq.3.11.

$$n_p = \frac{\Gamma_a v_g \tilde{g}\frac{n_{sp}}{V_p}}{\frac{1}{\tau_p} - \Gamma_a v_g \tilde{g}} \tag{3.11}$$

Where Γ_a is the mode confinement factor, v_g is the wave group velocity, $\tilde{g}$ is the gain, n_{sp} is the spontaneous emission factor, V_p is the effective mode volume and $\frac{1}{\tau_p}$ is the photon lifetime in a Fabry-Perot cavity. The important terms to consider here are the optical loss, $\frac{1}{\tau_p}$ and the optical gain, $\Gamma_a v_g \tilde{g}$. As the carrier density increases so does the gain, $\tilde{g}$, this results in an increasing optical gain until the denominator approaches zero causing the photon density to greatly increase. This increase in photon density will reduce the carrier density in the active area. This made clear by considering the laser rate equation for carrier density given in Eq.3.12.

$$\frac{dn}{dt} = \frac{\eta_i I}{qV_a} - [R_{nr}(n) - G_{nr}(n)] - [R_r(n) - G_r(n)] - v_g \tilde{g} n_p \tag{3.12}$$

Assuming steady state where $\frac{dn}{dt} = 0$ and rearranging the Eq.3.12 gives Eq.3.13. If the current I is increased in Eq.3.13 this increases the stimulated emission term $v_g \tilde{g} n_p$. Increasing the current increases the gain, $\tilde{g}$, in Eq.3.11 as gain is a function of carrier density, this results in higher photon density which increases the stimulated emission resulting in the carrier density being held equal. Therefore Eq.3.13 remains valid with the number of injected carriers being equal to the rate at which the carriers are depleted meaning a constant carrier density above threshold in the laser's active region.

$$\frac{\eta_i I}{qV_a} = [R_{nr}(n) - G_{nr}(n)] + [R_r(n) - G_r(n)] + v_g \tilde{g} n_p \tag{3.13}$$

Unlike LEDs the bandwidth of a laser is not dependent on the minority carrier lifetime τ

as shown in Eq.3.14. It is instead dependent on the photon lifetime τ_p. The maximum 3 dB bandwidth is given in Eq.3.14.

$$f_{3dB|max} = \frac{\sqrt{2}}{2\pi\tau_p} \tag{3.14}$$

This is the frequency at which the RF power has decreased by 3 dB from its power at zero frequency. This can be understood by first considering the modulation response of the laser $H(f)$. This is given by Eq.3.15.

$$H(f) = \frac{\omega_R^2}{(\omega_R^2 - (2\pi f)^2) - i(2\pi f)\gamma} \tag{3.15}$$

If we consider the variables governing the modulation response function $H(f)$ the reliance on the τ_p becomes clear. Firstly considering ω_R which is the relaxation oscillation frequency of the laser given by Eq.3.16.

$$\omega_R = \sqrt{\frac{1}{\tau_{st}\tau_p}} = \sqrt{v_g \left.\frac{d\tilde{g}}{dn}\right|_{ss} n_p} \tag{3.16}$$

The relaxation oscillation frequency increases with the square root of the photon density, n_p, Therefore increasing the current density increases the 3 dB modulation frequency as can be seen when considering Eq.3.15. However, as the current increases eventually the modulation frequency will stop increasing. This is as a result of the damping factor γ in Eq.3.15. This is given by Eq.3.17.

$$\gamma = \frac{1}{\tau_r} + \frac{1}{\tau_{st}} = \frac{1}{\tau_r} + v_g \left.\frac{d\tilde{g}}{dn}\right|_{ss} n_p \tag{3.17}$$

As the photon density increases so does the damping factor at a rate faster than the relaxation oscillation frequency. When the laser current is slightly higher than threshold current then $\omega_R \gg \gamma$ because $\frac{1}{\tau_p} \gg \frac{1}{\tau_{st}} + \frac{1}{\tau_r}$ where τ_p is the photon lifetime, τ_{st} is the differential stimulated emission time and τ_r is the differential recombination time. As the current increases so does $f_{3dB|max}$, however, eventually increasing the current results in $\omega_R = \frac{\gamma}{\sqrt{2}}$. At this point the oscillation peak in $H(f)$ does not occur, as depicted in Fig.3.5, and the $f_{3dB|max} = \frac{\omega_R}{2\pi} = \frac{\sqrt{2}}{2\pi\tau_p}$. Increasing the current beyond this decreases $f_{3dB|max}$. Therefore, the maximum 3 dB modulation frequency is determined by τ_p as described in Eq.3.14.

In addition to the advantages of higher bandwidth and efficiency laser-based illumination has already been shown to produce high quality colour rendering for white light illumination using multiple coloured sources and using phosphor colour converters [37, 38]. Recently, distributed feedback (DFB) lasers in GaN have been demonstrated making high channel density in WDM VLC systems possible in the future [110]. With these advantages visible light lasers are an interesting source for communication systems. The following section describes the characterisation

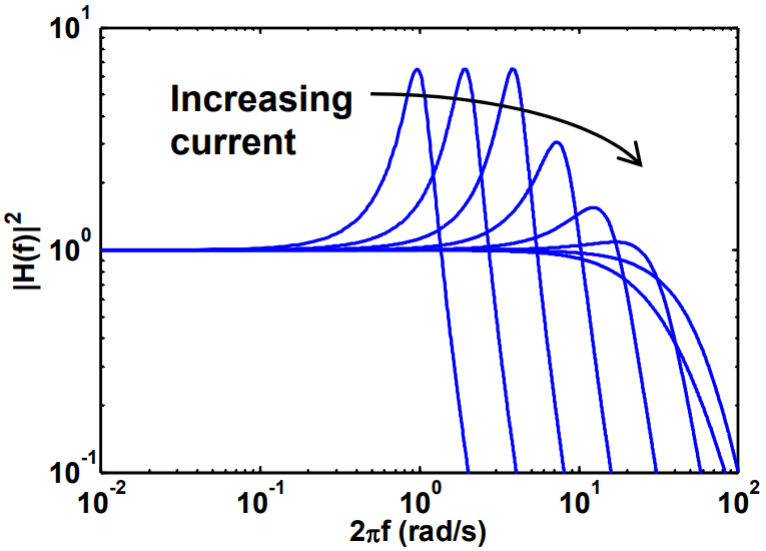

Figure 3.5: Square of magnitude of modulation response versus frequency. This depicts the elimination of the resonant peak at higher drive currents [109].

of the Osram PL450B laser which is used for the communication systems in sections 3.4 and 3.5.

3.3 System laser source characterisation

The first part of this section describes the experimental setup and process for characterization of the Osram PL450B laser which was used as the source for the communication systems described in sections 3.4 and 3.5. The LVI, emission spectra and bandwidth of the device were measured. The results of these measurements are detailed and discussed in section 3.3.2.

3.3.1 Experimental setup

The laser diode used for transmission is OSRAM's PL450B device with a nominal emission wavelength of 450 *nm*. The LVI characteristics of the device were experimentally obtained at 17°C and are shown in Fig.3.8. The temperature was maintained with the use of a temperature controller (ILX Lightwave LDT-5910) with TO-38 can laser diode connected to a heatsink. The pins of the laser were connected directly to an SMA cable. The threshold current of the device is 25 *mA* at a turn-on voltage of 4.29 V. The laser diode output was collected and collimated with a microscope lens (0.40 NA, x20 magnification). The distance between the laser and the photoreceiver was 15 cm. The free space link between the transmiiter and receiver lens was approximately 2 cm. The transmitted beam was then focused onto a power meter (Newport 1918-R) with a second microscope lens (0.25 NA, x10 magnification). The laser and lens setup are depicted in Fig.3.6. After surpassing the threshold, the power received at the power meter increased from 0.1 μW until a maximum reading of 3.82 mW.

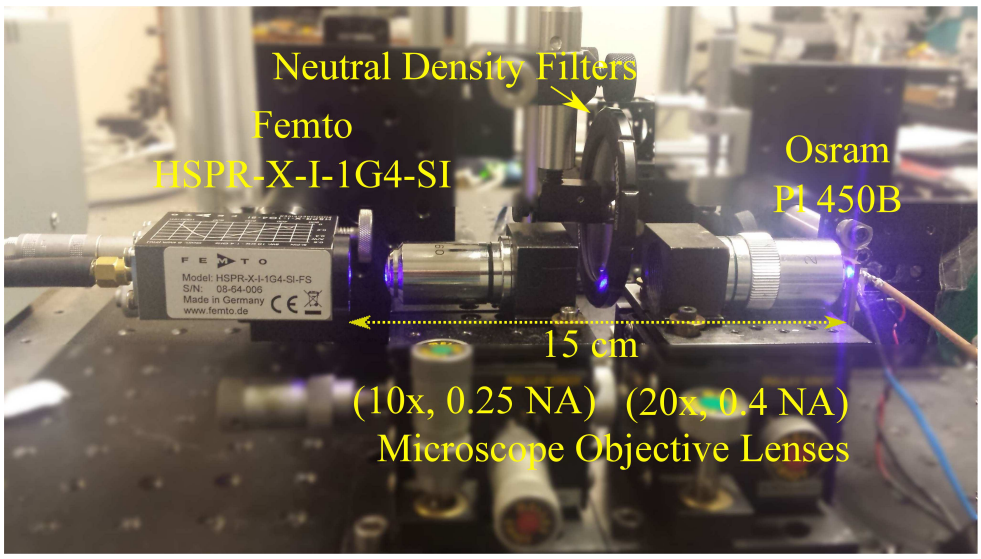

Figure 3.6: Photograph of the optical system showing the laser, optical lens system, and the photoreceiver.

The power meter was then replaced with a spectrometer (Ocean Optics USB 4000 Miniature Fibre Optic), whilst the lens configuration was maintained, and the wavelength of the laser light was measured at varying drive currents. The results are exhibited in Fig.3.9. The laser spectral width is less than 1 nm and exhibited the typical Fabry-Perot red shift in wavelength with increasing current. The optical modulation bandwidth and the small signal frequency response were then measured using a network analyser (Agilent HP 8753ES). A DC power supply and a 224 mV AC signal from the network analyser are combined via a bias-T (ZFBT-4R2GW+) and connected directly to the laser diode. After collecting and collimating as per LVI and spectral measurements, the light is focussed onto the 0.4 mm effective active diameter of a high-speed silicon PIN photodiode (Femto, HSPR-X-1G4-SI-FS), with a 3 dB bandwidth of 1.4 GHz, shown in Fig.3.6. The photoreceiver is connected to the network analyser which measures the frequency response. The system block diagram is shown in Fig.3.7 The system frequency response at drive currents from 40 mA to 120 mA is shown in Fig.3.10. The maximum optical modulation bandwidth of the system was found at a drive current of 50 mA shown in Fig.3.11. However, at higher drive currents where the laser bandwidth is expected to continue to increase, the system response is limited by the photoreceiver.

3.3.2 Results and discussion

The LVI characteristics of the device were experimentally obtained and are shown in Fig.3.8. This LVI curve was measured at the position of the photodetector after losses through transmission and the optical setup as shown in Fig.3.6. The device has a turn on voltage of 4.29 V. The maximum optical power received at the photodetector was 50 mW at a current of 90 mA. The VLC systems mentioned in the following sections are therefore operating at higher data rates

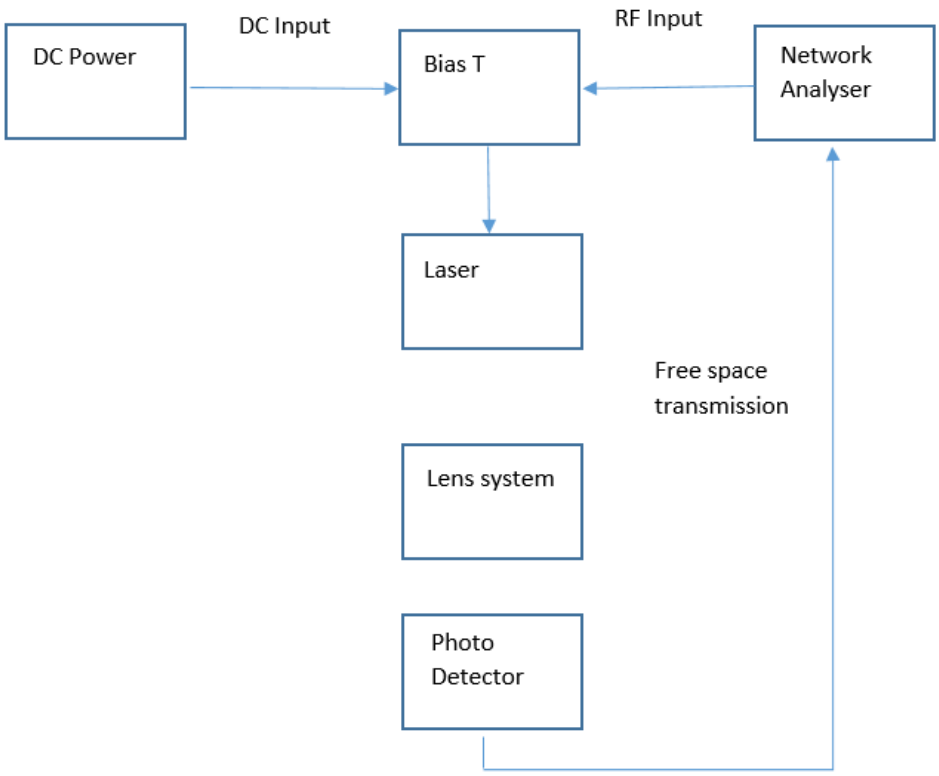

Figure 3.7: Block diagram showing the different system components for measurement of the laser's small signal frequency response.

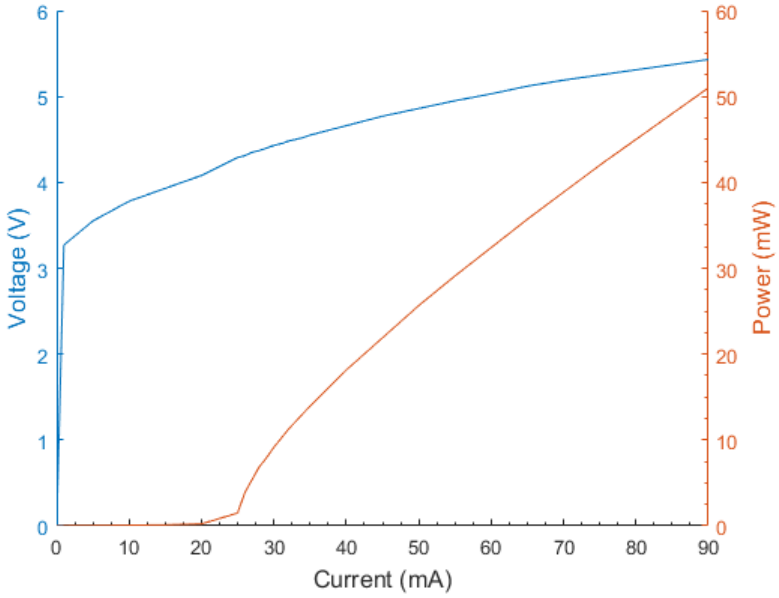

Figure 3.8: LVI curve of the Osram PL450B laser at 17°C.

with the same magnitudes of power levels to previous state of the art laser based systems [99].

Fig.3.9 shows the Osram PL450B spectra at drive currents from 30 *mA* to 80 *mA* in steps of 10 *mA*. The measured linewidth of the laser is approximately 0.5 *nm* with the resolution of the

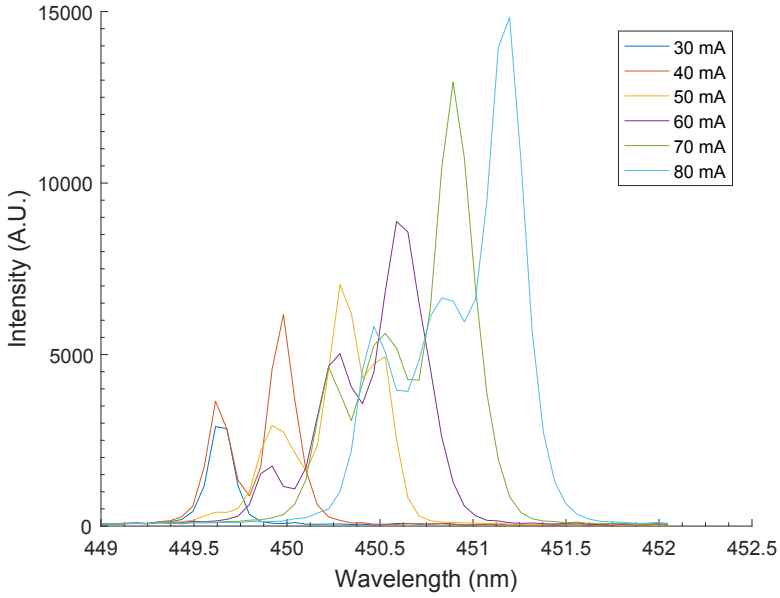

Figure 3.9: Emission spectra for Osram PL450B laser at drive currents from 30 *mA* to 80 *mA*.

spectrometer limiting this measurement. There are multiple peaks in the spectrum at each drive current, these are different FP cavity modes. These modes have no effect on the modulation in a free space system. As the drive current increases the emitted wavelength shifts towards a longer wavelength.

The normalised small signal frequency response is shown in Fig.3.10. A 224 mV AC sinusoidal signal was combined with DC bias currents from from 40 mA to 120 mA in steps of 20 mA. The system is calibrated to compensate for the effects of the SMA cable and bias-T at the transmitter. As can be seen in Fig.3.10 the highest bandwidth was found at a drive current of 50 mA. The - 3 dB optical modulation bandwidth is shown as a function of drive current in Fig.3.11. It can be seen that the bandwidth increases with drive current until it reaches a maximum of 1.8 GHz at a drive current of 50 mA. It then reduces to 1.4 GHz where it remains despite the increasing drive current. The bandwidth of the laser is expected to increase with increasing drive current but is limited by the bandwidth of the photoreceiver in the system which has a bandwidth of 1.4 GHz. As the current is increased the resonance frequency of the diode is increased. At 50 mA the resonance of the diode is still effective and increases the bandwidth to 1.8 GHz. However, as the drive current is increased the resonance of the diode increases beyond 1.4 GHz which is the limit of the photoreceiver and therefore does not affect the optical modulation bandwidth.

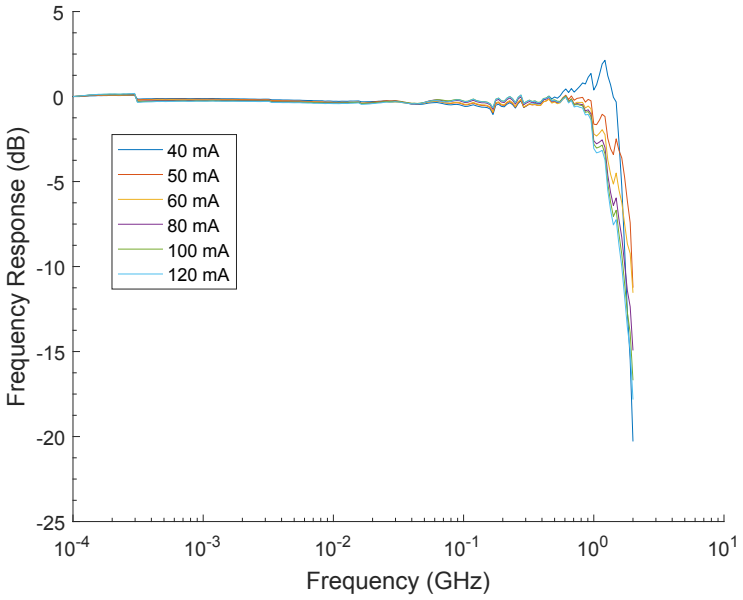

Figure 3.10: Frequency response of Osram PL450B laser at drive currents from 40 *mA* to 120 *mA*.

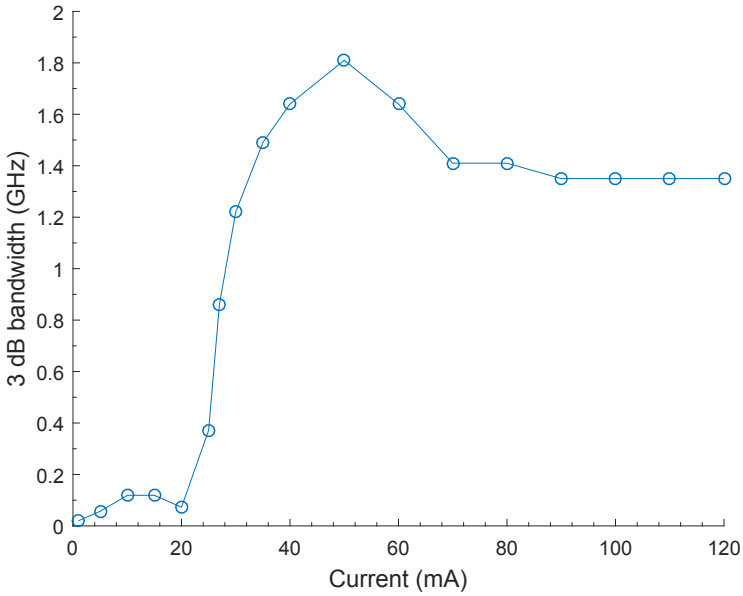

Figure 3.11: -3 *dB* bandwidth as a function of drive current.

3.4 NRZ-OOK

NRZ-OOK is a line coding scheme where binary data is represented by two different light intensity levels. This is distinct from RZ coding where the signal rests at zero for a time during each bit period. Fig.3.12 shows the NRZ OOK line coding schemes. When NRZ-OOK is employed as the line coding scheme it is possible to maintain low electronics costs compared to more complex modulation formats and multiplexing techniques. NRZ-OOK is used with 8b/10b

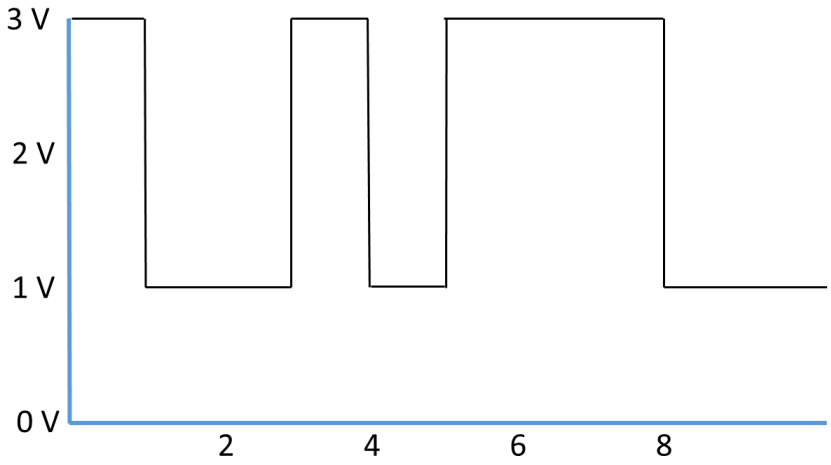

Figure 3.12: Time domain of NRZ OOK signal.

encoding scheme in IEEE 802.3-2015 for gigabit ethernet and, therefore, is a possible candidate for use in VLC systems in the future both in free space and underwater. This section describes the experimental research into the data transmission capabilities of a blue VLC system using the Osram PL450B and NRZ-OOK modulation. The highest data rate for a blue VLC system using NRZ-OOK was achieved at the time when these results were published.

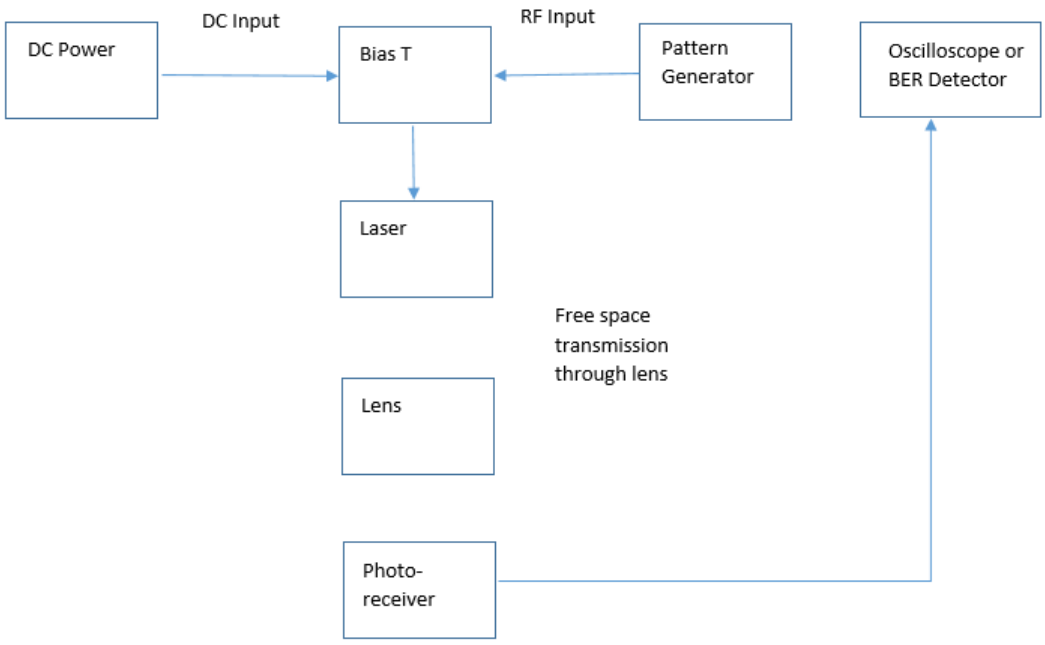

Figure 3.13: Block diagram showing the different system components for measurement of BERs and eye diagrams.

3.4.1 Experimental setup

The system block diagram for the NRZ-OOK measurements is shown in Fig.3.13. In this system an NRZ-OOK signal was produced using a PRBS pattern generator (Anritsu MP1763c). The data rate was determined by setting the clock frequency with a network analyser (Agilent HP 8753ES) . The PRBS was $2^7 - 1$ bits long to be consistent with current applications like Ethernet which use encoding schemes such as 8-B/10-B. The signal voltage was set at 2 V, which was the maximum available peak to peak voltage, as this allowed for the lowest optical power whilst retaining error free transmission. The NRZ-OOK signal was combined with a DC source at bias-T before being connected to the Osram PL450B. The free space transmission and optical setup are shown in Fig.3.6 with the photoreceiver maintained from this setup also. Eye diagrams were measured using an oscilloscope at different data rates as shown in Fig.3.14.

The oscilloscope was replaced with the BER detector. Bit error rate (BER) measurements of the NRZ-OOK system were measured using a BER detector (Anritsu MP1764C). Using a neutral density filter the optical power was varied and the corresponding error rate was measured for four data rates. Fig.3.15 demonstrates these measurements.

3.4.2 Results and discussion

Fig.3.14.(b) shows the eye diagram at 1.5 Gbit/s, with the error rate a multiple of 10^{-9}, at a drive current of 107.1 mA. The eye diagrams and BER was measured as described in section.3.4.1. The bit rate was set at the pattern generator and the received optical power was varied using a ND filter. This changed the BER. At the lower bit rate of 1.5 Gbit/s it was possible to further reduce the received optical power by introducing a low noise amplifier (RF Lambda RLNA01M10GC) between the photoreceiver and error detector. This avoided reaching the lower limit of voltage the error detector could distinguish between. Fig.3.14.(a) shows the eye diagram at 4.7 Gbit/s. This eye diagram, although with a lower Q factor than at 1.5 Gbit/s, was producing an error rate at $< 9 * 10^{-9}$ at a drive current of 64.8 mA. At 4.7 Gbit/s the eye amplitude has increased from 22.6 mV to 86.1 mV due to the higher required power for error free transmission at this data rate. However, it can be seen there is not a corresponding increase in the eye height. The eye height is maintained at around 22.6 mV for the faster signal. There is a power penalty associated with this data rate increase.

When measuring the BER at different optical power the current was varied to find the optimal drive current for each bit rate. This optimal drive current ranged from 54.1 mA to 107.1 mA for data rates from 1.5 Gbit/s to 4.7 Gbit/s. The required optical power for error rates $< 9 * 10^{-9}$ at 1.5, 2, 3, and 4.7 Gbit/s was -18.81, -16.90, -14.20 and -7.37 dBm respectively, as shown in Fig.3.15. The expected power increase required from 1.5 Gbit/s to 3 Gbit/s whilst maintaining error free transmission is 3 dBm, as the data rate has doubled we would expect the required power to double. However, the increase in power required is 4.61 dBm resulting in a power

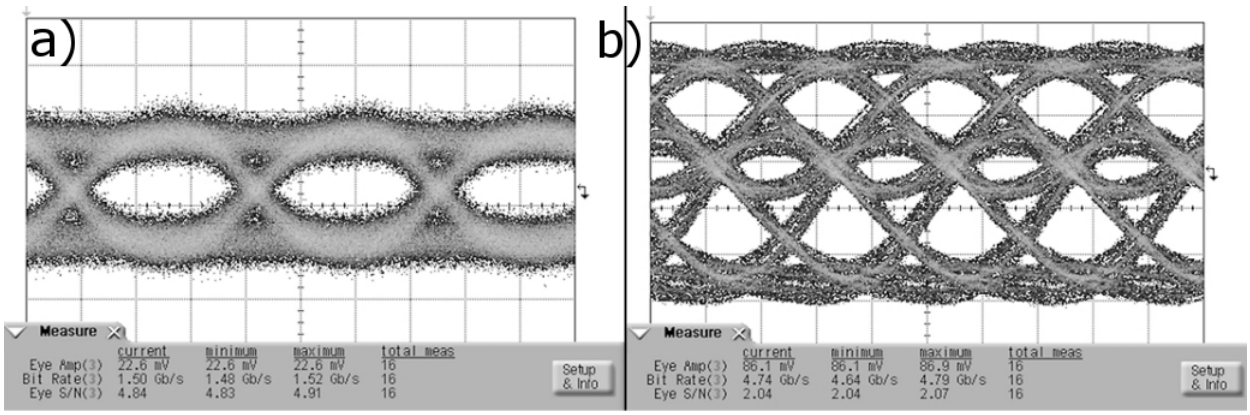

Figure 3.14: Two Eye diagrams showing error-free data transmission on the left at 1.5 Gbit/s and on the right at 4.7 Gbit/s.

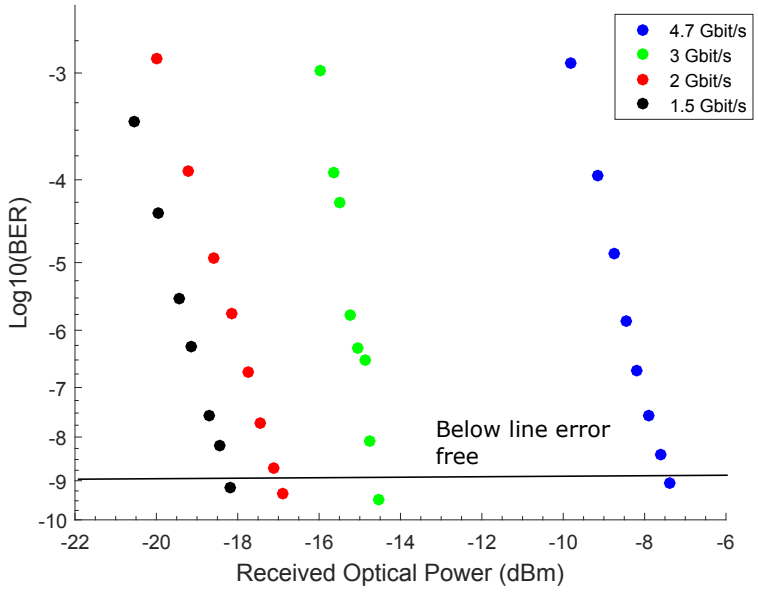

Figure 3.15: Log of the BER versus received optical power at 1.5, 2, 3 and 4.7 $Gbit/s$ at optimum bias currents for each bit rate.

penalty of 1.61 dBm. The same analysis shows a penalty in excess of 3 dBm whilst transmitting at 4.7 Gbit/s. Looking at Fig.3.14 from the eye diagram at 4.7 Gbit/s we see that a power increase is required to maintain the eye height at high frequency which means a corresponding low frequency power increase.

3.5 OFDM system

It is possible to improve data rates across a set bandwidth by introducing more complex multiplexing techniques and advanced modulation formats. Following on from the NRZ-OOK system described in the previous section, this section describes an OFDM-QAM based VLC system.

The optical system and Osram laser were maintained from the previous system with the equipment at the transmitter and receiver updated to facilitate the more complex multiplexing and modulation. OFDM QAM offers advantages over NRZ-OOK. The higher spectral efficiency of OFDM over NRZ-OOK means it is possible to achieve higher data rates with the same channel bandwidth. Using OFDM QAM along with adaptive bit loading it was possible to achieve a data rate of 15 Gbit/s which is three times the achieved data rate with the NRZ-OOK system in the previous section. Additionally, ISI is lower in OFDM as the symbol period can be reduced due to OFDM being a multicarrier modulation scheme. OFDM is utilized in current standards such as IEEE 802.1 and HyperLAN2 and as seen as a potential candidate for standards for wireless VLC systems [111]. This section describes a system utilizing the high bandwidth of the Osram PL450B laser as a transmitter along with both a complex multiplexing technique and modulation format to produce the highest reported data rate for a VLC system.

3.5.1 OFDM implementation

The OFDM is implemented in a similar fashion to the OFDM implementation as described in section 2.3.1 when μ-LEDs where the source for transmission. Once again DCO-OFDM is utilised for VLC and Hermitian symmetry is imposed [71]. The number of points in the FFT (N_{fft}) is equal to 1024 in this experiment. After exhaustive experimental measurements the cyclic prefix length (N_{cp}) was set to 5 which prevented any significant ISI. The PAPR is reduced by setting the upper and lower clipping clipping at as +3σ and -3.5σ respectively. Where σ is the standard deviation of the time domain signal. These settings for clipping and carrier number come from the Matlab OFDM provided by the University of Edinburgh. The values are found by adjustment of parameters and observation of system BER. A priori estimated SNR is used to determine bit and power allocation to each carrier. This loading is determined by the Levin-Campello algorithm [72]. The SNR is estimated Fig.3.16 shows the bit and energy loading of subcarriers. The channel capacity is also shown as described by Shannon [81]. The a priori estimated SNR is achieved using the channel estimation described by Wang *et al.* [112].

The OFDM signal is generated using MATLAB. The analog OFDM waveform is then produced using an arbitrary waveform generator (Tektronix AWG70001A), with a DC bias added via a bias-T and used to modulate the laser. The lens configuration is maintained from the device characterization stage described in Section.3.3 and a FEMTO photoreceiver is placed at the receiver (HSPR-X-1G4-SI-FS). The output from the detector is fed to the oscilloscope (Tektronix MSO73304DX) and analysed by MATLAB. The optical setup is shown in Fig.3.6.

3.5.2 Results and discussion

The drive current was varied and each time the system SNR and BER were measured. The a priori SNR is defined and measured as described in the previous section based on the work by

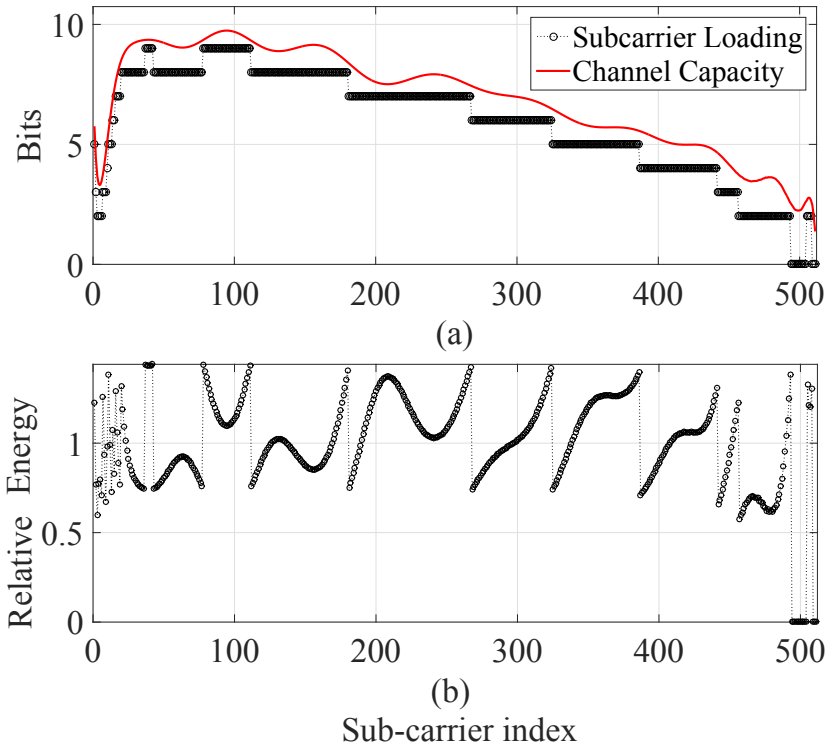

Figure 3.16: (a) The bit loading and channel capacity per subcarrier, both given in bits per subcarrier. (b) Energy loading per subcarrier.

Wang *et al.* [112]. The BER is the ratio of correct bits to bits in error, i.e. if 1 in 1000 bits is in error the BER is 1 x $10^{-}3$. This is measured by sending a known symbol and doing a cross correlation between the transmitted and received binary data. The optimum bias drive current was found at 65 mA. The optimum peak to peak voltage was 500 mV. Fig.3.17 shows the SNR over the 15 cm link at different drive currents. We can see that by increasing the drive current from 60 mA to 70 mA there is a noticeable improvement in the SNR of the high frequency subcarriers. However, the inset in Fig.3.17 also details the modest reduction in SNR at lower subcarriers attributed to the optical power saturation of the detector. Therefore, we found 65 mA to be the optimum drive current at which the combination of increased high frequency SNR and limited low frequency saturation resulted in the highest system data rate. Fig.3.19 shows the BER versus data rate for the 15 cm link. The black horizontal line in the figure demonstrates the FEC criterion BER. From the figure, it can be seen that 15 Gbit/s data transmission can be achieved below the FEC threshold. The FEC criterion is the BER at which error free transmission can be achieved when forward error correction coding is utilized.

The optical power at the receiver was then varied using a neutral density filter wheel which varies the SNR and therefore achievable data rate. Fig.3.18 shows the optical power required for different data rates whilst maintaining the BER below the FEC criterion. This shows that the optical power can be reduced to 1 dBm and still transmit successfully at 14 Gbit/s. The data rate saturates at higher optical power and this demonstrates the possibility to increase the trans-

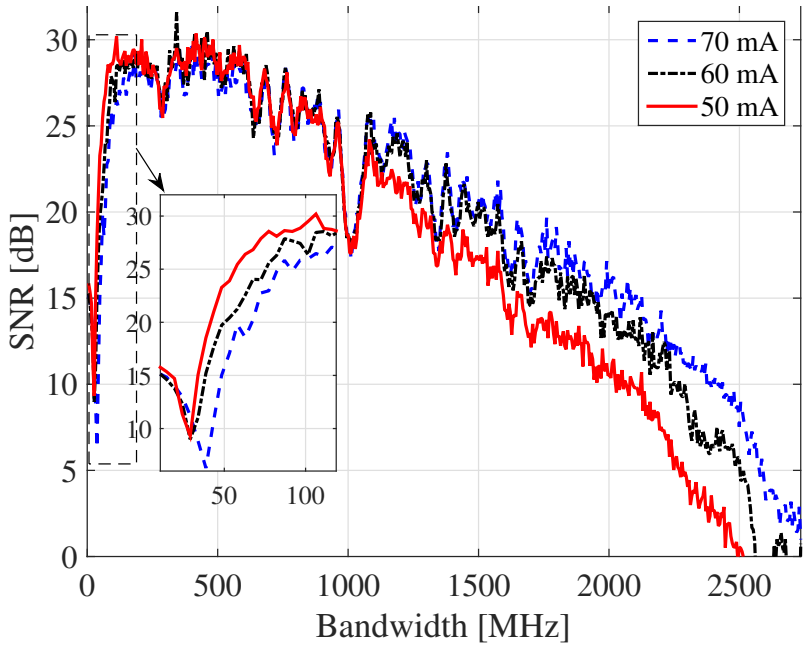

Figure 3.17: The SNR across the utilized bandwidth for different biasing levels.

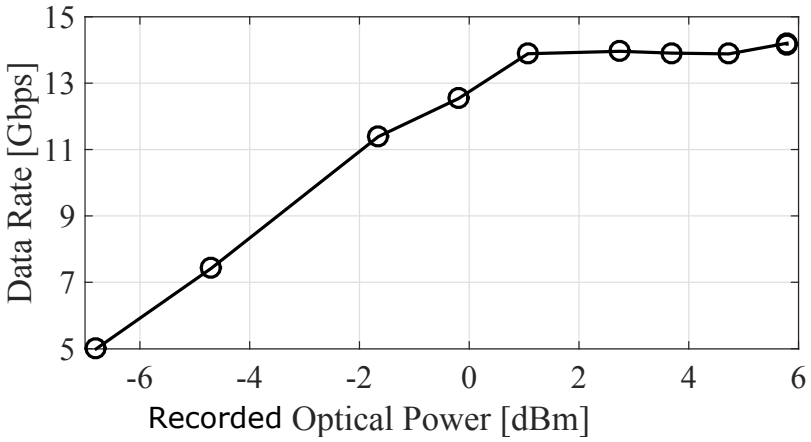

Figure 3.18: Data rate versus optical power over 15 *cm* link.

mission distance and maintain high data rates. The transmission distance was then increased to 197 cm. The receiver lens, previously a microscope lens, was replaced by a larger aspheric lens (Thorlabs ACL7560U-A). The drive current and peak to peak voltage are maintained. The successful data transmission is reduced to 13.5 Gbit/s as shown in Fig.3.19. The reduction in SNR at this distance compared to transmission at 15 cm results in a lower successful data rate. Lower SNR means that the QAM order on the carriers is reduced and therefore the number of bits loaded onto the carrier is reduced. This results in lower spectral efficiency.

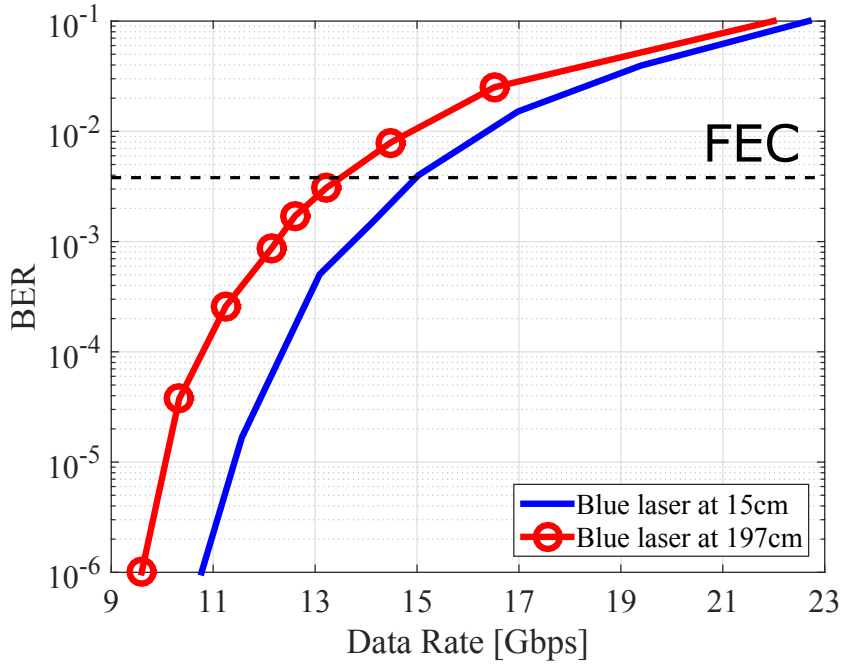

Figure 3.19: Data rate versus BER over 15 *cm* and 197 *cm* link.

3.6 Summary

In this chapter the performance of two VLC systems using the Osram PL 450B blue laser as a source has been described. Firstly, the characterization of the device has been reported in terms of its LVI curve, emission spectrum, frequency response and bandwidth. The system was found to have a maximum bandwidth of 1.8 GHz at 50 mA. At higher drive currents the system bandwidth was limited by the bandwidth of the photo-receiver.

The laser was then used to transmit data using NRZ-OOK as the modulation format. The system was able to transmit data at up to 4.7 Gbit/s error free using this modulation format. To the best of the author's knowledge this was the fastest data transmission for NRZ-OOK using a blue laser. It was found that driving the system at 4.7 Gbit/s resulted in a power penalty in excess of 3 dBm.

To further assess the data transmission capabilities of this device OFDM was utilized as a multiplexing technique along with the more complex modulation format QAM. This resulted in a data rate of 15 Gbit/s with the error rate below the FEC criterion. This increase in data rate showed the merits of moving to advanced multiplexing and complex modulation formats. The use of adaptive bit and energy loading allowed the utilised bandwidth to be extended beyond the 3 dB bandwidth to 2.5 GHz. To the best of the author's knowledge this is the highest data rate achieved for a single source VLC system.

Chapter 4

GaN DFB laser for communications

This chapter presents a VLC system using a GaN based DFB laser at violet wavelength (408 *nm*). In this chapter a brief introduction is given about DFB lasers explaining why they are of interest to the community and a basic explanation of their operation. After this a more specific explanation of the devices used as a VLC source in this chapter is given, along with an explanation of the state of the art. The penultimate section gives details of the experiment and results for characterisation of the violet DFB laser. The final section of this chapter demonstrates the data transmission capabilities of this novel device.

4.1 Operation and applications of DFB lasers

The output wavelength of a DFB laser is limited by closely coupling a diffraction grating to the active region as show in Fig.4.1. There is a mirror on one side of the active region reflecting photons into the gain medium and the diffraction grating acts as a Bragg reflector providing feedback for the desired wavelength creating a resonator and selecting a single longitudinal mode. A description of the coupled wave theory for DFB lasers has been published by Kogelnik and Shank [113]. The lasing wavelength is equal to the Bragg wavelength given in Eq.4.1.

$$\lambda = 2n_{eff}\Lambda \tag{4.1}$$

Where λ is the laser wavelength, n_{eff} is the effective refractive index and Λ is the periodicity of the grating.

Complications arise in the fabrication of gratings for GaN DFB lasers. Fig.4.2 depicts the process for fabrication of a narrow ridge waveguide laser. Initially staring with a blank wafer Pd is deposited as a p contact. The ridge waveguide is then defined using photoresist and a mask before the surface is etched to produce the ridge. Using a ridge waveguide allows single lateral mode operation. After the ridge is defined the device is insulated by coating the surface in an insulator which is selectively removed from the top of the ridge to allow a conductive contact

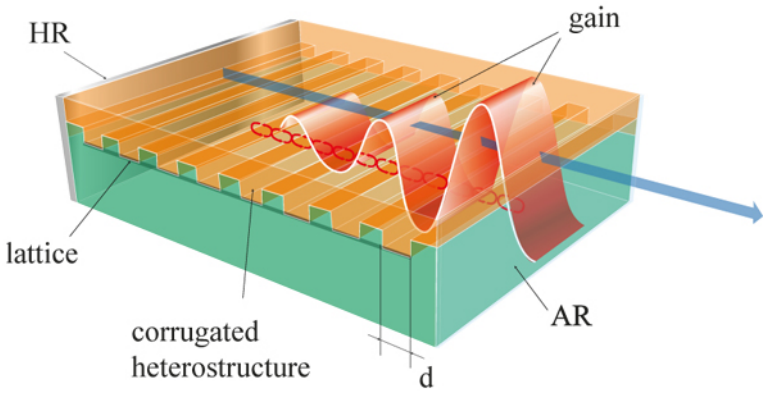

Figure 4.1: Optical arrangement of a distributed feedback semiconductor laser. HR - High Reflection mirror; AR - antireflection coating [114].

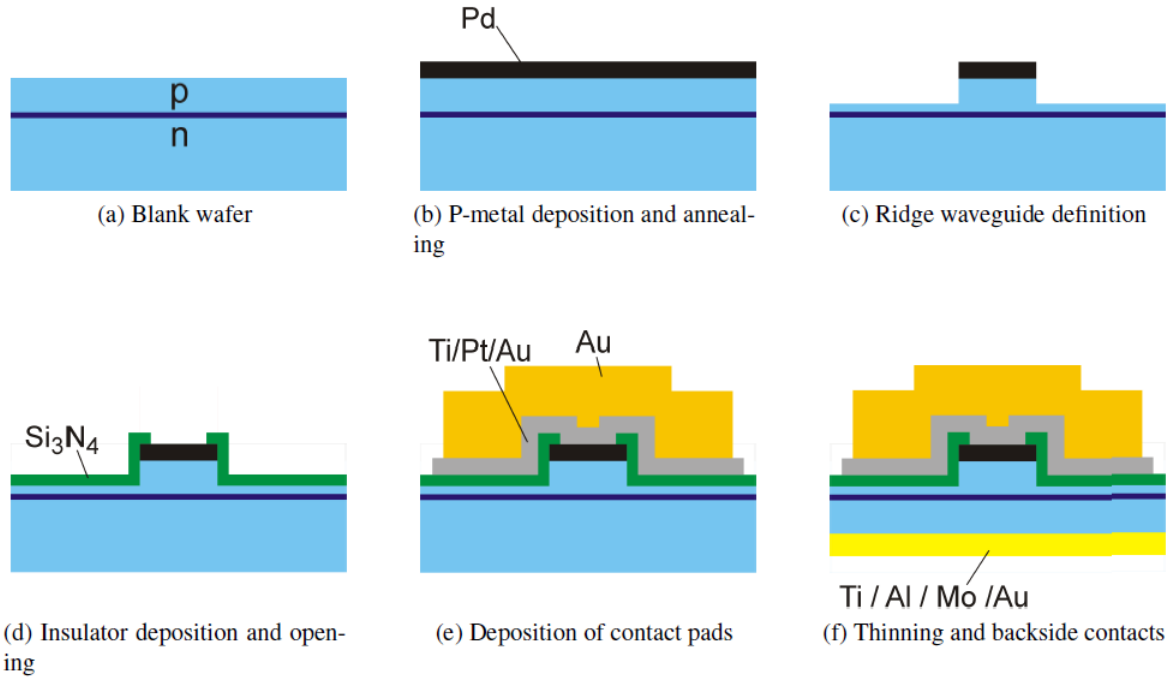

(a) Blank wafer

(b) P-metal deposition and annealing

(c) Ridge waveguide definition

(d) Insulator deposition and opening

(e) Deposition of contact pads

(f) Thinning and backside contacts

Figure 4.2: Illustration of the main processing steps for the fabrication of RW laser diodes [115].

to the p region. Large metal contacts are then deposited on the top and bottom of the laser. However, this design has no ridge grating and will therefore have multiple longitudinal modes.

The simplest way of fabricating a single longitudinal mode laser is by placing the grating outside the active region of the laser and fabricating a DBR laser as is shown in Fig.4.3.a). However, InGaN laser diodes have strong internal polarization fields which cause issues with absorption in non electrically pumped QWs in the grating region [116]. Another method shown in Fig.4.3.b) is the use of buried gratings. These require complex overgrowth steps which can introduce higher levels of non radiative recombination from threading dislocations caused by surface defects from interrupting the growth process. Fig.4.3.c) shows a surface etched DFB laser. When surface gratings are used ion etching induced damage can detrimentally effect the

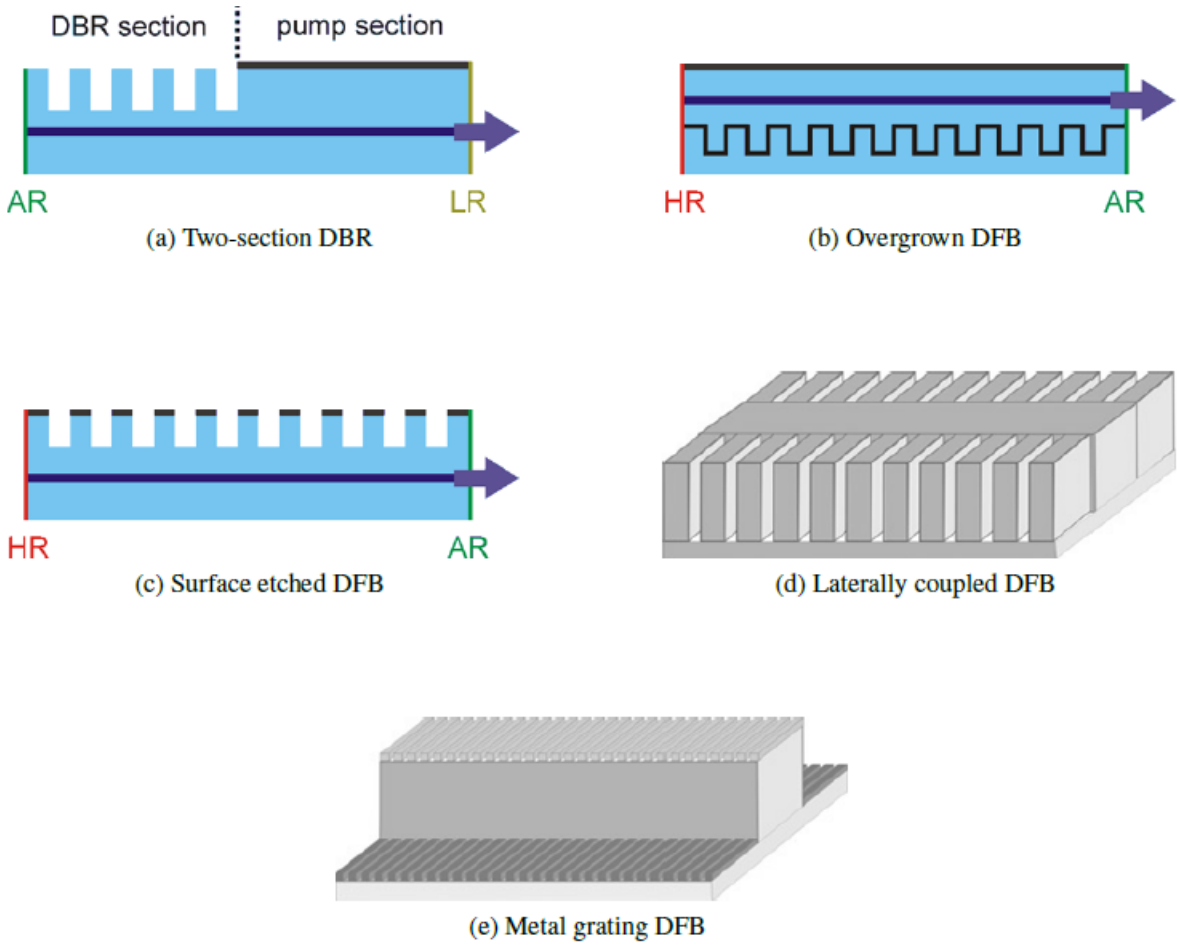

Figure 4.3: Different implementations of Bragg-gratings in laser diodes [115].

p-type contact. Additionally, surface grating designs also have higher optical losses in the un-pumped grating region. It is possible to address some of these peroblems using shallow etched lateral grating design shown in Fig.4.3.d). To increase coupling efficiency and simplify the fabrication process it is possible for the grating and ridge to be made in a single fabrication step. This process is known as deeply etched lateral gratings and is the method used for the novel laser transmitter sources used in this chapter. This design looks applicable with InGaN/GaN lasers, specifically because of the low damage fabrication process for these devices. Fig.4.3.e) shows a less commonly used active corrugated metal layer.

DFB and DBR lasers are a well established technology with the first DFB laser demonstrated four decades ago. However, the first GaN-based DFB laser wasn't demonstrated until 1998 when Hofstetter *et al.* demonstrated the fabrication of an electrically injected InGaN/GaN-based DFB laser with a holographically defined 3rd order grating. The first DBR laser was demonstrated by Cho *et al.*, pulsed emission was achieved from an electrically injected InGaN/GaN-based DBR laser pulsed emission was achieved. The grating for this laser was created using dry etching of the p-AlGaN upper cladding. Similarly to the first DBR laser pulsed emission was demonstrated

by Schweizer *et al.* for the first DFB laser using a laterally coupled second order grating. Both of these devices used surface gratings which do not require epitaxial growth.

GaN DFB lasers could find uses in a number of applications. In relation to the topic of optical communications there are some advantages that single wavelength DFB lasers have over their FP counterparts. With limited bandwidth transmitters in the visible wavelength a viable option for increasing data rates is the use of WDM. Single wavelength DFB lasers offer high density of orthogonal channels in such a system. An additional advantage of DFB lasers is the possibility of reducing background interference with signals. Using a single DFB laser operating within the Fraunhofer solar lines would reduce interference from natural ambient light in free space VLC systems. In addition to these applications in optical communications there are other fields which would benefit from the development of DFB lasers. Atomic clocks would benefit from a narrow linewidth blue laser for atomic cooling transitions. Another use for these devices is accurate targeting of emission wavelength in fluorescence spectroscopy in medical diagnostics [110].

4.2 InGaN/GaN distributed feedback laser diodes with deeply etched sidewall gratings

With the Bragg length close to 400 nm it is difficult to fabricate first order sidewall gratings due to the feature size required (40 nm) and the high aspect ratios. Therefore, the devices used in this chapter use 3rd order gratings and the minimum feature size in this case is 120 nm.

The devices were fabricated at CST Global and were tested and measured at the University of Glasgow. Commercially available GaN laser grade material was used for fabrication of these DFB devices. The devices were fabricated using metal-organic vapour phase epitaxy (MOVPE). Three InGaN quantum wells were fabricated with GaN barriers, an Al0.2Ga0.8N electron blocking layer, GaN waveguide layers, Al0.06Ga0.94N cladding layers and a GaN cap layer.

Electron beam lithography was used to define the gratings and ridge patterns in ZEP 520 resist. The resolution of the EBL tool (Raith VB6 UHR) was 1 nm which allowed the grating to be fabricated with accurate resolution to produce the desired Bragg wavelength. The pattern was transferred into a 100 nm thick SiO_2 mask. The grating and ridge was produced with an STS multiplex tool used for inductively coupled plasma (ICP) etching. In order to fabricate steep grating walls which are close to being vertical a Cl_2/N_2 based ICP etch process with 300 W platen and 600 W coil power was used.

The electrical contacts were produced using Pd/Au on an Md doped p-GaN cap layer. Contact area definition was achieved using SiO_2 as an insulator. A backside metal stack of Ti/Pt/Au was deposited after the wafer was mechanically thinned and polished.

The etched grating of the DFB laser is shown in Fig.4.4 and Fig.4.5. The orientation of the grating is different from that of the DFB design in Fig.4.1. The device is laterally etched to

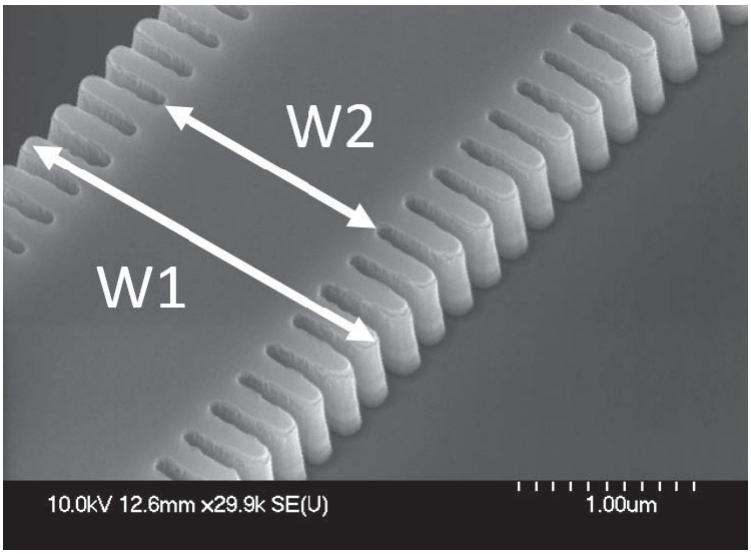

Figure 4.4: SEM micrograph of the as etched 3rd order grating [110].

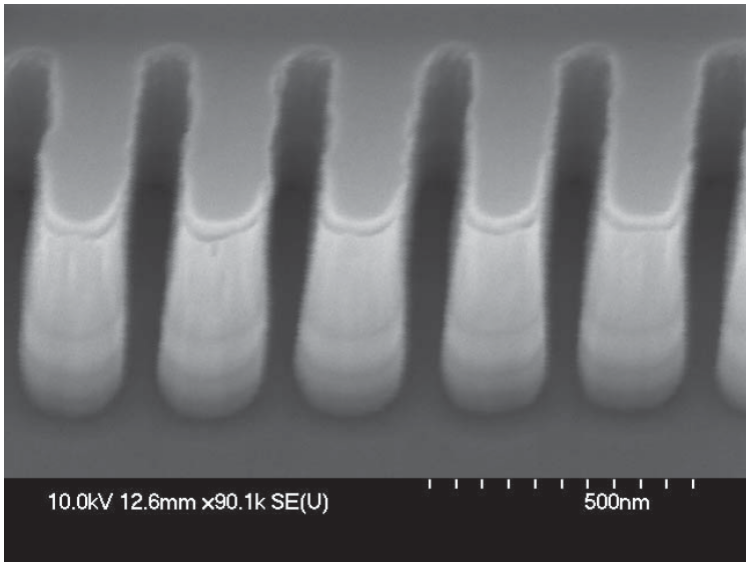

Figure 4.5: Micrograph looking towards the edge of the grating [110].

produce a sidewall grating on the ridge rather than the surface grating in Fig.4.1. The targeted duty cycle for the grating was 70-80%. However, the achieved duty cycle was approximately 50%. This discrepancy was mainly caused by over exposure during EBL but also process bias between resist and oxide line widths introduced during RIE contributes. When ICP etching is used there is an unavoidable sidewall angle as a result. In this case at the bottom of the ridge the duty cycle is approximately 80%. The bottom of the ridge is where the interaction with the optical mode is strongest. The following section presents the results from characterisation of the DFB laser used for optical transmission.

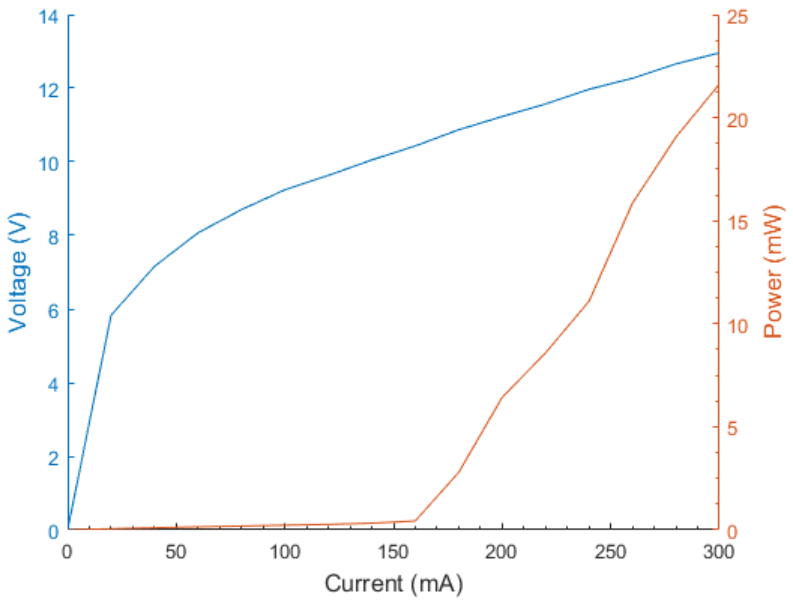

Figure 4.6: LVI curve of the DFB laser at 26°C.

4.3 DFB characterisation

This section describes the experimental method for characterising the novel DFB laser used in the optical communication system in section.4.4. The results of this characterisation are also expressed in this section with The LVI, emission spectra and bandwidth of the device presented.

4.3.1 Experiment, results and analysis

The experimental design for characterisation is similar to that described in section.3.3.1. The laser LVI was once again measured at a fixed temperature of 26^{o}C with the laser connected to a heatsink and temperature controlled as in section.3.3.1. This LVI curve was measured at the position of the photodetector after losses through transmission and the optical setup. The device was found to have a high threshold current, turn-on voltage and series resistance. When using sidewall etched gratings the p contact surface area is reduced and this increases series resistance. Fig.4.6 shows the LVI curve. The threshold current of the device is approximately 160 mA at a turn-on voltage of 10.5 V. The laser diode output was collected and collimated with a one inch focal length lens before being transmitted over a free space link of 10 cm. It was then focused onto a power meter (Newport 1918-R) with a second one inch focal length lens. After surpassing the threshold the power received at the power meter increased from 0.1 mW until a maximum reading of 21.62 mW.

The power meter was then replaced with a spectrometer, whilst the lens configuration was maintained, and the wavelength of the laser light was measured at varying drive currents. The results are exhibited in Fig.4.7. The laser spectral width is around 0.5 nm, this is limited by the

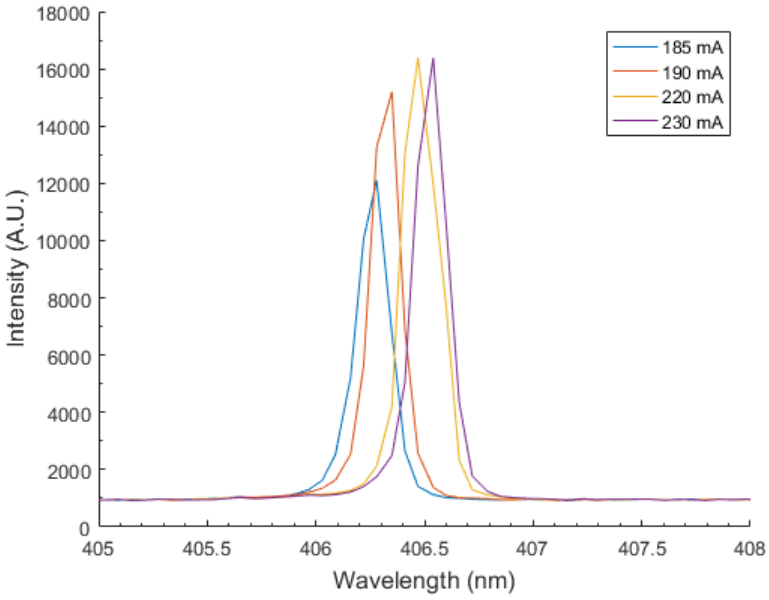

Figure 4.7: Emission spectra for DFB laser at drive currents from 185 *mA* to 230 *mA*.

resolution of the spectrometer. The spectra was measured at drive currents from 185 *mA* to 230 *mA*. As the drive current increases the emitted wavelength shifts towards a longer wavelength, this is known as Fabry-Perot shift. This is as a result of a change in the effective cavity length of the laser as is described in section.3.3.2.

The optical modulation bandwidth and the small signal frequency response were then measured as in section.3.3.1. With the only change being the Femto photorecevier was swapped for the Newport 818-BB-21A photoreceiver. The normalised small signal frequency response is shown in Fig.4.8. A 224 mV AC sinusoidal signal was combined with DC bias currents from 185 mA to 230 mA. The system is calibrated to compensate for the effects of the SMA cable and bias-T at the transmitter. As can be seen in Fig.4.8 the highest bandwidth was found at a drive current of 220 mA where the bandwidth is approximately 927 MHz.

The - 3 dB optical modulation bandwidth is shown as a function of drive current in Fig.4.9. It can be seen that the bandwidth increases with drive current until it reaches a maximum of 645 MHz at a drive current of 230 mA.

4.4 NRZ-OOK Communications

This section describes the optical communication using NRZ-OOK modulation format with the violet DFB laser as the source transmitter. The experimental design is described before the results are presented.

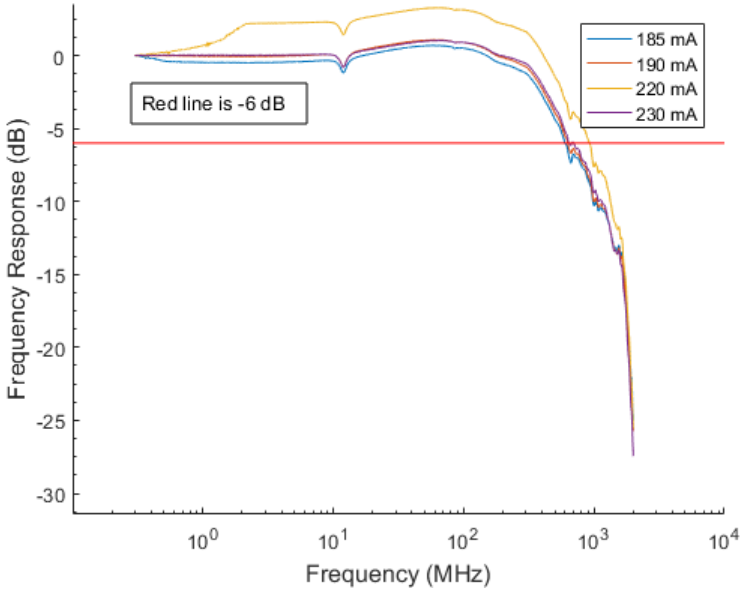

Figure 4.8: Frequency response of DFB laser at drive currents from 165 *mA* to 230 *mA*

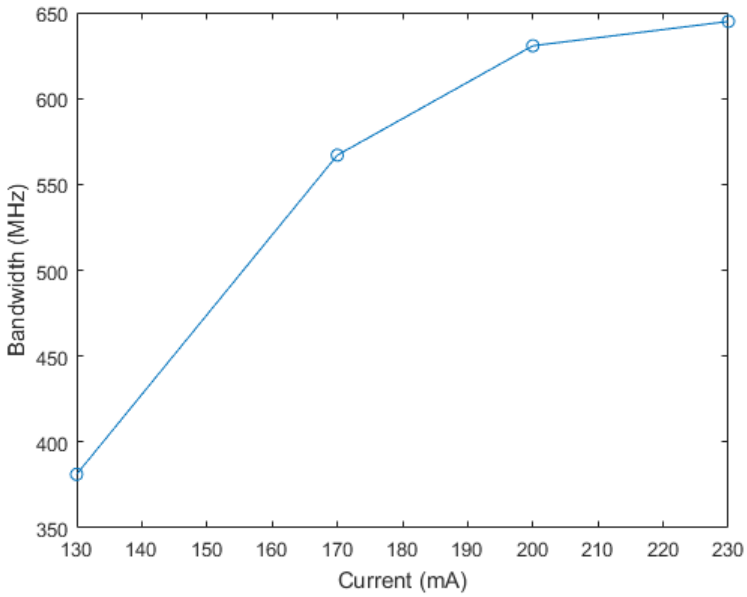

Figure 4.9: -3 dB optical modulation bandwidth for bias currents from 130 *mA* to 230 *mA*

4.4.1 Experiment, results and analysis

The experimental description of these measurements given in section.3.4 is applicable here. Eye diagrams were measured using an oscilloscope at different data rates as shown in Fig.4.10 and Fig.4.11. Fig.4.10 shows the eye diagram at 1.7 Gbit/s, with the error rate a multiple of 10^{-9}, at a drive current of 230 mA. Although the eye diagram is subject to high amplitude noise and time jitter the BER in this condition was still very low. Fig.4.11 shows the eye diagram at 1 Gbit/s, with the error rate at a multiple of 10^{-9}, at a drive current of 187 mA. At this lower data rate the

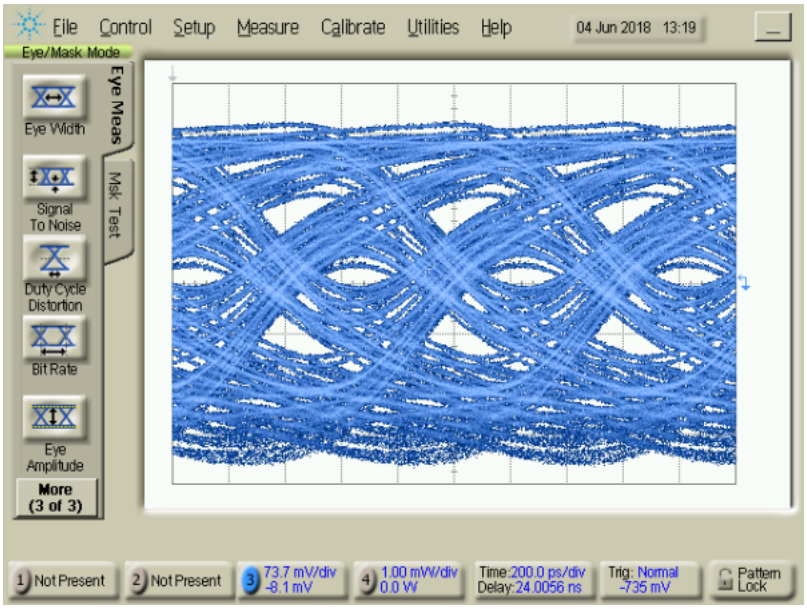

Figure 4.10: Eye diagrams showing error-free data transmission at 1.7 $Gbit/s$

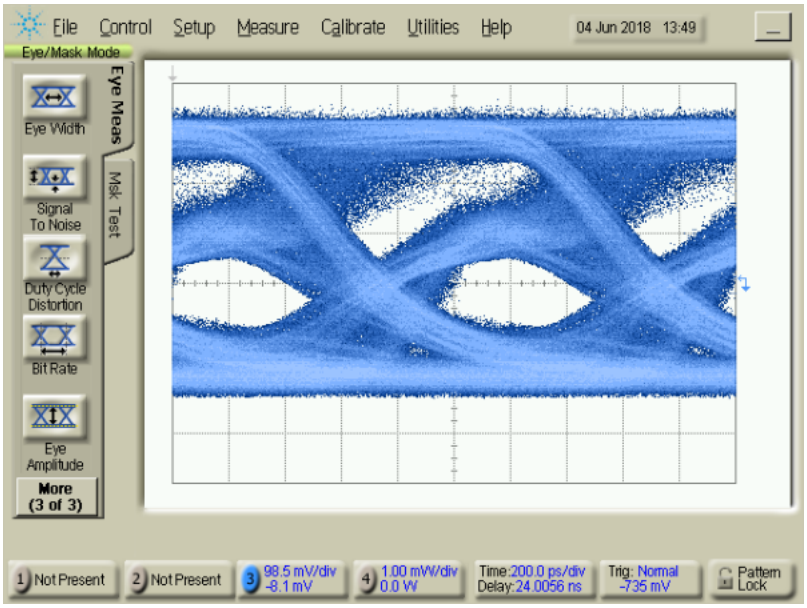

Figure 4.11: Eye diagrams showing error-free data transmission at 1 $Gbit/s$

eye diagram is more open. However, there is still significant undershoot visible at this data rate. Due to the reduce bit period at 1.7 Gbit/s the eye width is necessarily reduced when compared to the eye diagram at 1 Gbit/s. In addition to this the eye height is also reduced to around 25 mV.

The oscilloscope was then replaced with the BER detector. Bit error rate (BER) measurements of the NRZ-OOK system were measured using a BER detector. The maximum error free data rate as function of drive current was measured and can be seen in Fig.4.12. When measuring the BER the drive current and, therefore, optical power was varied to find the drive current at which the transmission was error free ($> 1x10^{-9}$) for each bit rate. This error free drive current

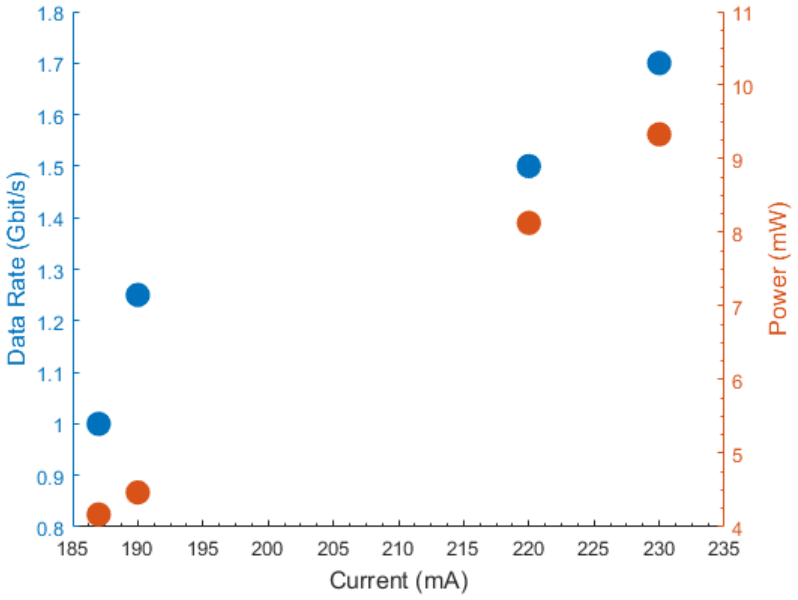

Figure 4.12: Left axis shows maximum error free data rate versus required current. Right axis shows the optical power corresponding to this drive current.

ranged from 187 mA to 230 mA for data rates from 1 Gbit/s to 1.7 Gbit/s. The required optical power for error rates less than $1x10^{-9}$ at 1, 1.25, 1.5, and 1.7 Gbit/s was 4.168, 4.467, 8.128 and 9.333 mW respectively, as shown in Fig.4.12.

4.4.2 Summary

In this chapter the data transmission capabilities of a novel DFB laser with deeply etched sidewall gratings were investigated. The device was characterised in terms of its LVI, frequency response, and bandwidth. The device was found to have subnanometer linewidth demonstrating the possibility of high density carrier WDM communications using such devices.

The laser was found to be capable of transmitting data error free up to 1.7 Gbit/s. The data transmission capabilities of such a device were unknown as this is the first GaN based DFB laser with deeply etched sidewall gratings emitting in the visible to be used in a communications system. This is slower than the maximum achievable data rate when using commercial lasers as is demonstrated in section.3.4. This is attributed to a combination of high threshold and high series resistance which was found to be greater than 10 ohms.

Chapter 5

OAM Underwater

This chapter presents the analysis of underwater effects on a set of 11-OAM modes propagating through slowly flowing water, at speeds similar to that found in oceanic conditions. A review of the published research on OAM communications and the effects of turbulence will be given first. After this the experimental design and methodology are discussed. The final section of the chapter details the results from the analysis of underwater effects on channel crosstalk and the potential causes of this.

5.1 OAM communications and turbulence effects

The use of OAM in a real world setting has already been demonstrated using radio waves [117]. Using an antenna disk with a stepped phase discontinuity Tamburini *et al.* were able to emit radio waves with l=1. It was shown that these waves were completely orthogonal and distinguishable from plane waves allowing for OAM multiplexing. Furthermore, Wang *et al.*, in 2012, transmitted at a data rate of 2.56 Tbit/s utilizing OAM multiplexing [118]. This data link was achieved by supplementing polarization multiplexing with OAM multiplexing. OAM multiplexing has been used in combination with polarization multiplexing and wavelength division multiplexing to demonstrate a system at 100 Tbit/s at wavelengths from 1536.34 nm to 568.5 nm [119]. In the visible range Gibson *et al.* used a HeNe laser to transmit information encoded as OAM states [120]. They were able to generate, transmit, receive and distinguish between eight OAM states over a distance of 15 m. This paper not only exhibited the multiplexing properties of OAM but also the increased security levels of OAM. It was shown that if the beam is intercepted away from its axis there will be inherent uncertainty about the form of the beam due to angular restriction and lateral offset. As is discussed in section.3.1 visible light communication underwater is a growing area of interest for its high bandwidth capabilities and low absorption coefficient underwater. Recently, Ren *et al.* performed underwater communication utilising OAM multiplexing to produce a system at 4 Gbit/s. They investigated various effects on the system from the underwater channel conditions such as scattering, water currents and

turbulence [121].

Due to the necessity of maintaining the beam's phase profile for successful distinction between OAM states, it is necessary to consider atmospheric turbulence and phase aberrations for transmission through free space. Work is being done to better understand these effects [122]. Optical waves propagating in free space encounter atmospheric turbulence effects. The astronomical society have studied these effects in depth to correct the resultant aberration in the images produced after propagation through turbulence [123]. The refractive index of the atmosphere is a function of temperature and humidity in air. As these vary randomly across a wave front this introduces a spatially dependent refractive index which leads to phase distortion across the optical beam wavefront [124]. Under certain circumstances, the phase fluctuations can be represented using Kolmogorov statistics and this is referred to as thin phase turbulence [125].

This phase deformation can be described by the phase structure function from Kolmogorov statistics. If we take two points in the wavefront r_1 and r_2 with each point having an associated phase fluctuation $\phi(r_1)$ and $\phi(r_2)$, respectively, then the phase function structure is described by $\langle[\phi(r_1)-\phi(r_2)]^2\rangle$ and the ensemble average of this must meet the requirement given in Eq.5.1.

$$\langle[\phi(r_1)-\phi(r_2)]^2\rangle = 6.88\|\frac{r_1-r_2}{r_0}\|^{\frac{5}{3}} \tag{5.1}$$

The r_0 term is the Fried parameter which is defined as the diameter of a circle over which the RMS wavefront aberration is equal to 1 rad. The ratio of the aperture system, D, to the Fried parameter, r_0, is used to characterise the effects of turbulence. For the case when $\frac{D}{r_0} < 1$ the limiting factor for the system resolution is the system aperture. The other limiting case where $\frac{D}{r_0} > 1$ the atmosphere limits the resolution.

Kolmogorov statistics can be used to predict the modal crosstalk of an OAM system subjected to atmospheric turbulence. Assuming thin phase turbulence, the power received in the mode adjacent to the transmitted mode can be calculated using Eq.5.2.

$$s_\Delta = \frac{1}{\pi}\int_0^1 \rho d\rho \int_0^{2\pi} d\theta e^{-3.44(\frac{D}{r_0})(\rho sin\frac{\theta}{2})^{\frac{5}{3}}} cos\Delta\theta \tag{5.2}$$

This theory has been confirmed for predicting modal crosstalk from atmospheric turbulence. Currently there is limited research on the effects of turbulence in water instead of the atmosphere [126]. The work in the rest of this chapter will show experimental measurement of modal crosstalk from underwater turbulence and effects.

5.2 Experimental design and system characterisation

The experiment consisted of a Tx and Rx placed 3 m apart within a water tank which was 15 m long and 0.3 m wide. The OAM modes were transmitted through water flowing at speeds similar to the gulf stream (1.3 ms^{-1}). The flow rate was set at three speeds and the modal

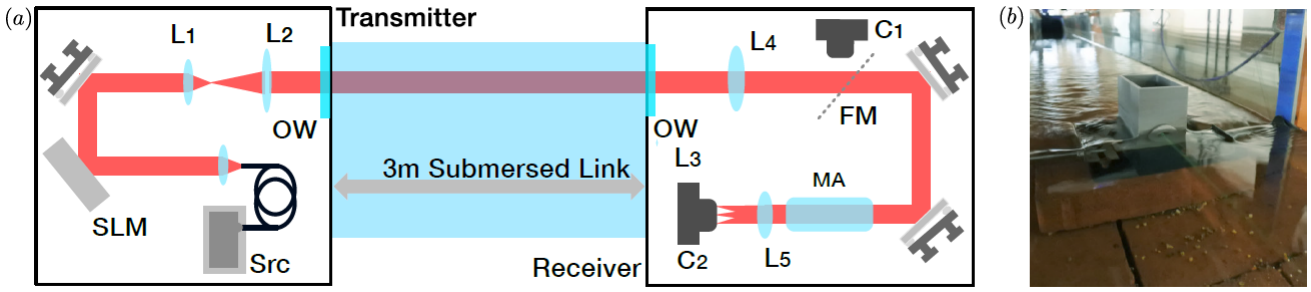

Figure 5.1: A coherent laser source (Src) with a wavelength of 535nm is coupled into a single mode fibre, and the output of the fibre is collimated by a 25mm lens. The collimated laser light is directed onto the surface of a spatial light modulator (SLM), which has a digital hologram encoded on it's optical surface to modulate the phase to the desired OAM mode. As the digital hologram is a diffraction grating, the first-order diffracted beam is spatially filtered at the focal plane of L1. A second lens, L2, of the same focal length is used to collimate the beam before propagation over the submersed link. To prevent modal degradation resulting from surface boundary effects, a Gorilla-glass optical window (OW) is used within a submersed 3D-printed water-proof enclosure, shown in (b). A field lens, L4, for focal length 500 mm is used to mitigate divergence accumulated over the submersed link. A flip mirror (FM) is utilised to allow for images of the received mode to be collected by C1. A combination of a mode analyser (MA) and a lens, L5, are used to transform the received OAM modes in discreet positions on a fast camera, C2.

crosstalk was measured at these three rates. The experimental layout is detailed in Fig.5.1.a). The beam from a Thorlab's laser diode (CPS532) was spatially filtered via a single mode fibre and used to illuminate Cambridge Correlator's SLM (SDE1024) with a Gaussian plane wave. Labview was used to control the l-forked hologram pattern generated on the SLM which was varied to give different OAM modes. By varying the refractive index across the liquid crystal display of the SLM it is possible to generate beams with different values of OAM. Lens L1 was used to focus the first order OAM mode through aperture A1 eliminating the other modes from transmission. L2 was used to collimate the mode before it is transmitted through 3 m of flowing tap water which is contained within a tank approximately 15 m long and 0.3 m wide. The floor of the tank is covered in gravel and bedrock similar to that of a coastal environment. Passing the mode through a water to air boundary would introduce distortion to the OAM mode due to the uneven surface of the water, therefore, the beam passes into a bespoke water proof enclosure which reflects the beam through an underwater glass boundary which introduces less distortion. This enclosure is shown in Fig.5.1.b).

Tip tilt aberration results from turbulence and mechanical stress on the system due to flowing water. The degree of tip tilt aberration is measured by transmitting a 0th order OAM mode (Gaussian mode) through the water and focussing it onto camera C1 without passing it through the mode analyser. The centre of mass (CoM) of the beam is then calculated at 16 μs intervals over a 10 s period and from this the tip tilt angle at the transmitter is calculated and shown in Fig.5.3.(a-c) for flow rates of 1.08, 1.38 and 2.02 ms^{-1}. This misalignment will contribute to

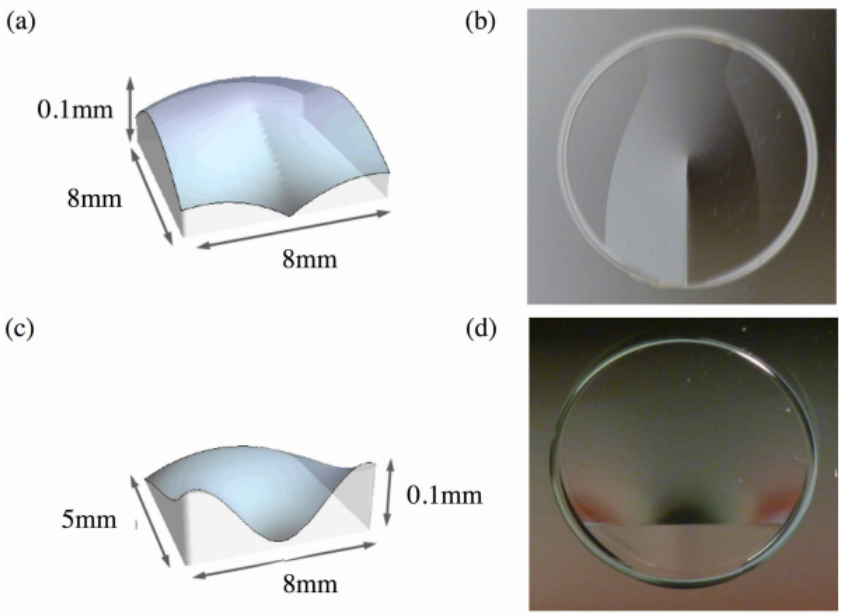

Figure 5.2: Height profiles (a,c) and photos (b,d) of refractive elements 1 (top) and 2 (bottom) of mode analyser. The aperture size is d = 8mm [130].

the observed modal crosstalk.

The beam at the receiver is analysed to measure the OAM spectrum. At the receiver lens L4 ensures the collimated beam is reflected onto a novel optical element called a mode analyser [127]. The mode analyser consists of two refreactive optical elements shown in Fig.5.2. The mode analyser is used with a convex lens to spatially separate the different OAM modes. The mode analyser takes an input OAM mode with an azimuthal phase gradient and transforms this into a plane wave with a transverse phase gradient which is then focussed by the convex lens to lateral positions at the focal plane dependent on the transverse phase gradient. A geometric transform can be performed if mapping of the input coordinates (x,y) to the output coordinates (u,v) is conformal as described in Eq.5.3.

$$\frac{\partial u(x,y)}{\partial y} = \frac{\partial v(x,y)}{\partial x} \tag{5.3}$$

the mode analyser uses a log polar transform where $v(x,y) = a arctan(\frac{y}{x})$ and $u(x,y) = -a ln(\frac{\sqrt{(x^2+y^2)}}{b})$ as this satisfies the requirement for conformality [128, 129]. The a term is a scaling parameter taking the value a$= \frac{d}{2\pi}$.

Therefore, the phase profile of the transforming optical element is given by Eq.5.4.

$$\phi_1(x,y) = \frac{2\pi a}{\lambda f}\left[y arctan\left(\frac{y}{x}\right) - x ln\left(\frac{\sqrt{x^2+y^2}}{b}\right) + x \right] \tag{5.4}$$

Using this optical element results in a phase distortion due to the varying optical path length.

It is therefore necessary to correct this distortion using a second optical element at the Fourier plane of the first image transforming element. The required phase distortion is calculated from the far field amplitude of a plane wave passed through the image transforming element and is given by Eq.5.5.

$$a_2(u,v) = exp\Big(i\phi_1(x,y) - i\frac{2\pi}{\lambda f}(xu+yv)\Big)\frac{2\pi}{\sqrt{\Big|\frac{\partial u}{\partial x}\frac{\partial v}{\partial y} - \Big(\frac{\partial u}{\partial y}\Big)^2\Big|}} \tag{5.5}$$

Therefore, there is a second optical element used to correct the amplitude distortion from the image transforming element. This phase correcting element is the inverse phase profile of a_2 and is given by Eq.5.6.

$$\phi_2(u,v) = -\frac{2\pi ab}{\lambda f}exp\Big(-\frac{u}{a}\Big)cos\Big(\frac{v}{a}\Big) \tag{5.6}$$

Where u and v are the cartesian coordinates in the Fourier plane of the first element. After these steps focussing the output plane waves generated from different OAM modes gives a lateral distance described by Eq.5.7.

$$t_l = \frac{\lambda f}{d}l \tag{5.7}$$

Matlab was used to process the frames from camera C2. Eleven equally sized regions were selected, with each region's pixel values summed to measure the power received in each different OAM order. The modes were l =+5 to l =-5 and the crosstalk is shown in Fig.5.3.(e-g) for when the transmitted mode was l =2. The power measured in each region is an average of the power over a 10 s window. Fig.5.4 shows the power matrix which shows the channel crosstalk for all input modes.

Due to the use of the mode sorter in this experiment it was possible to analyse the temporal power variance in each mode. This was measured for mode $l = 2$ in free space and at the fastest flow rate of 2.02 ms^{-1} shown in Fig.5.6. This figure also shows the variation for the higher order mode of $l = 5$. This measurement can give an indication of mechanical movement between the transmitter and the receiver.

As light propagates through the water it encounters particulates in the system causing absorption and scattering reducing the overall system power. The relative power fluctuation was measured over a 10 s window and is plotted for the three flow rates shown in Fig.5.7 along with the scintillation index.

5.3 Tip tilt aberration and modal crosstalk

Fig.5.3(a-c) shows the deviation in CoM for the three flow rates 1.08, 1.32 and 2.02 ms^{-1}.The CoM for each frame is calculated and the deviation from the mean CoM of all the frames is

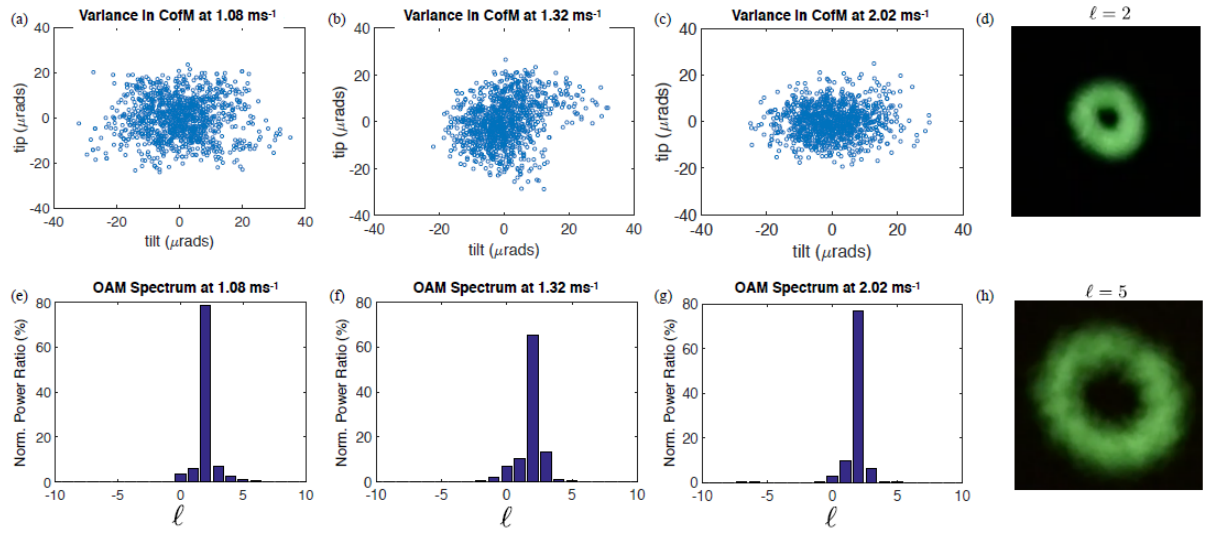

Figure 5.3: (a-c) A centroid measurement was calculated from each recorded frame, and plotted as a scatter plot to determine tip tilt aberration. Images of the received optical modes for optical modes (d) l = 2 and (h) l = 5. (e-g) For each flow rate the modal crosstalk can be determined by the intensity profile on camera C2. The measured intensity is averaged over 1200 frames for each speed respectively. The transmitted mode was l = 2.

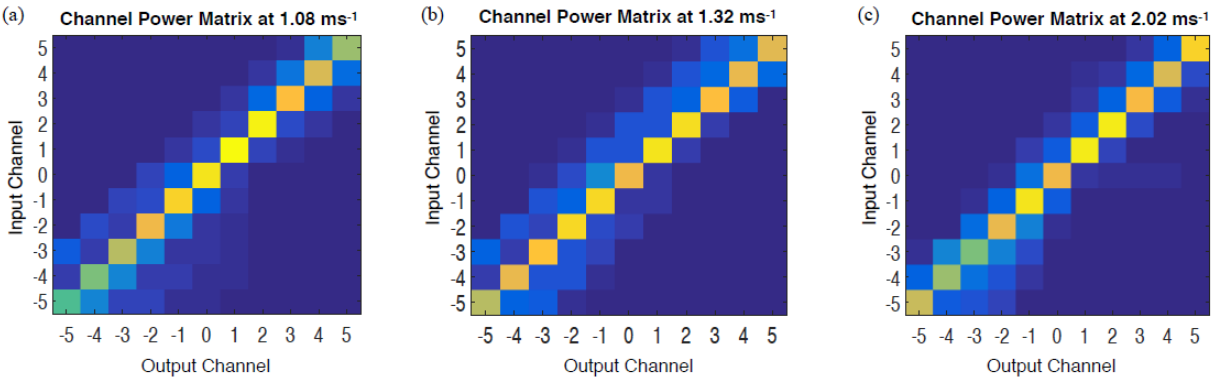

Figure 5.4: A crosstalk matrix can be generated to visualise the expected crosstalk for each of the 11 OAM channels for flow rates 1.08 ms^{-1}, 1.32 ms^{-1} and 2.02 ms^{-1} respectively. The measured crosstalk is the averaged modal crosstalk over a 10 s measurement window. Hence, crosstalk arising from tip-tilt aberrations and static system aberrations both contribute to the crosstalk measured.

calculated and presented as the angular tip tilt variation at the transmitter. The CoM deviation in the x direction is given by Eq.5.8. The CoM deviation in the y direction is given by Eq.5.9.

$$C_x = \sum_{i=1}^{N} \frac{M_i x_i}{mass} \tag{5.8}$$

$$C_y = \sum_{i=1}^{N} \frac{M_i y_i}{mass} \tag{5.9}$$

Where M_i is is the mass at position x_i and position y_i in each formula. Given the variation in position and length of propagation the CoM variance can be represented in rads using Pythagaras theorem to convert the variance. The CoM showed little variation over the three speeds with a standard deviation of 9.92 microrads, 8.89 microrads and 7.88 microrads at 1.08 m/s, 1.38 m/s and 2.02 m/s respectively. Therefore, from the consistent standard deviation of CoM we can assume a consistent value for tip tilt turbulence regardless of longitudinal flow rate. Fig.5.3.d and Fig.5.3.h show the beam profile for modes l=2 and l=5 after propagation through the water.

After the CoM variance was measured the modal crosstalk at the three flow rates was measured when the transmitted mode was l=2. The results are shown in Fig.5.3(e-g). There is crosstalk inherent to the system from the mode sorter and the mechanical instability of the system. The mechanical instability contributes to tip tilt aberration and produces crosstalk into other OAM modes. Pure OAM states are defined relative to the z axis which is normal to the plane in which the azimuthal phase gradient exists where the complex amplitude of the pure mode is $exp[il\phi]$. When measured using a different z axis the beam becomes a superposition of different OAM modes. OAM modes are Laugerre Gaussian modes described using cartesian coordinates by Eq.5.10.

$$\psi_{l,p}(x,y) = C_{lp}\left(\frac{2(x^2+y^2)}{w^2}\right)^{\frac{|l|}{2}} \; L_p^{|l|}\left(\frac{2(x^2+y^2)}{w^2}\right) \; x \; exp\left[\frac{-(x^2+y^2)}{w^2}\right] \; exp[ilatan2(x,y)] \quad (5.10)$$

Any beam cross section can be described Eq.5.11 using Braket notation.

$$|\psi\rangle = \sum_{l=-\infty}^{\infty} \sum_{p=0}^{\infty} |l_p\rangle\langle l_p|\psi\rangle \quad (5.11)$$

Where $\psi_{l,p} = |l_p\rangle$ and $|\psi\rangle = \psi(x,y)$ When the mode is misaligned as in Fig.5.5 the mode is described by Eq.5.12.

$$\psi(x,y) = \psi_{l,p}(x-\Delta x, y-\Delta y) \; exp\left[i\frac{2\pi}{\lambda} \; (xsin\alpha + ysin\beta)\right] \quad (5.12)$$

Where $\Delta x, \Delta y, \alpha$ and β are the beam offset and angle of incidence with the plane at right angles to the measurement axis. The OAM spectrum of this misaligned mode is described by Eq.5.13.

$$P_l = \sum_{p=0}^{\infty} P_{l,p} = \sum_{p=0}^{\infty} |\langle l_p|\psi\rangle|^2 \quad (5.13)$$

Where $|\psi\rangle$ is the beam cross section $\psi(x,y)$ given in braket notation and is given by Eq.5.11. Where $|l_p\rangle = \psi_{l,p}$ and is a pure mode cross section.

The consistent crosstalk across each flow rate indicates that the inherent system factors are the main contributor to the modal crosstalk as oppose to effects of underwater turbulence.

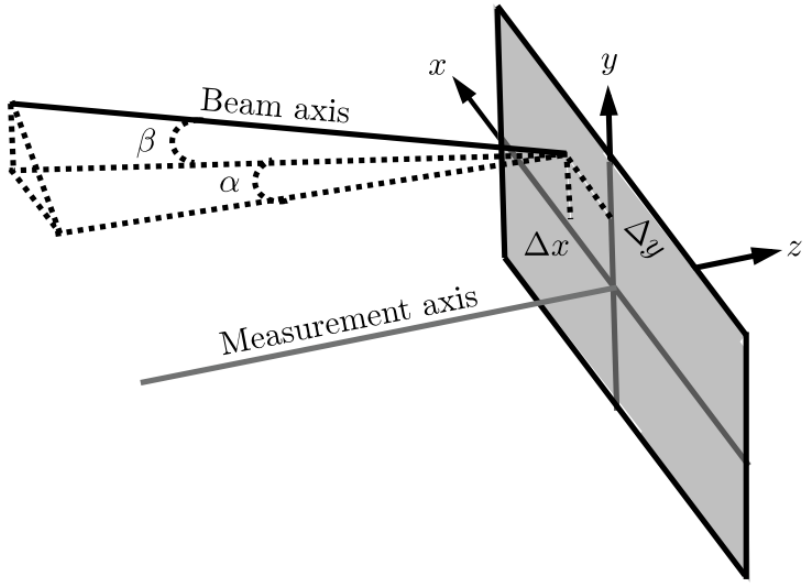

Figure 5.5: Relationship between beam axis and measurement axis. The beam axis is tilted with respect to the measurement axis by the angles α and β in the (x,z) and (y,z) planes, respectively. In the plane z = 0, the beam axis is offset with respect to the measurement axis in the x direction by Δx and in the y direction by Δy [131].

Fig.5.4 shows the crosstalk for all 11 input modes (l=-5 to l=+5) at three flow rates. Again from the matrix we can see that the modal crosstalk is consistent across flow rate for all the transmitted modes. The following section examines variations in modal crosstalk and power over time.

5.4 Temporal analysis of modal crosstalk and power variation

Fig.5.6 shows the crosstalk variation for each frame and how it varies with time. Looking at how the crosstalk varies frame to frame can give a better understanding of stability. The instantaneous crosstalk was measured for l=2 without flowing water and for l=2 and l=5 at 2.02 ms^{-1}. The temporal variance in crosstalk was greatest without water flowing in the channel. This suggests that when water is present this reduces movement of the transmitter and receiver from mechanical effects such as tank vibration. Therefore, one of the main issues when compensating for crosstalk in an underwater OAM system will be the mitigation of tip tilt aberration as a result of mechanical instabilities.

Fig.5.7(a-c) shows the frame to frame power variation over 10 s. The power variation gives insight into the effects from floating particulates in the water reducing the optical power by scattering and absorption. The scintillation index allows for analysis of the temporal power fluctuation and is given by Eq.5.14.

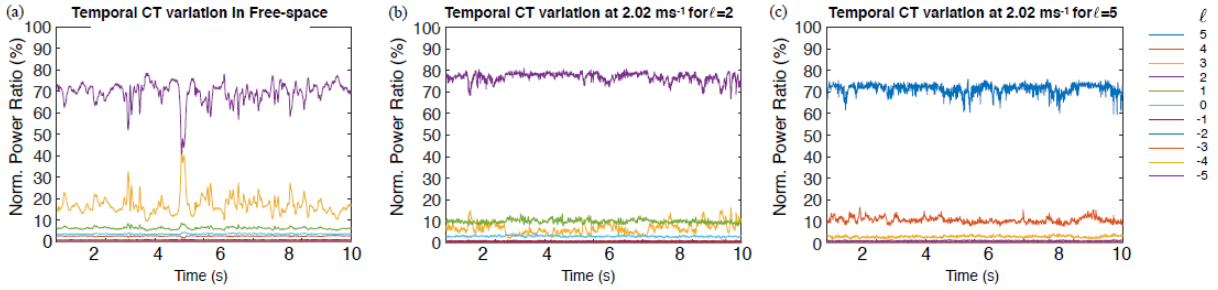

Figure 5.6: System stability is an important consideration. To investigate the stability of the submersed link we consider the channel crosstalk measured at each individual frame. Each frame has 16 μs exposure time. It can be seen that the free-space link (a) has greater frame-by-frame variation in modal crosstalk as compared to a link that has water flowing at 2.02 ms^{-1} (b). This variation may be due to increased mechanical vibration. We further consider an OAM mode with l = 5, showing the stability is broadly similar for the higher order modes.

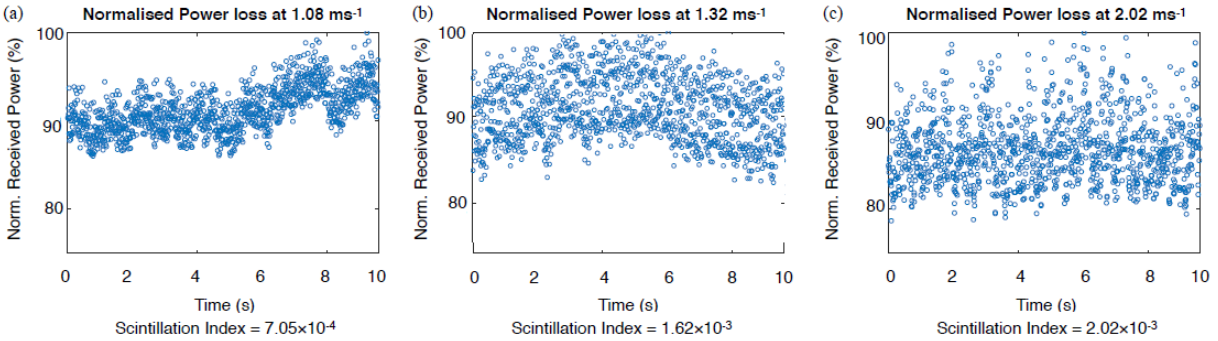

Figure 5.7: Optical scattering from particulates are a concern with a submersed optical link. These particles move with the fluid flow and can result in a variance in measured crosstalk and power loss. The normalised power is considered frame-by-frame for flow speeds 1.08 ms^{-1}, 1.32 ms^{-1} and 2.02 ms^{-1}.

$$\sigma_I^2 = \frac{< I^2 > - < I >^2}{< I^2 >} \tag{5.14}$$

.

It can be seen that the scintillation index increases with flow rate. As the flow rate increases the rate at which the particulates pass through the propagating beam increases. This leads to a higher fluctuation in power and therefore a higher scintillation index.

5.4.1 Summary

In conclusion we have experimentally measured the crosstalk between OAM modes propagating through slow moving water. Our initial results indicate that tip-tilt aberration is a considerable contributing factor to the expected inter-channel crosstalk. In coastal conditions, we expect there to be little modal degradation arising from phase aberrations. However, we expect mechanical

stability of the optical system to be a central source of modal crosstalk. In this chapter a review of communication systems demonstrating OAM multiplexing was given. The modal crosstalk and causes of crosstalk were analysed also. The modal crosstalk was not found to vary significantly as a result of the water flow rate or water particulates suspended in the water from the coastal gravel and bedrock. The crosstalk that was apparent in the system was as a result of inherent system factors such as mechanical vibration. Therefore, compensating for mechanical vibrations would make OAM a viable option for underwater multiplexing in VLC.

Chapter 6

Conclusions

This thesis presented novel free space optical communication systems using different modulation formats, multiplexing schemes and transmitter sources. The optical devices used as system transmitter sources were either μ - LEDs or lasers emitting radiation in the visible portion of the electromagnetic spectrum. All systems were found to have high speed data capabilities in the region of gigabits and would be useful in different applications of visible light communications.

Chapter 1 provided a brief history of the LED and major milestones in its development towards contemporary technology. In the past decades advances in the growth of AlInGaN materials has brought us to the point were solid state lighting is highly efficient and in the coming decades will replace current incandescent and fluorescent lighting infrastructure. This is despite the fact that the reasons for efficiency droop and high number of dislocations in InGaN LEDs is not properly understood. A review of the fundamental operation of LEDs was also given. Next in this chapter was a short history of the laser diode ranging from the first optically pumped ruby rod laser to the modern GaN laser diode which could be the basis for future underwater optical communications. A review of how laser operation contrasts to that of LEDs was given. Finally a brief theoretical introduction and historical review of the advanced multiplexing techniques of OFDM and OAM were given.

Chapter 2 began with an introduction to LED applications in visible light communications. Particular emphasis was given to the state of the art and recent achievements with GaN based μ - LEDs. A brief description of the layout and fabrication process for novel μ - LED arrays used as transmitter sources was presented. These devices have small active areas and are designed in an array to match optical fibre arrays. In this chapter the first VLC system was presented using a violet μ - LED. The implementation of OFDM using IM/DD for VLC systems was described. The device was first characterised by measurement of LVI, emission spectra, frequency response and bandwidth before being modulated by the QAM-based OFDM signal in the VLC system. The key result of this research was the demonstration of the record data rate for a violet LED system at 7.91 Gbit/s. This device was shown to be the highest bandwidth LED in the violet wavelength range at 655 MHz.

Chapter 3 introduced the results of moving to a laser as the source transmitter for VLC. A review of the state of the art for laser based VLC was given at the start of this chapter. A discussion of the different environments where lasers may yet find commercial applications such as FSO systems or underwater communication systems was provided in the review. Interests in lasers as sources for VLC stems from some of the advantages associated with using lasers instead of LEDs. Specifically, lasers have higher bandwidth and efficiency than LEDs and the mechanisms for this were explained in Chapter 3. The laser source used for the experiments in this chapter was the Osram PL450B. The results from characterisation of this device were presented before the results of deploying the device in a VLC system were presented. The initial system utilized NRZ OOK as the modulation format achieving 4.7 Gbit/s. The merits of QAM modulation, OFDM and adaptive bit loading were shown in this chapter as the data rate increased to 15 Gbit/s for the same device.

Chapter 4 discussed the operation of DFB lasers and how they achieve narrow linewidth emission. The various methods of fabricating a grating in the DFB were introduced. Then the characterisation of a novel InGaN distributed feedback laser with deeply etched sidewall gratings was presented. The device was also modulated using a NRZ OOK signal and the system achieved error free transmission at 1.7 Gbit/s. These devices were shown to have subnanometer linewidths. With a narrow emission spectrum such lasers could be used for high density WDM systems. Additionally, with measured linewdiths as low as 0.5 nm these lasers could operate in the Fraunofer lines where the absorption linewidths can be several nm. This would reduce ambient lighting interference.

Chapter 5 introduced the concept of turbulence and the OAM modal crosstalk that is induced by turbulence. A review of communication systems demonstrating OAM multiplexing was given. The modal crosstalk and causes of crosstalk were analysed in this chapter. The modal crosstalk was not found to vary significantly as a result of the water flow rate or water particulates suspended in the water from the coastal gravel and bedrock. The crosstalk that was apparent in the system was as a result of inherent system factors such as mechanical vibration. Therefore, compensating for mechanical vibrations would make OAM a viable option for underwater multiplexing in VLC.

6.0.1 Future work

As a result of the research in this thesis a 6 month feasibility study to develop an early system underwater communication prototype is under way at the University of Glasgow (Undercomm Phase 1). So far a TRL4 prototype has been developed using the Osram PL450B laser, characterised in this thesis, as the transmitter source. The laser acts as a direct optical link at 450 nm in a gigabit ethernet system.

The InGaN DFB described in Chapter 4 was fabricated using a process to produce deeply etched sidewall gratings which do not require the complex overgrowth steps required for over-

grown DFBs which can introduce higher levels of non radiative recombination from threading dislocations caused by surface defects from interrupting the growth process. Sidewall etched DFB lasers do not risk damaging the p contact, unlike surface etched devices. The InGaN DFB laser used in this thesis was shown to have a subnanometer linewidth. Work is underway to lower the threshold current of these devices and reduce the series resistance. A novel application of these devices would be a background immune optical communication system. Taking an optical communication system similar to the one described in chapter 2 with added background interference and filtering would be an experimental demonstration of the benefits of a narrow linewidth DFB laser. Solar irradiance has been found to increase the BER in VLC system or reduce the system data transmission capacity [132]. One method of alleviating this issue would be operation of VLC systems at Fraunhofer solar lines. for example the Fraunhofer line at 396 nm is 1.5 nm wide and therefore the linewidth of the DFB in this thesis is narrow enough. Further developments are required to reliably produce lasers with accurate wavelength output. Development of a DFB laser at one of these wavelengths would allow a demonstration of a VLC system which is highly immune to ambient solar light. In addition to exploring background immunity of these narrow linewidth lasers further work could show the achievable density for WDM. Narrow linewidth devices allow for high density of carriers in WDM systems which can be separated by filtering. Further work could explore the accuracy requirements for filters in terms of their transmission versus wavelength characteristics.

Chapter 5 investigated the effects of water flow rate, coastal condition bedrock and mechanical stability on OAM modal crosstalk underwater. This is a new area of research and much research has still to be done for the technology to mature. In Chapter 5 it was shown that the turbulence effects from flowing water were minimal when compared to the crosstalk as a result of tip tilt aberration through mechanical instability. As orthogonality of OAM modes is dependent upon coaxial propagation of modes, precise alignment between the transmitter and receiver is required . Therefore it is likely that mitigation techniques such as adaptive optics compensation will be required to reduce modal crosstalk. Additionally, this work has not considered effects of thermal gradients in water which will introduce further crosstalk. This chapter explored crosstalk for a horizontally propagating beam. In oceanic and other water types vertical propagation of OAM modes will be greatly affected by variation in temperature across the link as the temperature of water is more variant vertically than horizontally in most scenarios. Therefore, vertical propagation of OAM modes should be investigated and will have a different set of issues to overcome.

Bibliography

[1] H. J. Round, "A note on carborundum," in *Semiconductor Devices: Pioneering Papers*. World Scientific, 1991, pp. 879–879.

[2] H. K. Henisch and R. Roy, *Silicon Carbide: Proceedings of the International Conference on Silicon Carbide, University Park, Pennsylvania, October 20-23, 1968*. Elsevier, 2013.

[3] R. M. Potter, J. M. Blank, and A. Addamiano, "Silicon Carbide Light-Emitting Diodes," *Journal of Applied Physics*, vol. 40, no. 5, pp. 2253–2257, 1969.

[4] N. Holonyak Jr and S. Bevacqua, "Coherent (visible) light emission from Ga (As1- xPx) junctions," *Applied Physics Letters*, vol. 1, no. 4, pp. 82–83, 1962.

[5] N. Holonyak Jr, C. Nuese, M. Sirkis, and G. Stillman, "Effect of donor impurities on the direct-indirect transition in ga (as1-xpx)," *Applied Physics Letters*, vol. 8, pp. 83–85, 1966.

[6] S. Ishimatsu and Y. Okuno, "High efficiency GaAlAs LED," *Optoelectron. Devices Technol*, vol. 4, pp. 21–32, 1989.

[7] P. Maruska, H and J. Tietjen, "The preparation and properties of Vapor-Deposited single-crystal-line GaN," *Applied Physics Letters*, vol. 15, no. 10, pp. 327–329, 1969.

[8] J. Pankove, E. Miller, and J. Berkeyheiser, "Electroluminescence in GaN," in *Luminescence of Crystals, Molecules, and Solutions*. Springer, 1973, pp. 426–430.

[9] H. Amano, M. Kito, K. Hiramatsu, and I. Akasaki, "P-type conduction in Mg-doped GaN treated with low-energy electron beam irradiation (LEEBI)," *Japanese Journal of Applied Physics*, vol. 28, no. 12A, p. L2112, 1989.

[10] S. Nakamura, N. Iwasa, and M. Senoh, "Method of manufacturing p-type compound semiconductor," Apr. 26 1994, US Patent 5,306,662.

[11] E. Schubert, W. Grieshaber, and I. Goepfert, "Enhancement of deep acceptor activation in semiconductors by superlattice doping," *Applied physics letters*, vol. 69, no. 24, pp. 3737–3739, 1996.

[12] S. Nakamura, M. Senoh, and T. Mukai, "P-GaN/N-InGaN/N-GaN double-heterostructure blue-light-emitting diodes," *Japanese Journal of Applied Physics*, vol. 32, no. 1A, p. L8, 1993.

[13] ——, "High-power InGaN/GaN double-heterostructure violet light emitting diodes," *Applied Physics Letters*, vol. 62, no. 19, pp. 2390–2392, 1993.

[14] S. Nakamura, T. Mukai, and M. Senoh, "Candela-class high-brightness InGaN/AlGaN double-heterostructure blue-light-emitting diodes," *Applied Physics Letters*, vol. 64, no. 13, pp. 1687–1689, 1994.

[15] S. Nakamura, "Nobel Lecture: Background story of the invention of efficient blue InGaN light emitting diodes," *Reviews of Modern Physics*, vol. 87, no. 4, p. 1139, 2015.

[16] E. F. Schubert, *Light Emitting Diodes*, 2006.

[17] S. Chichibu, T. Azuhata, T. Sota, and S. Nakamura, "Spontaneous emission of localized excitons in InGaN single and multiquantum well structures," *Applied Physics Letters*, vol. 69, no. 27, pp. 4188–4190, 1996.

[18] S. Nakamura, "The roles of structural imperfections in InGaN-based blue light-emitting diodes and laser diodes," *Science*, vol. 281, no. 5379, pp. 956–961, 1998.

[19] S. Hussain, "Structural and optical characterization of green-yellow light emitting devices with high indium concentrated (in, ga) n quantum wells," Ph.D. dissertation, Université Nice Sophia Antipolis, 2014.

[20] S. Nakamura, S. Pearton, and G. Fasol, *The blue laser diode: the complete story*. Springer Science & Business Media, 2013.

[21] D. O'brien, G. Parry, and P. Stavrinou, "Optical hotspots speed up wireless communication," *Nature Photonics*, vol. 1, no. 5, pp. 245–247, 2007.

[22] https://steemit.com/steemstem/@whileponderin/electrons-holes-and-electricity, accessed: 2017-10-04.

[23] http://pediaa.com/difference-between-p-type-and-n-type-semiconductor/, accessed: 2017-10-04.

[24] M. Fukuda, *Optical Semiconductor Devices*, 1999.

[25] https://physics.stackexchange.com/q/175485, accessed: 2017-10-04.

[26] A. Einstein, "On the Quantum Theory of Radiation," *The Old Quantum Theory: The Commonwealth and International Library: Selected Readings in Physics*, p. 167, 2016.

[27] J. P. Gordon, H. J. Zeiger, and C. H. Townes, "Molecular Microwave Oscillator and New Hyperfine Structure in the Microwave Spectrum of N H 3," *Physical Review*, vol. 95, no. 1, p. 282, 1954.

[28] T. H. Maiman, "Stimulated optical radiation in ruby," *nature*, vol. 187, no. 4736, pp. 493–494, 1960.

[29] A. Javan, W. R. Bennett Jr, and D. R. Herriott, "Population inversion and continuous optical maser oscillation in a gas discharge containing a He-Ne mixture," *Physical Review Letters*, vol. 6, no. 3, p. 106, 1961.

[30] A. White and J. Rigden, "Continuous gas maser operation in visible," *Proceedings of the Institute of Radio Engineers*, vol. 50, no. 7, p. 1697, 1962.

[31] L. Johnson and K. Nassau, "Infrared fluorescence and stimulated emission of Nd3+ in CaWO4," *Proc. Ire*, vol. 49, no. 11, pp. 1704–1705, 1961.

[32] L. Johnson, G. Boyd, K. Nassau, and R. Soden, "Continuous operation of a solid-state optical maser," *Physical Review*, vol. 126, no. 4, p. 1406, 1962.

[33] R. Keyes and T. Quist, "Recombination radiation emitted by gallium arsenide," *Proceedings of the Institute of Radio Engineers*, vol. 50, no. 8, p. 1822, 1962.

[34] R. N. Hall, G. E. Fenner, J. Kingsley, T. Soltys, and R. Carlson, "Coherent light emission from GaAs junctions," *Physical Review Letters*, vol. 9, no. 9, p. 366, 1962.

[35] I. Hayashi, M. Panish, P. Foy, and S. Sumski, "Junction lasers which operate continuously at room temperature," *Applied Physics Letters*, vol. 17, no. 3, pp. 109–111, 1970.

[36] S. Nakamura, M. Senoh, S.-i. Nagahama, N. Iwasa, T. Yamada, T. Matsushita, Y. Sugimoto, and H. Kiyoku, "Room-temperature continuous-wave operation of InGaN multi-quantum-well structure laser diodes," *Applied Physics Letters*, vol. 69, no. 26, pp. 4056–4058, 1996.

[37] A. Neumann, J. Wierer, W. Davis, Y. Ohno, S. Brueck, and J. Tsao, "Four-color laser white illuminant demonstrating high color-rendering quality," *Optics express*, vol. 19, no. 104, pp. A982–A990, 2011.

[38] K. A. Denault, M. Cantore, S. Nakamura, S. P. DenBaars, and R. Seshadri, "Efficient and stable laser-driven white lighting," *AIP Advances*, vol. 3, no. 7, p. 072107, 2013.

[39] C. Koester and C. J. Campbell, "The first clinical application of the laser," *Lasers in Ophthalmology: Basic, Diagnostic, and Surgical Aspects: A Review*, pp. 115–117, 2003.

[40] e. P. Franken, A. E. Hill, C. e. Peters, and G. Weinreich, "Generation of optical harmonics," *Physical Review Letters*, vol. 7, no. 4, p. 118, 1961.

[41] A. K. Maini, *Laser and Optoelectronics: Fundamentals, Devices and Applications*, 2013.

[42] https://www.photonics.com/Articles/Semiconductor_Lasers_An_Overview_of_Commercial/a25099, accessed: 2017-10-04.

[43] T. Matniyaz, "Free-space npr mode locked erbrium doped fiber laser based frequency comb for optical frequency measurement," *arXiv preprint arXiv:1802.10183*, 2018.

[44] P. Winzer, "Making spatial multiplexing a reality," *ature Photonics*, vol. 8, no. 5, p. 345, 2014.

[45] https://en.wikipedia.org/wiki/Wavelength-division_multiplexing, accessed: 2017-10-04.

[46] http://blog.teledynelecroy.com/2016/02/the-fundamentals-of-coherent-signals.html, accessed: 2017-10-04.

[47] https://www.labvolt.com/downloads/39866_F0.pdf, accessed: 2017-10-04.

[48] S. Randel, R. Ryf, A. Sierra, P. J. Winzer, A. H. Gnauck, C. A. Bolle, R.-J. Essiambre, D. W. Peckham, A. McCurdy, and R. Lingle, "6$\times$ 56-Gb/s mode-division multiplexed transmission over 33-km few-mode fiber enabled by 6$\times$ 6 MIMO equalization," *Optics Express*, vol. 19, no. 17, pp. 16 697–16 707, 2011.

[49] R. W. Chang, "Synthesis of Band-Limited Orthogonal Signals for Multichannel Data Transmission," *Bell Labs Technical Journal*, vol. 45, no. 10, pp. 1775–1796, 1966.

[50] S. Weinstein and P. Ebert, "Data transmission by frequency-division multiplexing using the discrete Fourier transform," *IEEE transactions on Communication Technology*, vol. 19, no. 5, pp. 628–634, 1971.

[51] A. Peled and A. Ruiz, "Frequency domain data transmission using reduced computational complexity algorithms," in *Acoustics, Speech, and Signal Processing, IEEE International Conference on ICASSP'80.*, vol. 5. IEEE, 1980, pp. 964–967.

[52] B. Hirosaki, "An orthogonally multiplexed QAM system using the discrete Fourier transform," *IEEE Transactions on Communications*, vol. 29, no. 7, pp. 982–989, 1981.

[53] L. Cimini, "Analysis and simulation of a digital mobile channel using orthogonal frequency division multiplexing," *IEEE transactions on communications*, vol. 33, no. 7, pp. 665–675, 1985.

[54] I. Kalet, "The multitone channel," *IEEE transactions on communications*, vol. 37, no. 2, pp. 119–124, 1989.

[55] W. Shieh and I. Djordjevic, *OFDM for optical communications*. Academic Press, 2009.

[56] J. C. Maxwell, "A dynamical theory of the electromagnetic field," *Philosophical transactions of the Royal Society of London*, vol. 155, pp. 459–512, 1865.

[57] J. Poynting, "The wave motion of a revolving shaft, and a suggestion as to the angular momentum in a beam of circularly polarised light," *Proceedings of the Royal Society of London. Series A, Containing Papers of a Mathematical and Physical Character*, vol. 82, no. 557, pp. 560–567, 1909.

[58] R. A. Beth, "Mechanical detection and measurement of the angular momentum of light," *Physical Review*, vol. 50, no. 2, p. 115, 1936.

[59] C. Darwin, "Notes on the theory of radiation," *Proceedings of the Royal Society of London. Series A, Containing Papers of a Mathematical and Physical Character*, vol. 136, no. 829, pp. 36–52, 1932.

[60] L. Allen, M. W. Beijersbergen, R. Spreeuw, and J. Woerdman, "Orbital angular momentum of light and the transformation of Laguerre-Gaussian laser modes," *Physical Review A*, vol. 45, no. 11, p. 8185, 1992.

[61] M. P. Lavery, D. J. Robertson, A. Sponselli, J. Courtial, N. K. Steinhoff, G. A. Tyler, A. E. Willner, and M. J. Padgett, "Efficient measurement of an optical orbital-angular-momentum spectrum comprising more than 50 states," *New Journal of Physics*, vol. 15, no. 1, p. 013024, 2013.

[62] C. A. Burrus and B. Miller, "Small-area, double-heterostructure aluminum-gallium arsenide electroluminescent diode sources for optical-fiber transmission lines," *Optics Communications*, vol. 4, no. 4, pp. 307–309, 1971.

[63] D. C. O'Brien, G. E. Faulkner, E. B. Zyambo, K. Jim, D. J. Edwards, P. Stavrinou, G. Parry, J. Bellon, M. J. Sibley, V. A. Lalithambika *et al.*, "Integrated transceivers for optical wireless communications," *IEEE Journal of Selected Topics in Quantum Electronics*, vol. 11, no. 1, pp. 173–183, 2005.

[64] M. M. Dumitrescu, M. J. Saarinen, M. D. Guina, and M. V. Pessa, "High-speed resonant cavity light-emitting diodes at 650 nm," *IEEE Journal of selected topics in quantum electronics*, vol. 8, no. 2, pp. 219–230, 2002.

[65] M. Akhter, P. Maaskant, B. Roycroft, B. Corbett, P. De Mierry, B. Beaumont, and K. Panzer, "200 Mbit/s data transmission through 100 m of plastic optical fibre with nitride LEDs," *Electronics Letters*, vol. 38, no. 23, pp. 1457–1458, 2002.

[66] A. Shaw, A. Bradley, J. Donegan, and J. Lunney, "GaN resonant cavity light-emitting diodes for plastic optical fiber applications," *IEEE Photonics Technology Letters*, vol. 16, no. 9, pp. 2006–2008, 2004.

[67] T. Komine and M. Nakagawa, "Fundamental analysis for visible-light communication system using LED lights," *IEEE Transactions on Consumer Electronics*, vol. 50, no. 1, pp. 100–107, Feb 2004.

[68] https://www.siemens.com/press/en/presspicture/?press=/en/presspicture/innovationnews/2010/in20100103-01.htm&content[]=CT&content[]=IO, accessed: 2018-03-05.

[69] S. Jin, J. Shakya, J. Lin, and H. Jiang, "Size dependence of III-nitride microdisk light-emitting diode characteristics," *Applied Physics Letters*, vol. 78, no. 22, pp. 3532–3534, 2001.

[70] J. J. McKendry, D. Massoubre, S. Zhang, B. R. Rae, R. P. Green, E. Gu, R. K. Henderson, A. Kelly, and M. D. Dawson, "Visible-light communications using a CMOS-controlled micro-light-emitting-diode array," *Journal of lightwave technology*, vol. 30, no. 1, pp. 61–67, 2012.

[71] D. Tsonev, H. Chun, S. Rajbhandari, J. J. McKendry, S. Videv, E. Gu, M. Haji, S. Watson, A. E. Kelly, G. Faulkner *et al.*, "A 3-Gb/s single-LED OFDM-based wireless VLC link using a gallium nitride μLED," *IEEE Photon. Technol. Lett.*, vol. 26, no. 7, pp. 637–640, 2014.

[72] H. E. Levin, "A complete and optimal data allocation method for practical discrete multitone systems," in *Global Telecommunications Conference, 2001. GLOBECOM'01. IEEE*, vol. 1. IEEE, 2001, pp. 369–374.

[73] C. Lee, C. Shen, H. M. Oubei, M. Cantore, B. Janjua, T. K. Ng, R. M. Farrell, M. M. El-Desouki, J. S. Speck, S. Nakamura *et al.*, "2 Gbit/s data transmission from an unfiltered laser-based phosphor-converted white lighting communication system," *Optics express*, vol. 23, no. 23, pp. 29 779–29 787, 2015.

[74] Y. Wang, X. Huang, L. Tao, J. Shi, and N. Chi, "4.5-Gb/s RGB-LED based WDM visible light communication system employing CAP modulation and RLS based adaptive equalization," *Optics express*, vol. 23, no. 10, pp. 13 626–13 633, 2015.

[75] F.-M. Wu, C.-T. Lin, C.-C. Wei, C.-W. Chen, Z.-Y. Chen, and K. Huang, "3.22-Gb/s WDM visible light communication of a single RGB LED employing carrier-less amplitude and phase modulation," in *Optical Fiber Communication Conference*. Optical Society of America, 2013, pp. OTh1G–4.

[76] G. Cossu, A. Khalid, P. Choudhury, R. Corsini, and E. Ciaramella, "3.4 Gbit/s visible optical wireless transmission based on RGB LED," *Optics express*, vol. 20, no. 26, pp. B501–B506, 2012.

[77] Y. Wang, X. Huang, J. Zhang, Y. Wang, and N. Chi, "Enhanced performance of visible light communication employing 512-QAM N-SC-FDE and DD-LMS," *Optics express*, vol. 22, no. 13, pp. 15 328–15 334, 2014.

[78] J. J. McKendry, D. Tsonev, R. Ferreira, S. Videv, A. D. Griffiths, S. Watson, E. Gu, A. E. Kelly, H. Haas, and M. D. Dawson, "Gb/s single-LED OFDM-based VLC using violet and UV gallium nitride μLEDs," in *Summer Topicals Meeting Series (SUM), 2015*. IEEE, 2015, pp. 175–176.

[79] C.-W. Jeon, H. W. Choi, E. Gu, and M. D. Dawson, "High-density matrix-addressable AlInGaN-based 368-nm microarray light-emitting diodes," *IEEE Photonics Technology Letters*, vol. 16, no. 11, pp. 2421–2423, Nov 2004.

[80] M. R. Krames, O. B. Shchekin, R. Mueller-Mach, G. O. Mueller, L. Zhou, G. Harbers, and M. G. Craford, "Status and Future of High-Power Light-Emitting Diodes for Solid-State Lighting," *Journal of Display Technology*, vol. 3, no. 2, pp. 160–175, June 2007.

[81] C. E. Shannon, "A mathematical theory of communication," *ACM SIGMOBILE Mobile Computing and Communications Review*, vol. 5, no. 1, pp. 3–55, 2001.

[82] Q. Dai, Q. Shan, H. Lam, L. Hao, Y. Lin, and Z. Cui, "Circadian-effect engineering of solid-state lighting spectra for beneficial and tunable lighting," *Optics express*, vol. 24, no. 18, pp. 20 049–20 059, 2016.

[83] A. Žukauskas, R. Vaicekauskas, and M. Shur, "Colour-rendition properties of solid-state lamps," *Journal of physics D: applied physics*, vol. 43, no. 35, p. 354006, 2010.

[84] J. M. Phillips, M. E. Coltrin, M. H. Crawford, A. J. Fischer, M. R. Krames, R. Mueller-Mach, G. O. Mueller, Y. Ohno, L. E. Rohwer, J. A. Simmons *et al.*, "Research challenges to ultra-efficient inorganic solid-state lighting," *Laser & Photonics Reviews*, vol. 1, no. 4, pp. 307–333, 2007.

[85] C. J. Humphreys, "Solid-state lighting," *MRS bulletin*, vol. 33, no. 4, pp. 459–470, 2008.

[86] R. P. Green, M. Jonathan, M. David, G. Erdan, D. Martin, and A. E. Kelly, "Modulation bandwidth studies of recombination processes in blue and green InGaN quantum well micro-light-emitting diodes," *Applied Physics Letters*, vol. 102, no. 9, p. 091103, 2013.

[87] S. Rajbhandari, J. J. McKendry, J. Herrnsdorf, H. Chun, G. Faulkner, H. Haas, I. M. Watson, D. O'Brien, and M. D. Dawson, "A review of gallium nitride LEDs for multi-gigabit-per-second visible light data communications," *Semiconductor Science and Technology*, vol. 32, no. 2, p. 023001, 2017.

[88] J. K. Kim and E. F. Schubert, "Transcending the replacement paradigm of solid-state lighting," *Opt. Express*, vol. 16, no. 26, pp. 21 835–21 842, Dec 2008.

[89] G. P. Agrawal, *Fiber-optic communication systems*. John Wiley & Sons, 2012.

[90] S. C. J. Lee, F. Breyer, S. Randel, R. Gaudino, G. Bosco, A. Bluschke, M. Matthews, P. Rietzsch, R. Steglich, H. P. A. van den Boom, and A. M. J. Koonen, "Discrete Multitone Modulation for Maximizing Transmission Rate in Step-Index Plastic Optical Fibers," *Journal of Lightwave Technology*, vol. 27, no. 11, pp. 1503–1513, June 2009.

[91] S. Watson, S. P. Najda, P. Perlin, M. Leszczynski, G. Targowski, S. Grzanka, M. A. Watson, H. White, and A. E. Kelly, "Multi-gigabit data transmission using a directly modulated GaN laser diode for visible light communication through plastic optical fiber and water," in *2015 IEEE Summer Topicals Meeting Series (SUM)*, July 2015, pp. 224–225.

[92] https://www.sonardyne.com/product/bluecomm-underwater-optical-communication-system/, accessed: 2018-03-25.

[93] K. Nakamura, I. Mizukoshi, and M. Hanawa, "Optical wireless transmission of 405 nm, 1.45 gbit/s optical im/dd-ofdm signals through a 4.8 m underwater channel," *Optics express*, vol. 23, no. 2, pp. 1558–1566, 2015.

[94] C. Pontbriand, N. Farr, J. Ware, J. Preisig, and H. Popenoe, "Diffuse high-bandwidth optical communications," in *OCEANS 2008*. IEEE, 2008, pp. 1–4.

[95] https://en.wikipedia.org/wiki/Electromagnetic_absorption_by_water#/media/File:Absorption_spectrum_of_liquid_water.png, accessed: 2017-10-04.

[96] S. Arai, S. Mase, T. Yamazato, T. Endo, T. Fujii, M. Tanimoto, K. Kidono, Y. Kimura, and Y. Ninomiya, "Experimental on hierarchical transmission scheme for visible light communication using LED traffic light and high-speed camera," in *Vehicular Technology Conference, 2007. VTC-2007 Fall. 2007 IEEE 66th*. IEEE, 2007, pp. 2174–2178.

[97] P. Luo, Z. Ghassemlooy, H. L. Minh, E. Bentley, A. Burton, and X. Tang, "Fundamental analysis of a car to car visible light communication system," in *2014 9th International Symposium on Communication Systems, Networks Digital Sign (CSNDSP)*, July 2014, pp. 1011–1016.

[98] https://spectrum.ieee.org/transportation/advanced-cars/bmw-laser-headlights-slice-through-the-da accessed: 2018-04-13.

[99] S. Watson, M. Tan, S. P. Najda, P. Perlin, M. Leszczynski, G. Targowski, S. Grzanka, and A. Kelly, "Visible light communications using a directly modulated 422 nm gan laser diode," *Optics letters*, vol. 38, no. 19, pp. 3792–3794, 2013.

[100] C. Lee, C. Zhang, M. Cantore, R. M. Farrell, S. H. Oh, T. Margalith, J. S. Speck, S. Nakamura, J. E. Bowers, and S. P. DenBaars, "4 gbps direct modulation of 450 nm gan laser for high-speed visible light communication," *Optics express*, vol. 23, no. 12, pp. 16 232–16 237, 2015.

[101] Y.-C. Chi, D.-H. Hsieh, C.-T. Tsai, H.-Y. Chen, H.-C. Kuo, and G.-R. Lin, "450-nm GaN laser diode enables high-speed visible light communication with 9-Gbps QAM-OFDM," *Optics express*, vol. 23, no. 10, pp. 13 051–13 059, 2015.

[102] M. H. Crawford, "LEDs for solid-state lighting: performance challenges and recent advances," *IEEE Journal of Selected Topics in Quantum Electronics*, vol. 15, no. 4, pp. 1028–1040, 2009.

[103] S. Chichibu, T. Sota, K. Wada, and S. Nakamura, "Exciton localization in InGaN quantum well devices," *Journal of Vacuum Science & Technology B: Microelectronics and Nanometer Structures Processing, Measurement, and Phenomena*, vol. 16, no. 4, pp. 2204–2214, 1998.

[104] M.-H. Kim, M. F. Schubert, Q. Dai, J. K. Kim, E. F. Schubert, J. Piprek, and Y. Park, "Origin of efficiency droop in GaN-based light-emitting diodes," *Applied Physics Letters*, vol. 91, no. 18, p. 183507, 2007.

[105] A. David and M. J. Grundmann, "Droop in ingan light-emitting diodes: A differential carrier lifetime analysis," *Applied Physics Letters*, vol. 96, no. 10, p. 103504, 2010.

[106] K. T. Delaney, P. Rinke, and C. G. Van de Walle, "Auger recombination rates in nitrides from first principles," *Applied Physics Letters*, vol. 94, no. 19, p. 191109, 2009.

[107] W. Scheibenzuber, U. Schwarz, L. Sulmoni, J. Dorsaz, J.-F. Carlin, and N. Grandjean, "Recombination coefficients of gan-based laser diodes," *Journal of Applied Physics*, vol. 109, no. 9, p. 093106, 2011.

[108] Y. Shen, G. Mueller, S. Watanabe, N. Gardner, A. Munkholm, and M. Krames, "Auger recombination in ingan measured by photoluminescence," *Applied Physics Letters*, vol. 91, no. 14, p. 141101, 2007.

[109] https://courses.cit.cornell.edu/ece533/Lectures/handout11.pdf, accessed: 2018-04-18.

[110] T. J. Slight, O. Odedina, W. Meredith, K. E. Docherty, and A. E. Kelly, "InGaN/GaN distributed feedback laser diodes with deeply etched sidewall gratings," *IEEE Photonics Technology Letters*, vol. 28, no. 24, pp. 2886–2888, 2016.

[111] M. S. Islim and H. Haas, "Modulation techniques for li-fi," *ZTE communications*, vol. 14, no. 2, pp. 29–40, 2016.

[112] D. Tsonev, S. Videv, and H. Haas, "Unlocking spectral efficiency in intensity modulation and direct detection systems," *IEEE Journal on Selected Areas in Communications*, vol. 33, no. 9, pp. 1758–1770, 2015.

[113] H. Kogelnik and C. V. Shank, "Coupled-Wave Theory of Distributed Feedback Lasers," vol. 43, pp. 2327 – 2335, 06 1972.

[114] http://eng.thesaurus.rusnano.com/wiki/article23844, accessed: 2017-10-04.

[115] L. Redaelli, "Design and fabrication of gan-based laser diodes for single-mode and narrow-linewidth applications," Ph.D. dissertation, Technische Universität Berlin, 2013.

[116] F. Renner, P. Kiesel, G. Dohler, M. Kneissl, C. G. Van de Walle, and N. M. Johnson, "Quantitative analysis of the polarization fields and absorption changes in InGaN/GaN quantum wells with electroabsorption spectroscopy," vol. 81, pp. 490–492, 07 2002.

[117] F. Tamburini, E. Mari, A. Sponselli, B. Thidé, A. Bianchini, and F. Romanato, "Encoding many channels on the same frequency through radio vorticity: first experimental test," *New Journal of Physics*, vol. 14, no. 3, p. 033001, 2012.

[118] J. Wang, J.-Y. Yang, I. M. Fazal, N. Ahmed, Y. Yan, H. Huang, Y. Ren, Y. Yue, S. Dolinar, M. Tur *et al.*, "Terabit free-space data transmission employing orbital angular momentum multiplexing," *Nature photonics*, vol. 6, no. 7, pp. 488–496, 2012.

[119] "100 Tbit/s free-space data link enabled by three-dimensional multiplexing of orbital angular momentum, polarization, and wavelength, author=Huang, Hao and Xie, Guodong and Yan, Yan and Ahmed, Nisar and Ren, Yongxiong and Yue, Yang and Rogawski, Dvora and Willner, Moshe J and Erkmen, Baris I and Birnbaum, Kevin M and others," *Optics letters*, vol. 39, no. 2, pp. 197–200, 2014.

[120] G. Gibson, J. Courtial, M. J. Padgett, M. Vasnetsov, V. Pas'ko, S. M. Barnett, and S. Franke-Arnold, "Free-space information transfer using light beams carrying orbital angular momentum," *Optics express*, vol. 12, no. 22, pp. 5448–5456, 2004.

[121] Y. Ren, L. Li, Z. Zhao, G. Xie, Z. Wang, N. Ahmed, Y. Yan, A. Willner, Y. Cao, C. Liu *et al.*, "4 Gbit/s underwater transmission using OAM multiplexing and directly modulated green laser," in *CLEO: Science and Innovations*. Optical Society of America, 2016, pp. SW1F–4.

[122] B. Rodenburg, M. P. Lavery, M. Malik, M. N. O'Sullivan, M. Mirhosseini, D. J. Robertson, M. Padgett, and R. W. Boyd, "Influence of atmospheric turbulence on states of light carrying orbital angular momentum," *Optics letters*, vol. 37, no. 17, pp. 3735–3737, 2012.

[123] J. M. Beckers, "Adaptive optics for astronomy: principles, performance, and applications," *Annual review of astronomy and astrophysics*, vol. 31, no. 1, pp. 13–62, 1993.

[124] V. I. Tatarski, *Wave propagation in a turbulent medium*. Courier Dover Publications, 2016.

[125] D. L. Fried, "Statistics of a geometric representation of wavefront distortion," *JOSA*, vol. 55, no. 11, pp. 1427–1435, 1965.

[126] Y. Ren, L. Li, Z. Wang, S. M. Kamali, E. Arbabi, A. Arbabi, Z. Zhao, G. Xie, Y. Cao, N. Ahmed *et al.*, "Orbital angular momentum-based space division multiplexing for high-capacity underwater optical communications," *Scientific reports*, vol. 6, 2016.

[127] G. C. Berkhout, M. P. Lavery, J. Courtial, M. W. Beijersbergen, and M. J. Padgett, "Efficient sorting of orbital angular momentum states of light," *Physical review letters*, vol. 105, no. 15, p. 153601, 2010.

[128] W. Hossack, A. Darling, and A. Dahdouh, "Coordinate transformations with multiple computer-generated optical elements," *Journal of Modern Optics*, vol. 34, no. 9, pp. 1235–1250, 1987.

[129] Y. Saito, S.-i. Komatsu, and H. Ohzu, "Scale and rotation invariant real time optical correlator using computer generated hologram," *Optics Communications*, vol. 47, no. 1, pp. 8–11, 1983.

[130] M. P. Lavery, D. J. Robertson, G. C. Berkhout, G. D. Love, M. J. Padgett, and J. Courtial, "Refractive elements for the measurement of the orbital angular momentum of a single photon," *Optics express*, vol. 20, no. 3, pp. 2110–2115, 2012.

[131] M. P. Lavery, G. C. Berkhout, J. Courtial, and M. J. Padgett, "Measurement of the light orbital angular momentum spectrum using an optical geometric transformation," *Journal of Optics*, vol. 13, no. 6, p. 064006, 2011.

[132] M. S. Islim, S. Videv, M. Safari, E. Xie, J. J. McKendry, E. Gu, M. D. Dawson, and H. Haas, "The impact of solar irradiance on visible light communications," *Journal of Lightwave Technology*, vol. 36, no. 12, pp. 2376–2386, 2018.